Imagerie ultrasonore multivues par cohérence de phase pour la détection et la caractérisation de défauts dans les soudures

par

Baptiste GAUTHIER

THÈSE PAR ARTICLES PRÉSENTÉE À L'ÉCOLE DE TECHNOLOGIE SUPÉRIEURE COMME EXIGENCE PARTIELLE À L'OBTENTION DU DOCTORAT EN GÉNIE
Ph.D.

MONTRÉAL, LE 21 NOVEMBRE 2022

ÉCOLE DE TECHNOLOGIE SUPÉRIEURE
UNIVERSITÉ DU QUÉBEC

PRÉSENTATION DU JURY

CETTE THÈSE A ÉTÉ ÉVALUÉE

PAR UN JURY COMPOSÉ DE:

M. Pierre Bélanger, directeur de thèse
Département de génie mécanique à l’École de technologie supérieure

Mme. Catherine Laporte, présidente du jury
Département de génie électrique à l’École de technologie supérieure

M. Ricardo Zednik, membre du jury
Département de génie mécanique à l’École de technologie supérieure

M. Philippe Micheau, examinateur externe
Faculté de génie mécanique à l’Université de Sherbrooke

ELLE A FAIT L’OBJET D’UNE SOUTENANCE DEVANT JURY ET PUBLIC

LE 17 NOVEMBRE 2022

À L’ÉCOLE DE TECHNOLOGIE SUPÉRIEURE

REMERCIEMENTS

Je souhaite tout d'abord remercier les membres du jury d'avoir accepté d'évaluer ce travail. Merci pour votre temps, votre intérêt et vos remarques.

Je souhaiterais ensuite remercier notre partenaire industriel, Olympus (ou Evident), qui a rendu possible ce projet, et plus encore nos deux scientifiques et fidèles collaborateurs, Alain et Guillaume.

Je tiens à remercier tout particulièrement mon directeur de thèse, Pierre Bélanger, pour son accompagnement et son soutien. La confiance que tu me démontres a beaucoup de valeur pour moi, tant pour mes travaux de doctorat que pour tous les petits (et gros) projets annexes que nous avons pu mener et continuons de mener ensemble.

Merci à tous les membres et anciens membres du PULETS avec qui j'ai pu forger de nombreux et excellents souvenirs au cours des six dernières années, tant en maîtrise qu'en doctorat. Les plus anciens : Nicolas (12), Aurélien, Victor, Guillaume, Fred, Thibault, Aubin, Geoffrey, Arthur, Damien, Tim, Cherif, Anthony, André, Mathieu L, et Jorge. Mais aussi ceux que j'ai connus plus récemment : Nathan, Lucas, Ricardo (BBQ), Bhupesh, Tony, Adrien, Hugo, Hugo, Laura et Douglas. Obrigado pelos bons momentos ! Enfin je me dois de remercier spécialement Daniel et Sévan pour les aventures entrepreneuriales que nous avons vécues ensemble, tout ça, en plein COVID ! Chapeau à nous trois ! Monsieur Bouchy, tu as su très agréablement me surprendre et démontrer une implication sans failles. J'espère continuer ces aventures avec toi pour encore un bon bout !

Un gros merci à mes amis pour votre présence et votre aide durant (toutes) ces années d'études. Ça n'aurait tout simplement pas fonctionné sans vous !

Un TRÈS gros merci à ma famille, qui croyait me voir parti au Québec pour seulement deux ans et qui après six ans, vient toujours me rendre visite régulièrement et n'a jamais douté de moi <3.

Mathieu, tu auras été la cerise sur le sundae de ces quatre dernières années, merci ! :-)

Imagerie ultrasonore multivues par cohérence de phase pour la détection et la caractérisation de défauts dans les soudures

Baptiste GAUTHIER

RÉSUMÉ

Les méthodes de contrôle non destructif (CND, traduction de nondestructive testing - NDT) par ultrasons sont largement utilisées dans l'industrie pour la détection et la caractérisation de défauts sur tous types de structures et à des cadences parfois élevées. C'est par exemple le cas pour l'inspection des soudures circonférentielles réalisées lors de la fabrication de pipelines. Lorsqu'il s'agit de réaliser une image de la pièce inspectée à l'aide de sondes multiéléments, l'image produite n'est en réalité qu'une représentation indirecte de la de la géométrie et des propriétés matériaux qu'il convient de bien interpréter afin d'en déduire la présence d'éventuels défauts. Les dernières avancées en termes d'électronique permettent aujourd'hui d'utiliser la méthode de focalisation en tout point (FTP, traduction de total focusing method - TFM) en temps réel afin de réaliser une image présentant une résolution accrue des différentes régions d'intérêt de la pièce. Cependant, cette méthode, bien que plus précise, présente certains inconvénients comme le fait d'être moins sensible que les méthodes conventionnelles à certains petits réflecteurs et de générer une quantité importante de données. De plus, l'utilisation grandissante de l'imagerie multivues, dérivée de la méthode TFM et qui ne considère par uniquement le chemin direct pour la reconstruction de l'image, est un fardeau supplémentaire pour l'inspecteur qui doit maintenant traiter un nombre très important de paramètres. Cependant, des méthodes d'imagerie reposant sur l'exploitation du contenu de la phase du signal ont été proposées ces dernières années et pourraient s'avérer utiles pour compenser les inconvénients associés à la méthode TFM. À travers ce travail, les propriétés du facteur de cohérence vectorielle (VCF), reposant sur l'analyse des composantes en phase et en quadrature du signal mesuré, sont exploitées dans le but de générer des images de la région d'intérêt. L'imagerie VCF repose sur la même catégorie d'algorithmes de formation de faisceaux de type délai et somme que la méthode TFM. Cependant, elle présente l'avantage de ne pas dépendre de l'amplitude du signal, d'être particulièrement sensible aux défauts diffractifs comme l'extrémité des soudures, et permet une combinaison facile des images issues des méthodes multivues. Dans cette étude, l'imagerie VCF est d'abord évaluée sur ses capacités à dimensionner des défauts, et comparée à la méthode de diffraction par temps de vol (TOFD) mais aussi à l'imagerie TFM. Ensuite, et puisque l'imagerie VCF repose sur l'exploitation de la phase du signal uniquement, la réduction de la quantité de données à acquérir pour générer une image de qualité est étudiée. Enfin, la fusion des différentes images issues de l'imagerie VCF multivues est étudiée et un seuil statistique est défini permettant de filtrer le bruit de fond. Des essais expérimentaux ont été menés sur deux configurations. La première est composée de deux plaques d'acier de ¾" d'épaisseur avec des encoches (centrées ou débouchantes) réalisées par électroérosion à plusieurs angles. La seconde est une plaque d'acier de 20 mm d'épaisseur avec des trous à fond plat (FBH : Flat Bottom Holes) usinés sur son bord imitant les réflecteurs utilisés pour l'étalonnage d'un appareil d'inspection de soudures circonférentielles. Une sonde multiéléments linéraire de 60 éléments, ayant une fréquence centrale de 7.5 MHz et montée sur un sabot en Rexolite de 36° a principalement été utilisée pour les différentes acquisitions. Finalement, il est montré que : 1- l'imagerie VCF présente des performances de dimensionnement similaires à la TOFD et meilleures que la TFM pour des encoches ayant un angle de 70° ou plus par rapport au plan horizontal ; 2- il est possible de réduire de près de cinquante fois la quantité de données nécessaires à la formation des images VCF en exploitant uniquement les fronts montants ou descendants du signal ; 3- l'imagerie VCF se prête très bien à la fusion simple des images issues des différentes vues, tout en conservant un rapport contraste à bruit de plus de 30 dB, et permettant de définir un seuil statistique qui permet de filtrer une grande partie du bruit de fond de l'image fusionnée.

Mots-clés: ultrasons, imagerie ultrasonore, focalisation en tout point, facteur de cohérence, cohérence vectorielle

Multi-view ultrasonic imaging using phase coherence imaging for detection and characterization of welds defects

Baptiste GAUTHIER

ABSTRACT

Ultrasonic nondestructive testing (NDT) methods are widely used in the industry for the detection and characterization of defects on all types of structures and, sometimes, at high speeds. This is for example the case for the inspection of girth welds during the manufacturing of pipelines. When using multi-element probes to produce an image of the inspected part, the resulting image is actually an indirect representation of the geometry and material properties that must be interpreted correctly in order to conclude on the presence of a defect. The latest advances in terms of electronics enable the use of the total focusing method (TFM) in real time to produce a high resolved image of the different regions of interest inside the inspected part. However, this method, although more accurate, has some drawbacks such as being less sensitive to small reflectors and generating a large amount of data during acquisition. Moreover, the increasing use of multi-view imaging, derived from the TFM and which does not rely only the direct path for image reconstruction, is an additional burden for the inspector who must now deal with a very large number of parameters. However, imaging methods based on the signal phase have also been proposed in recent years and could be useful to compensate the disadvantages associated with the TFM. In this work, the properties of the Vector Coherence Factor (VCF), based on the analysis of the in-phase and quadrature components of the measured signal, are leveraged in order to generate images of the region of interest. VCF imaging is based on the same type of delay-and-sum (DAS) beamformers as the TFM. However, it has the advantages of not relying on the signal amplitude, being particularly sensitive to diffractive defects such as crack tips, and allowing easy merging of images from multi-view methods. In this study, VCF imaging is first evaluated for defects sizing and compared to TFM and the time-of-flight diffraction method (TOFD). Then, as VCF imaging relies only on the use of the signal phase, the reduction of the data throughput during acquisition to generate a satisfying image is studied. Finally, the merging of different images from the multi-view implementation of VCF imaging is studied and a statistical threshold is defined to filter the background noise. Experiments were conducted on two sets of samples. The first one was composed of two ¾” thick steel plates with EDM notches at several angles centered at the mid-wall or surface-breaking on the backwall . The second one was a 20 mm thick steel plate with Flat Bottom Holes (FBH) machined on its edge mimicking reflectors used for calibration of a circumferential weld inspection apparatus. A 60-element linear multi-element probe with a center frequency of 7.5 MHz mounted on a 36° Rexolite wedge was used for the different acquisitions. Finally, it is shown that : 1- VCF imaging has similar sizing performances compared to TOFD and better performances than TFM for notches with an angle of 70° or more with respect to the horizontal plane ; 2- it is possible to reduce the amount of data required for VCF imaging by almost fifty times by exploiting only the rising or falling edges of the signal ; 3- VCF imaging is suitable for simple fusion of images from different views, while maintaining a contrast-to-noise ratio of more than 30 dB, and allowing the definition of a statistical threshold that filters out most of the background noise in the fused image.

X

Keywords: ultrasonics, ultrasonic imaging, total focusing method, coherence factor, vector coherence factor

TABLE DES MATIÈRES

Page

LISTE DES TABLEAUX

Page

LISTE DES FIGURES

LISTE DES ABRÉVIATIONS, SIGLES ET ACRONYMES

ASME	American Society of Mechanical Engineers
AUT	Automated Ultrasonic Testing
CCF	Circular Coherence Factor
CND	Contrôle Non Destructif
DAS	Delay and Sum
FBH	Flat Bottom Holes
FMC	Full Matrix Capture
FTP	Focalisation en Tout Point
HMC	Half Matrix Capture
IPCF	Instantaneous Phase Coherence Factor
IPCI	Instantaneous Phase Coherence Imaging
ISO	International Standards Organization
PCF	Phase Coherence Factor
PCI	Phase Coherence Imaging
SCF	Sign Coherence Factor
SCI	Sign Coherence Imaging
SNR	Signal to Noise Ratio
TFM	Total Focusing Method
TOF	Time of Flight
TOFD	Time of Flight Diffraction
ROI	Region of Interest
VCF	Vector Coherence Factor
VCI	Vector Coherence Imaging

LISTE DES SYMBOLES ET UNITÉS DE MESURE

δ_{ij}	Symbole delta de Kronecker
$\frac{\partial}{\partial}$	Dérivée partielle
λ	Premier coefficient de Lamé
λ_{wl}	Longueur d'onde
μ	Deuxième coefficient de Lamé
τ	Temps de vol
ν	Coefficient de poisson
Φ	Potentiel scalaire
ϕ	Phase du signal mesuré
Ψ	Potentiel vecteur
ω	Pulsation
ρ	Densité
σ	Écart type
A	Amplitude de l'onde
A_0	Amplitude initiale de l'onde
c_{ii}	Composante du tenseur d'élasticité
cos	Fonction cosinus
E	Module d'Young
f	Fréquence centrale du signal
Hz	Hertz
k	Nombre d'onde
R	Coefficient de réflexion
sin	Fonction sinus

T	Coefficient de transmission
tan	Fonction tangente
T_{ij}	Tenseur des contraintes
$Var(\cdot)$	Opérateur de variance
v_i	Vitesse de l'onde incidente
v_L	Vitesse longitudinale de l'onde
v_T	Vitesse de cisaillement ou transversale de l'onde
v_{tL}	Vitesse longitudinale de l'onde transmise
v_{tT}	Vitesse de cisaillement de l'onde transmise
y	Amplitude du signal mesuré
$\tilde{y}$	Forme analytique du signal mesuré

INTRODUCTION

Le contrôle de l'intégrité des structures, que ce soit lors de leur fabrication ou bien pendant leur fonctionnement, fait régulièrement appel à des technologies basées sur les ultrasons, ondes mécaniques dont la fréquence d'oscillation est située au-delà du spectre audible, i.e. au-dessus de 20 kHz. Ces technologies se réfèrent au domaine du contrôle non destructif (CND, traduction de nondestructive testing - NDT) ultrasonore dont les applications sont à la fois industrielles, pour la recherche de défauts et l'inspection de tous types de structures, mais aussi médicales afin d'effectuer des diagnostics avancés à travers les technologies bien connues d'échographie.

Dans cette étude, nous nous intéresserons à l'imagerie ultrasonore par sondes multiéléments pour ses applications industrielles. Contrairement aux signaux obtenus à l'aide de sondes à ultrasons conventionnelles composées d'un seul élément actif, les sondes multiéléments font appel à un réseau d'éléments pouvant être pilotés indépendamment afin d'orienter le champ ultrasonore incident dans une direction donnée ou bien de mesurer simultanément et en plusieurs points le champ réfléchi. Si l'innovation concernant la fabrication de ces sondes reste marginale au cours des dernières années, les unités de contrôle, le traitement numérique qui y est appliqué et les algorithmes d'imagerie qui y sont associés ont fait l'objet de recherches poussées. Ceci, principalement en raison de l'augmentation des performances de calcul, tant en puissance qu'en temps, des contrôleurs pouvant être utilisés en développement comme en production grâce à la miniaturisation des unités portatives.

Les techniques d'imagerie ultrasonore sont souvent comparées et mises au défi par les méthodes radiographiques qui permettent un rendu plus photoréaliste, poussant les fabricants d'appareils de contrôle à innover davantage. Ainsi, les méthodes par balayage linéaire et sectoriel ont longtemps représenté le standard en termes d'inspection multiélément. Dernièrement, la méthode de focalisation en tout point (FTP, traduction de total focusing method - TFM), plus gourmande en ressources, mais maintenant largement employée et rendue possible en temps réel, assure un plus grand confort aux techniciens d'inspection grâce à un rendu d'image plus réaliste et facilement interprétable. Cette dernière est d'autant plus intéressante qu'elle offre la possibilité de considérer différentes vues en fonction du trajet emprunté par les ondes ultrasonores et des conversions de modes ayant lieu lors des interactions avec des réflecteurs. Cependant, ces différentes vues sont pour le moment exploitées individuellement et l'opérateur doit interpréter la contribution de chacune d'entre elles à la détection éventuelle d'un défaut. Enfin, des méthodes dérivées de la TFM et faisant l'objet de recherches actives, exploitant uniquement la phase du signal mesuré, présentent de nombreux avantages et seront exploitées dans cette étude.

Evident Industrial (anciennement Olympus NDT Canada) est le partenaire industriel de ce travail. L'entreprise développe des équipements d'inspection et réalise également leur intégration dans des environnements industriels. Le cas d'application de cette étude concerne l'inspection des soudures circonférentielles nécessaires à l'assemblage de conduites et pour lesquelles une solution robotisée dédiée a été développée. Cette solution fait appel à plusieurs sondes multiéléments afin de réaliser une image précise des différentes zones de la soudure et en particulier du chanfrein de celle-ci où se concentre généralement les défauts (manque de fusion, inclusions, fissures, porosités etc.). Cependant, l'information actuellement présentée au technicien d'inspection, reposant sur les méthodes monoélément et multiéléments traditionnelles, demeure très complexe d'interprétation et requiert une expérience élevée qu'il n'est pas toujours facile d'obtenir. Il y a donc un intérêt fort pour une méthode permettant de rendre une image plus facile d'interprétation au technicien tout en simplifiant la procédure d'inspection. L'objectif de cette recherche est donc axé sur le développement de nouvelles techniques d'imagerie ultrasonore par sondes multiéléments, basées sur la méthode TFM, afin de simplifier la procédure d'inspection et améliorer l'interprétation de l'information. L'enjeu est également d'améliorer la confiance accordée aux technologies ultrasonores face à des technologies concurrentes ou complémentaires (comme la radiographie ou l'inspection par courants de Foucault) qui elles aussi ont leurs défis.

L'étude a ainsi été conduite en deux grandes parties :

- Comprendre, étudier et comparer les possibilités offertes par la méthode TFM et et en particulier ses dérivés reposant sur la phase du signal par rapport aux méthodes traditionnelles en ce qui a trait à la facilité d'interprétation de l'information et la qualité de la mesure. En effet, les méthodes d'imagerie reposant sur la phase du signal permettent par exemple de s'affranchir des étapes de calibration et présentent une grande sensibilité aux extrémités des défauts, facilitant ainsi leur dimensionnement.
- Exploiter les possibilités offertes par ces nouvelles méthodes afin de simplifier la procédure d'inspection et synthétiser l'information issue des différentes vues qui peuvent être générées. En particulier, on s'intéressera aux possibilités offertes en termes de réduction de la quantité de données nécessaire à la génération des images, un enjeu industriel important lorsqu'il s'agit de stocker les données de milliers d'inspections, ainsi qu'aux différentes méthodes de fusion des vues qui peuvent être générées.

Enfin, le document est décomposé en cinq chapitres. Le premier chapitre fera état de la littérature entourant le sujet. Les trois chapitres qui suivront présenteront les articles publiés et soumis au cours de cette étude. Enfin, le dernier chapitre traitera des conclusions qu'il convient de faire à la suite de ce travail.

CHAPITRE 1

REVUE DE LITTÉRATURE

Cette revue de littérature a pour objectif de présenter les notions fondamentales nécessaires à la compréhension du sujet abordé, mais également d'établir l'état de l'art en ce qui concerne la problématique étudiée. Ainsi elle présentera dans un premier temps les principes de base relatifs aux ondes ultrasonores de volume et à leur propagation et se concentrera ensuite sur les méthodes d'imagerie avancées qui sont utilisés dans le cadre de ce travail.

1.1 Propagation d'une onde ultrasonore, et ses différents modes

Une onde ultrasonore est avant tout une onde mécanique, soit une perturbation locale qui a besoin d'un milieu matériel pour sa propagation, et dont la fréquence est située au-dessus du spectre audible, soit au-delà de 20kHz. De nombreux livres de référence détaillent la théorie et l'histoire de ce domaine (Royer, Dieulesaint & Gennes, 1996; Cheeke, 2017). On se limitera dans cette étude, au cas de la propagation des ondes ultrasonores dans un matériau isotrope et homogène.

1.1.1 Propagation des ondes de volume dans les solides

La propagation des ondes a dans un premier temps été mise en équation par d'Alembert pour le cas unidimensionnel puis généralisée à n'importe quel cas tridimensionnel par Euler. L'étude du cas unidimensionnel fait apparaître des paramètres essentiels liés à la propagation des ondes comme la longueur d'onde, le nombre d'onde, la période et la pulsation. La généralisation au cas tridimensionnel apporte la théorie nécessaire à la compréhension de la propagation de plusieurs modes. C'est sur ces différentes notions fondamentales que reposent les méthodes d'imagerie présentées plus loin.

1.1.1.1 Formulation dans le cas unidimensionnel

La propagation d'une onde mécanique est décrite par l'équation de d'Alembert, aussi connue sous le nom d'équation d'onde :

$$\frac{\partial^2 u\,(x,t)}{\partial x^2} = \frac{1}{v^2}\,\frac{\partial^2 u\,(x,t)}{\partial t^2}, \tag{1.1}$$

où v représente la célérité de l'onde.

La solution générale est de la forme :

$$u\,(x,t) = f\,(x - vt) + g\,(x + vt)\,, \tag{1.2}$$

où

$$U\,(x,t) = F\left(t - \frac{x}{v}\right) + G\left(t + \frac{x}{v}\right), \tag{1.3}$$

avec f, g, F et G des fonctions arbitraires dont le premier terme est relatif à la propagation de l'onde dans la direction positive de l'axe x alors que le second terme est relatif à la propagation de l'onde dans la direction négative, toujours selon l'axe x.

En considérant une perturbation de forme sinusoïdale, la solution peut alors s'exprimer :

$$u\,(x,t) = A\cos\left(\omega t - kx\right) \tag{1.4}$$

avec :

- $\omega = \frac{2\pi}{T}$ la pulsation de période T
- $k = \frac{\omega}{T} = \frac{2\pi}{\lambda_{wl}}$ le nombre d'onde et λ_{wl} la longueur d'onde.

Dans cette expression, $-k.x$ représente le déphasage spatial alors que $\omega.t$ représente le déphasage temporel. Il est possible d'écrire la phase de l'onde sous la forme $\phi(x,t) = \omega t - kx$ que nous retrouverons plus loin lorsque que nous présenterons des méthodes d'imagerie reposant sur cette dernière. Le nombre d'onde k représente ainsi la variation de la phase ϕ par rapport à la position

x à un temps donné t alors que la pulsation ω représente la variation de la phase ϕ par rapport au temps t à une position donnée x.

1.1.1.2 Formulation dans le cas tridimensionnel

L'équation de propagation dans le cas tridimensionnel peut être obtenue à partir des équations fondamentales de la mécanique,

$$\rho \frac{\partial^2 u_i}{\partial t^2} = \frac{\partial T_{ij}}{\partial x_j} \tag{1.5}$$

avec ρ la densité du matériau, T_{ij} le tenseur des contraintes pour un matériau isotrope, défini par une généralisation de la loi de Hooke :

$$T_{ij} = c_{ijkl} S_{kl} \tag{1.6}$$

avec c_{ijkl} le tenseur d'élasticité et S_{kl} le tenseur des déformations. T_{ij} peut aussi s'écrire comme

$$T_{ij} = \lambda S_{ii} \delta_{ij} + 2\mu\, S_{ij} \tag{1.7}$$

avec δ_{ij} le delta de Kronecker, λ et μ les coefficients de Lamé qui peuvent s'écrire en fonction du module d'Young, du coefficient de Poisson ou encore du tenseur d'élasticité du matériau :

$$\begin{cases} E = \frac{\mu(3\lambda+2\mu)}{(\lambda+\mu)} \\ \nu = \frac{\lambda}{2\,(\lambda+\mu)} \\ c_{44} = \frac{c_{11}-c_{12}}{2} = \mu \\ c_{12} = \lambda \end{cases}, \tag{1.8}$$

À l'aide des équations précédentes on a :

$$T_{ij} = c_{12} S_{ii} \delta_{ij} + 2 c_{44} S_{ij} = (c_{11} - 2c_{44}) \frac{\partial u_i}{\partial x_i} \delta_{ij} + c_{44} \left(\frac{\partial u_i}{\partial x_j} + \frac{\partial u_j}{\partial x_i} \right). \tag{1.9}$$

Enfin, on peut obtenir :

$$\rho \frac{\partial^2 u_i}{\partial t^2} = \frac{\partial}{\partial x_i}\left[(c_{11} - c_{44})\,\frac{\partial u_j}{\partial x_i}\right] + c_{44}\frac{\partial^2 u_i}{\partial x_j}. \tag{1.10}$$

Cette dernière équation peut être réécrite sous sa forme vectorielle :

$$\rho \frac{\partial^2 \vec{u}}{\partial t^2} = (c_{11} - c_{44})\,\vec{\nabla}(\vec{\nabla} \cdot \vec{u}) + c_{44}\,\Delta\vec{u}. \tag{1.11}$$

Les trois composantes du champ de déplacement $\vec{u}$ peuvent être découplées en utilisant la décomposition de Helmholtz et en définissant un potentiel scalaire Φ et un potentiel vecteur Ψ :

$$\vec{u} = \vec{\nabla}\Phi + \vec{\nabla} \times \Psi = \vec{u}_L + \vec{u}_T \tag{1.12}$$

où $\vec{u}_L$ a un rotationnel nul et $\vec{u}_T$ une divergence nulle. Ainsi, en utilisant les équations précédentes nous avons deux équations indépendantes :

$$v_L^2 \Delta\Phi - \frac{\partial^2 \Phi}{\partial t^2} = 0, \tag{1.13}$$

qui correspond à un mouvement longitudinal pur dépendant du potentiel scalaire Φ et

$$v_T^2 \Delta\Psi - \frac{\partial^2 \Psi}{\partial t^2} = 0, \tag{1.14}$$

qui correspond à un mouvement de cisaillement pur dépendant du potentiel vecteur Ψ. Chaque type de mouvement est aussi caractérisé par une vitesse de propagation spécifique : v_L pour la vitesse longitudinale et v_T pour la vitesse de cisaillement de l'onde. Ces vitesses peuvent directement être exprimées en fonction des propriétés matériaux :

$$v_L = \sqrt{\frac{c_{11}}{\rho}} = \sqrt{\frac{\lambda + 2\mu}{\rho}}, \tag{1.15}$$

$$v_T = \sqrt{\frac{c_{44}}{\rho}} = \sqrt{\frac{\mu}{\rho}}. \tag{1.16}$$

À la suite de cette démonstration nous remarquons qu'il y a propagation indépendante d'uniquement deux types d'ondes : les ondes longitudinales (ou ondes P ou de compression) et les ondes de cisaillement (ou ondes T ou transversales). Tout autre mode de propagation dans un matériau solide est dérivé de ces deux modes fondamentaux. La Figure 1.1 illustre la déformation induite dans un solide pour ces deux cas. Les ondes longitudinales se propagent grâce à un série de compressions et dilatations d'un volume donné de matière (Figure 1.1a.) et les ondes de cisaillement se propagent grâce au glissement, à volume constant, de plans atomiques parallèles et adjacents (Figure 1.1b.).

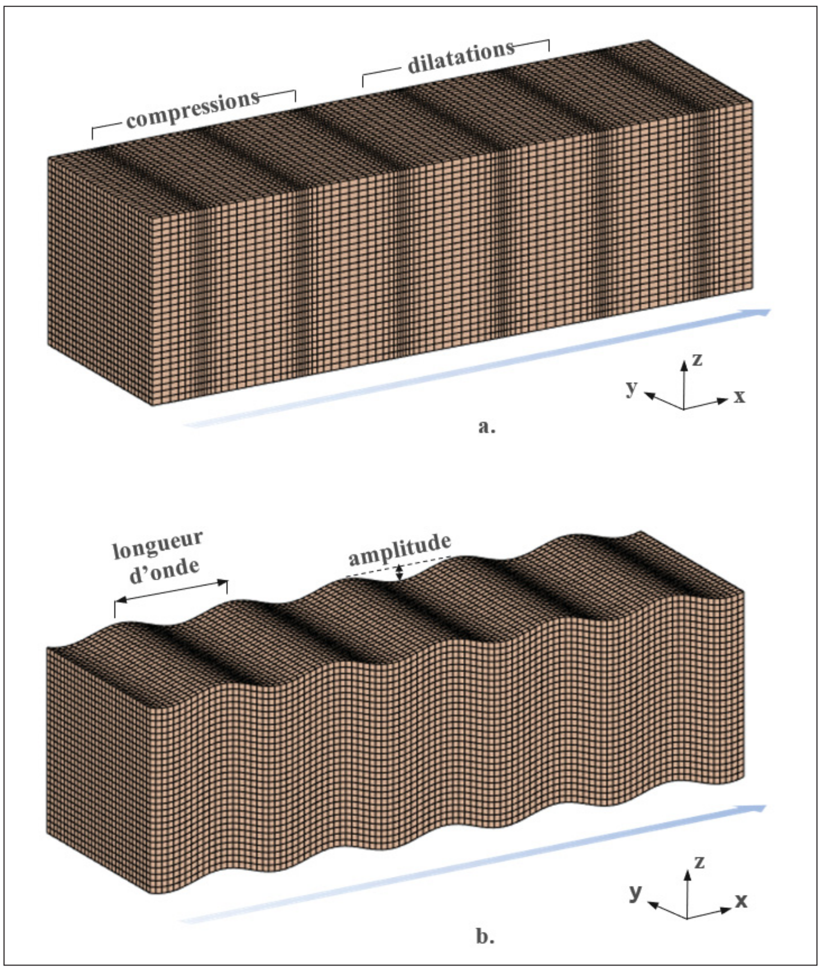

Figure 1.1 Déformation induite dans un solide par la propagation selon l'axe x de (a.) une onde longitudinale et (b.) une onde de cisaillement

1.1.2 Interactions aux interfaces

Quand une onde mécanique progressive rencontre une frontière entre deux matériaux isotropes aux propriétés mécaniques différentes, une fraction de l'énergie incidente est réfléchie dans le matériau initial et le reste de cette énergie est transmise dans le deuxième matériau. En fonction de l'angle d'incidence et des propriétés matériau, les ondes mécaniques résultant de l'interaction avec cette interface sont décrites par les lois de Snell-Descartes ou lois de la réfraction.

Ainsi, si l'on considère une onde incidente oblique se propageant dans un milieu solide comme illustré sur la Figure 1.2a., les lois de Snell-Descartes donnent :

$$\frac{\sin\theta_i}{v_i} = \frac{\sin\theta_{tL}}{v_{tL}} = \frac{\sin\theta_{tT}}{v_{tT}} \tag{1.17}$$

avec θ_i l'angle de l'onde incidente, θ_{tL} l'angle de l'onde longitudinale transmise et θ_{tT} l'angle de l'onde de cisaillement transmise (ces angles sont aussi appelés angles de réfraction) dont les vitesses de propagation respectives sont v_i, v_{tL} et v_{tT}. Les mêmes lois s'appliquent pour les ondes réfléchies. Quand le milieu incident est un liquide non visqueux comme illustré dans la Figure 1.2b., seule une onde longitudinale est réfléchie avec le même angle que l'onde incidente et les lois de Snell-Descartes s'appliquent de la même manière pour les ondes réfractées dans le second milieu.

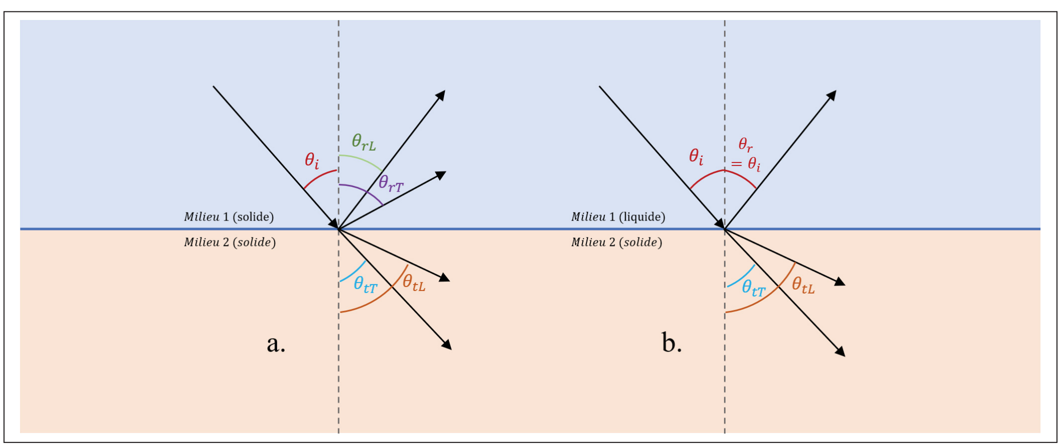

Figure 1.2 Interactions d'une onde mécanique incidente avec (a.) une interface solide/solide et (b.) une interface liquide (non visqueux)/solide

De plus, il est possible de calculer simplement la portion de l'énergie réfléchie et transmise à partir de l'impédance acoustique des deux matériaux. Ainsi on exprime le coefficient de réflexion, R, et le coefficient de transmission, T, comme :

$$R = \frac{Z_2 \cos\theta_i - Z_1 \cos\theta_t}{Z_2 \cos\theta_i + Z_1 \cos\theta_t}, \tag{1.18}$$

$$T = \frac{2Z_2 \cos\theta_i}{Z_2 \cos\theta_i + Z_1 \cos\theta_t}, \tag{1.19}$$

avec $Z_n = \rho_n\ v_n$ l'impédance acoustique du matériau pour le mode de propagation spécifié, et θ_t l'angle de l'onde transmise, qu'elle soit longitudinale ou de cisaillement. Ces interactions à la frontière entre deux milieux et la réfraction de deux modes de propagation (longitudinal et transversal) sont la base de l'imagerie ultrasonore multivues que nous détaillerons un peu plus loin.

1.1.3 Atténuation

L'atténuation est un phénomène associé à la perte d'énergie de l'onde avec l'augmentation de sa distance de propagation dans un milieu déterminé. Celle-ci peut être modélisée par :

$$A\ (x) = \ A_0.e^{-\alpha x} \tag{1.20}$$

avec A_0 l'amplitude initiale de l'onde, A l'amplitude de l'onde à une distance x et α le coefficient d'atténuation. Le coefficient d'atténuation est affecté par de nombreux phénomènes comme la diffraction, la diffusion et l'absorption qui mènent à une perte d'énergie lors de la propagation de l'onde, mais est aussi influencé par les propriétés matériau et le type d'excitation. Il est cependant important de noter que de manière générale, l'atténuation augmente avec la fréquence de la perturbation générée par le transducteur ultrasonore. On peut retrouver une analyse détaillée de l'influence de chacun des paramètres évoqués sur l'atténuation dans certains livres de référence (Royer *et al.*, 1996; Schmerr, 1998; Cheeke, 2017).

1.2 Du transducteur conventionnel au transducteur multiéléments

Pour la génération des ondes, et dans le cadre de ce projet, des transducteurs basés sur la technologie piézoélectrique seront utilisés. Ils sont les plus répandus pour la génération d'ondes ultrasonores et sont à l'origine des sondes multiéléments qui seront utilisées pour notre étude. Nous détaillerons dans cette partie et de façon succincte le fonctionnement des transducteurs conventionnels et des transducteurs multiéléments.

1.2.1 Transducteur conventionnel

Comme illustré sur la Figure 1.3, un transducteur (ou une sonde) ultrasonore conventionnel est constitué de trois éléments clés (Schmerr Jr, 2016) :

- Un matériau piézoélectrique recouvert d'électrodes
- Une couche de couplage entre l'élément piézoélectrique et la pièce inspectée servant à protéger l'élément et maximiser l'énergie transmise à la pièce. Cette couche a de façon générale une épaisseur d'un quart de la longueur d'onde correspondant à la fréquence centrale de la sonde.
- Une couche d'absorption permettant notamment l'atténuation de la partie de l'onde qui se propagerait dans le boîtier du transducteur.

Selon la nature et la polarisation de l'élément piézoélectrique, celui-ci peut générer soit des ondes de compression, soit des ondes de cisaillement.

Outre les différentes propriétés physiques d'un transducteur conventionnel, il convient d'évoquer quelques propriétés du champ ultrasonore qu'il génère dans la pièce (Figure 1.4a.). Celui-ci est affecté par la géométrie du transducteur et par les caractéristiques du signal qui est envoyé à ses bornes. Ainsi, ce champ ultrasonore est caractérisé par une zone située directement sous la surface du transducteur et où l'énergie varie de façon conséquente, cette zone est appelée le champ proche. Le champ lointain, situé après le champ proche, possède, lui, une variation d'énergie beaucoup plus faible. Dans cette dernière zone, l'énergie décroît progressivement avec l'augmentation de la distance par rapport à la surface du transducteur (Figure 1.4b.).

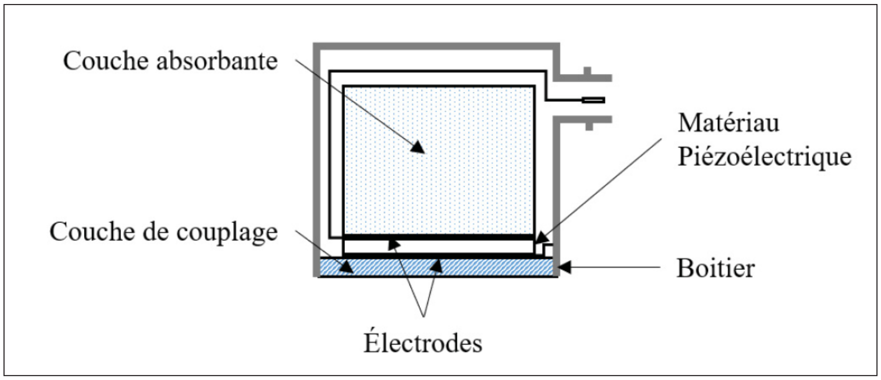

Figure 1.3 Principaux éléments constitutifs d'un transducteur ultrasonore conventionnel

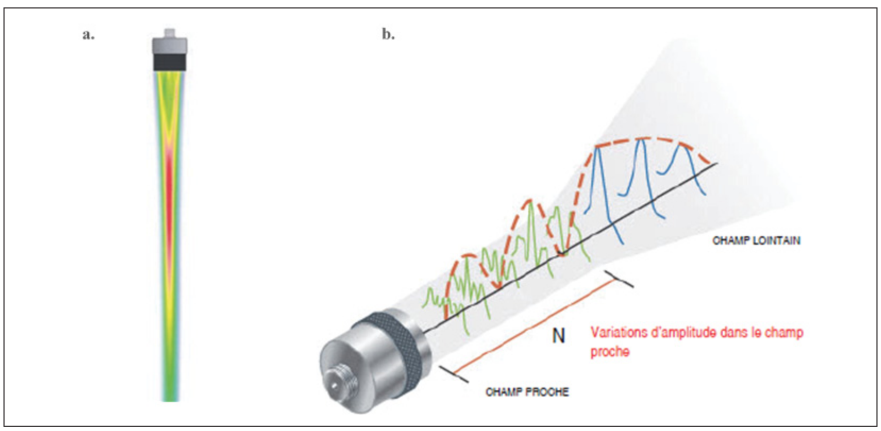

Figure 1.4 Illustration du champ ultrasonore sous la surface d'un transducteur avec (a.) la distribution de l'énergie sous la surface du transducteur et (b.) le champ proche et champ lointain sous la surface d'un transducteur
Tirée de Olympus (2015, p. 15)

Le champ proche est parfois également appelé distance de Fresnel et peut être calculé simplement pour un transducteur circulaire :

$$N = \frac{D^2}{4\lambda_{wl}} \tag{1.21}$$

avec D le diamètre de l'élément piézoélectrique et λ_{wl} la longueur d'onde relative au signal généré par le transducteur. Lorsque l'onde se propage au-delà du champ proche, le faisceau de celle-ci diverge. L'angle de divergence est influencé à la fois par la fréquence du signal d’excitation, le matériau dans lequel l’onde se propage et la géométrie du transducteur. Toujours dans le cas d’un transducteur circulaire, cet angle de divergence peut se calculer par :

$$\alpha = \sin^{-1}\left(\frac{0.514\ v}{f\ D}\right) \tag{1.22}$$

avec v la vitesse de l’onde dans le matériau considéré et f la fréquence centrale du signal d’excitation.

1.2.2 Transducteur multiéléments

Un transducteur multiéléments, d’une point de vue fonctionnel, est un assemblage d’une multitude d’éléments piézoélectriques pilotables indépendamment. Il est par ailleurs construit de la même manière qu’un transducteur conventionnel, ainsi composé d’une couche de couplage et d’une couche d’absorption. Plusieurs configurations de sondes multiéléments existent, suivant la disposition des éléments piézoélectriques. Ainsi, la plus commune est la sonde dite linéaire (Figure 1.5a.), mais on trouve également des sondes matricielles (Figure 1.5b.), annulaires (Figure 1.5c.), courbées, focalisées, etc. On retrouve également des sondes adaptées spécifiquement à la géométrie de la pièce pour certains cas spécifiques.

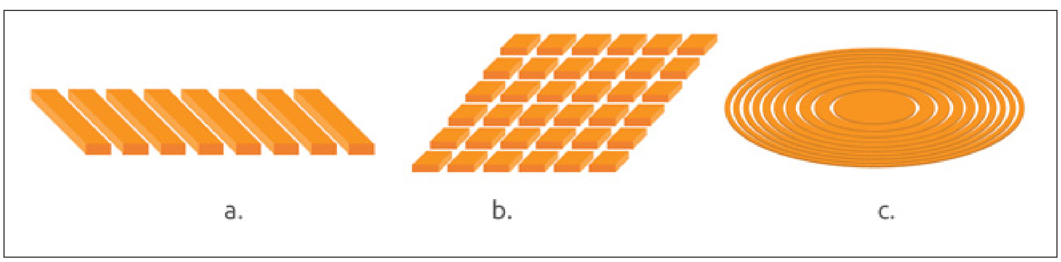

Figure 1.5 Agencement des éléments piézoélectriques pour (a.) une sonde linéaire, (b.) une sonde matricielle et (c.) une sonde annulaire

Un premier intérêt de ce type de sondes réside dans la possibilité de construire un front d’onde orienté et focalisé dans la direction souhaitée, à l’aide d’un pilotage indépendant de chaque élément. De simples délais sont ajoutés à chaque tire pour chaque élément afin de constituer le front d’onde désiré. Par analogie, l’interférence résultante entre chaque front d’onde individuel émis par chaque élément est comparable à ce que l'on peut observer lors de la propagation de plusieurs perturbations à la surface d'un bassin d'eau. Un deuxième intérêt des sondes multiéléments est le fait de pouvoir collecter, avec une même sonde, de multiples signaux de manière simultanée et sur une petite surface. Cette propriété sera notamment exploitée par l'acquisition FMC que nous présenterons plus loin.

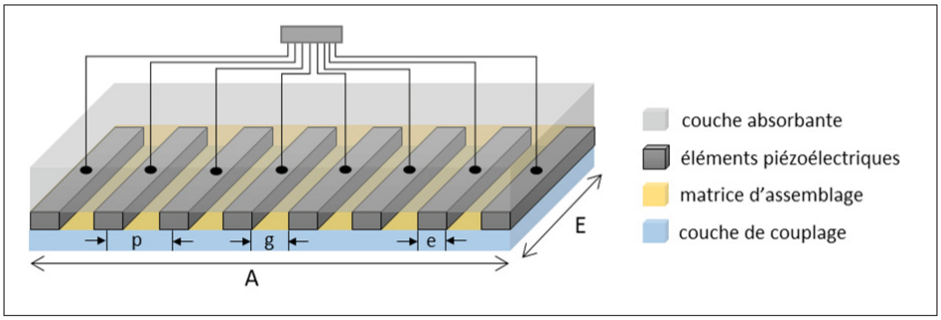

Figure 1.6 Schéma illustrant les différents composants d'une sonde multiéléments

Une sonde multiéléments, comme illustré sur la Figure 1.6, est caractérisée par différents paramètres comme l'ouverture A (longueur totale active de la sonde), le nombre d'éléments N_e, le pas élémentaire p (distance entre le centre de deux éléments contigus), son élévation E (largeur de la sonde), sa fréquence centrale etc. Enfin, comme les sondes conventionnelles à un seul élément, les sondes multiéléments sont souvent couplées à un sabot possédant un certain angle afin d'orienter le champ ultrasonore et de favoriser un mode de propagation en particulier (par conversion de mode à l'interface avec la pièce à inspecter). Dans notre étude, seul des sondes linéaires seront considérées. Nous ne détaillerons pas ici l'influence de chaque paramètre de la sonde sur les performances de l'imagerie ultrasonore par souci de concision. Notons également que nous nous intéresserons uniquement aux applications industrielles de ces sondes et pas à leur utilisation dans le domaine médical. De plus, de nombreux livres de référence traitent déjà de ce sujet (Schmerr Jr, 2015).

1.3 Méthodes d'imagerie avancées

Si la conception des transducteurs a très peu évolué au cours des dernières années, les méthodes d'imagerie en même temps que les contrôleurs permettant le pilotage des sondes ont profité des avancées importantes dans la miniaturisation et l'augmentation des capacités de calcul des microprocesseurs. Les méthodes d'imagerie ultrasonore conventionnelles, notamment par balayage sectoriel et linéaire, sont encore largement utilisées particulièrement en raison du temps nécessaire à l'élaboration de nouvelles procédures de certification et d'homologation. Nous présenterons dans cette partie la technique de focalisation en tout point (TFM) ainsi que le principe de l'imagerie multivues (ou multi-modes) qui en découle. Nous introduirons également une série de méthodes d'imagerie basées sur l'exploitation de la phase du signal, dérivées de la méthode TFM, et qui seront largement utilisées dans cette étude.

1.3.1 Focalisation en tout point (TFM)

Les images produites grâce aux méthodes conventionnelles d'imagerie ultrasonore par sondes multiéléments consistent en une simple représentation des signaux reçus sur chaque élément et disposés les uns à la suite des autres en appliquant ou non certains délais, généralement les mêmes qu'à l'émission (Figure 1.7a. et c.). La méthode TFM (dans la suite du document nous utiliserons l'acronyme anglais qui est plus répandu), elle, réalise une focalisation virtuelle en de multiples points d'une région d'intérêt dans la pièce définie au préalable (Holmes, Drinkwater & Wilcox, 2005; Zhang, Drinkwater & Wilcox, 2013a), permettant ainsi une reconstruction plus détaillée des éventuels défauts présents, comme illustré dans la Figure 1.7c..

Le schéma d'acquisition des données nécessaires à cette reconstruction diffère des méthodes conventionnelles, et procède comme illustré sur la Figure 1.8 et est actuellement connu sous le nom de capture matricielle complète (FMC : Full Matrix Capture) . Une première émission, sans délais, est tout d'abord effectuée sur le premier élément de la sonde puis tous les autres éléments de la sonde mesurent le signal généré par la réflexion des ondes dans la pièce. Cette opération est répétée pour tous les éléments consécutifs de la sonde. Considérant un nombre d'éléments N_e,

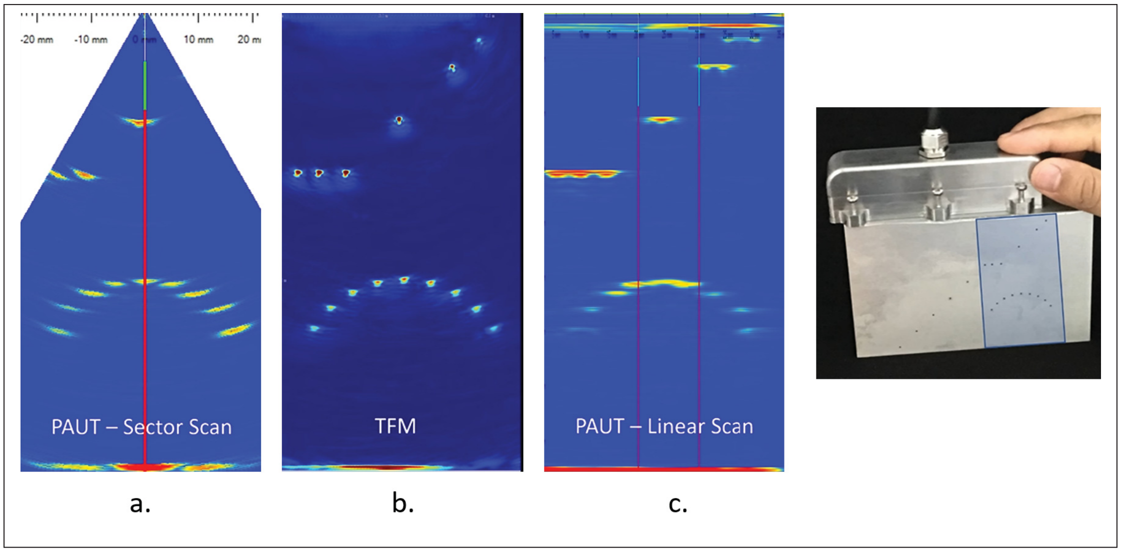

Figure 1.7 Comparaison entre l'image obtenue par (a.) un balayage sectoriel, (b.) la TFM et (c.) par un balayage linéaire sur une pièce en acier comportant différents trous percés sur le côté et en utilisant une sonde multiéléments linéaire
Adaptée de The Phased Array Company (2021)

on obtient N_e^2 traces temporelles qui seront ensuite traitées afin de générer une image de la région d'intérêt. Pour limiter la quantité de données acquises et considérant le principe de réciprocité relatif à la propagation des ondes mécaniques dans un milieu homogène, on préfère généralement garder la moitié de la matrice d'émission-réception ainsi générée (HMC : Half Matrix Capture). Remarquons également que le temps d'acquisition des données est plus important pour cette méthode que pour les méthodes conventionnelles, ce qui peut parfois représenter un inconvénient majeur lorsqu'une cadence d'inspection élevée est requise.

Après acquisition des signaux, l'image de la région d'intérêt est calculée par formation de faisceaux (beamforming) à l'aide d'un algorithme de type délai et somme (DAS : Delay-And-Sum) en prenant en considération le temps de vol total τ (TOF : Time Of Flight) entre l'élément émetteur, le pixel de la région d'intérêt (ROI : Region of Interest) dans la pièce, et l'élément utilisé en réception (Figure 1.9a.). On peut considérer soit un chemin direct entre le point d'émission, le point de reconstruction (ou focalisation) et le point de réception, ou bien un

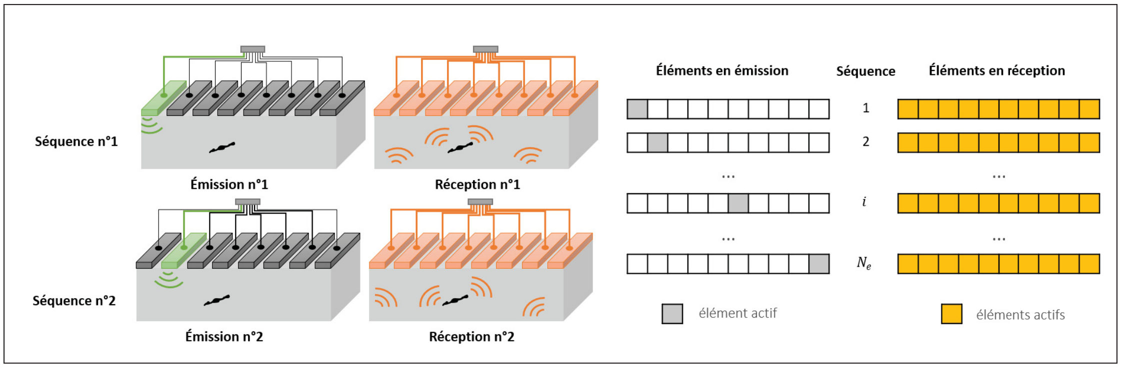

Figure 1.8 Principe de l'acquisition FMC

chemin indirect comportant des réflexions sur les faces de la pièce comme nous le verrons dans la section suivante (Figure 1.9b.).

Ainsi, considérons une région d'intérêt dans la pièce, discrétisée par une grille de pixels pour laquelle chaque pixel est localisé par sa position (x, z). L'intensité de chaque pixel de la région d'intérêt après l'application d'un algorithme de reconstruction de type DAS basé sur l'amplitude du signal, comme la TFM, est donnée par :

$$\begin{aligned} I_{\mathrm{TFM}}(x,z) &= \left| \sum_{k=1}^{N_e} \sum_{l=1}^{N_e} \tilde{y}_{kl}(\tau_{kl}(x,z)) \right| \\ &= \left| \sum_{k=1}^{N_e} \sum_{l=1}^{N_e} |\tilde{y}_{kl}(\tau_{kl}(x,z))| \mathrm{e}^{i\phi_{kl}(\tau_{kl}(x,z))} \right| \end{aligned} \tag{1.23}$$

où $\tilde{y}_{kl}(t)$ désigne le signal analytique de l'amplitude du signal reçu $y_{kl}(t)$ sur chaque élément à un instant donné $\tau_{kl}(x, z)$, correspondant au temps de vol total entre l'élément émetteur k, un pixel, et l'élément récepteur l (Figure 1.9a.). Plus la zone de reconstruction est grande et dense, plus le temps de calcul est important. Si les ressources électroniques nécessaires pour le calcul de l'image ont longtemps été une limite à l'utilisation cette méthode, elle est depuis quelques années progressivement introduite dans les équipements commerciaux portatifs. La norme ASME (livre V, section 4) a été mise à jour en conséquence en 2019 et la norme ISO (23865) en 2021.

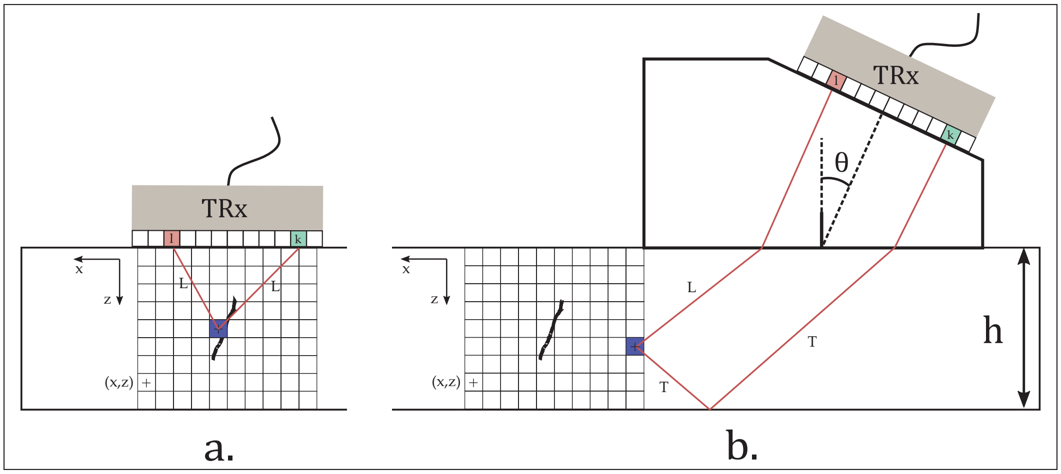

Figure 1.9 Principe du calcul des délais pour un algorithme d'imagerie de type délai et somme pour (a.) une sonde en contact direct avec la pièce et (b.) une sonde couplée à un sabot

1.3.2 Imagerie multivues

1.3.2.1 Principe

L'imagerie multivues (ou multi-modes) est une extension de la TFM (Zhang, Drinkwater, Wilcox & Hunter, 2010) à cela près qu'elle prend en considération des temps de vol plus complexes. Ainsi la Figure 1.9a. illustrait les temps de vol pour aller d'un élément de la sonde à un pixel, puis d'un pixel à un élément directement. Dans le cas de l'imagerie multivues, les temps de vols peuvent différer 1- selon le mode de propagation impliqué (longitudinal ou transversal), 2- selon le nombre de rebonds effectués par l'onde sur le fond de la pièce (ce qui présuppose de connaître la géométrie de la pièce à inspecter). Cette technique trouve majoritairement des applications là encore, dans l'inspection de soudures. La Figure 1.9b. illustre un exemple où on considère un chemin plus complexe pour le parcours de l'onde avec l'ajout d'un sabot. L'onde va d'abord se réfléchir sur le fond de la pièce avant d'attendre le point (ou pixel) d'intérêt. Cette méthode donne lieu à de nombreuses combinaisons de vues possibles avec des modes de propagations différents. Ces combinaisons sont exprimées indépendamment du trajet dans le sabot, s'il est utilisé, puisque la propagation dans celui-ci est toujours considérée selon le mode longitudinal. Ainsi on notera par exemple « TT-T » le mode impliquant un aller jusqu'au fond de la pièce (T), un rebond jusqu'au point (ou pixel) d'intérêt (TT) puis un retour (TT-T) en mode transversal uniquement. Cette nomenclature est d'ailleurs largement employée dans la littérature et dans l'industrie (Budyn, Bevan, Zhang, Croxford & Wilcox, 2019). On retrouve également d'autres appellations pour décrire ces méthodes reposant sur un chemin indirect de l'onde comme "half-skip" ou "full-skip" selon que l'on considère une ou deux réflexions de l'onde sur le fond de la pièce.

La prise en compte de toutes ces vues donne lieu à la reconstruction d'une multitude d'images (d'où l'appellation "multivues") qui ne sont pas toutes pertinentes pour la caractérisation du défaut recherché (Sy, Bredif, Iakovleva, Roy & Lesselier, 2018a). Ainsi, il est nécessaire de trouver une méthode de sélection de ces vues afin d'en extraire le maximum d'information tout en réduisant le temps de calcul nécessaire à leur reconstruction et en facilitant la lecture de l'image finale. Une première piste de recherche visant à traiter cette problématique est la génération de cartes de sensibilité (Budyn *et al.*, 2019; Sy, 2018) permettant de sélectionner la vue ou une portion de la vue la plus appropriée en fonction de la forme, de l'orientation et de la localisation du défaut. Celles-ci sont générées à partir de l'amplitude maximum théorique de l'image TFM à chaque pixel pour un type de défaut donné, connaissant le modèle décrivant sa matrice de diffusion. La Figure 1.10 illustre à cet effet les cartes de sensibilité relatives à de multiples vues et considérant la configuration suivante : une sonde linéaire dont la fréquence centrale est de 7.5 MHz, composée de 60 éléments, sur un sabot incliné de 36° en contact avec une plaque de 3/4" d'épaisseur et considérant une fine fissure de 5 mm de hauteur. Pour cette configuration, on remarque que la vue TT-T semble par exemple la plus appropriée pour une grande partie de la région d'intérêt. La principale limite concernant l'utilisation de ces cartes est la nécessaire connaissance préalable de l'orientation et de la taille du défaut, en faisant une méthode très (trop) spécifique.

Enfin, des travaux ont également été réalisés sur la filtration des artefacts (Iakovleva, Chatillon, Bredif & Mahaut, 2014; Cantero-Chinchilla, Wilcox & Croxford, 2022) qui peuvent apparaître lors de la reconstruction de l'image ainsi que sur l'utilisation de ces différentes vues pour la détection de défauts situés près de la surface (P. Yu, 2017). En somme, bien que le principe de l'imagerie multivues soit simple, le problème majeur reste l'exploitation et la sélection des contributions de chaque vue afin d'établir la meilleure image possible des éventuels défauts.

1.3.2.2 Combinaison des vues

Comme évoqué dans la partie précédente, la sélection des vues pertinentes à l'identification de défauts n'est pas une chose simple. On souhaiterait donc aboutir à une façon de combiner toutes les vues qu'il est possible de reconstruire pour obtenir la meilleure image possible. Aussi, très peu de travaux ont pour l'instant été menés à ce sujet. À notre connaissance, seuls les groupes de recherche de Lesselier et al. et Wilcox et al. ont abordé cette problématique. Ainsi, (Sy, 2018) a proposé plusieurs méthodes envisageables de fusion telles que la fusion par maximum d'amplitude, par sommation ou par corrélation, et ce pour des indications issues de réflexions spéculaires ou de diffractions. Son travail présente également de premiers essais sur des données expérimentales et simulées d'utilisation des cartes de sensibilité pour orienter les opérations de fusion sur des zones particulières de l'image. De manière similaire, on retrouve dans (Bevan *et al.*, 2020) des essais de fusion simple (par sommation) mais également reposant sur l'utilisation des cartes de sensibilité. Une proposition plus poussée (Wilcox *et al.*, 2020) a montré qu'il est possible d'utiliser les cartes de sensibilité en combinaison avec une étude probabiliste afin de fusionner les différentes vues de façon satisfaisante. Encore une fois, la majorité des méthodes de combinaison des vues permettant d'obtenir des résultats probants, reposent sur une connaissance préalable du type de défauts recherché.

1.3.3 Imagerie par cohérence de phase

Comme nous l'avons vu précédemment, la méthode TFM permet grâce à sa focalisation en tout point de la région d'intérêt, de localiser et de dimensionner avec précision de nombreux types de défauts et de discontinuités. De plus, la prise en compte de différentes vues utilisant des combinaisons de modes de propagation longitudinale et de cisaillement sont autant de possibilités que nous pouvons exploiter afin de faciliter l'interprétation de l'information présentée

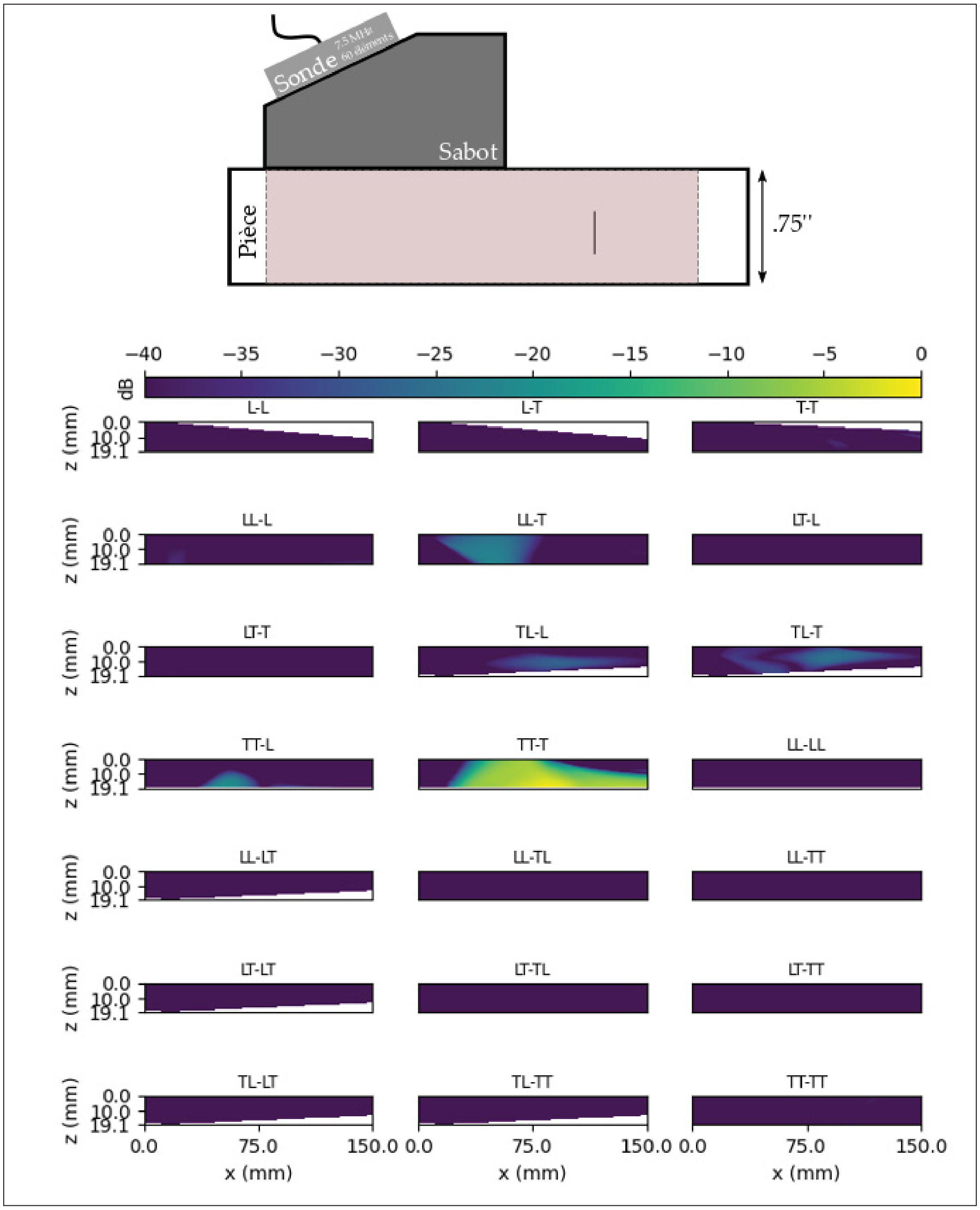

Figure 1.10 Cartes de sensibilité pour de multiples vues considérant une plaque d'acier de $\frac{3}{4}$" d'épaisseur, une fissure verticale fine de 5 mm de hauteur et une sonde linéaire dont la fréquence centrale est de 7.5 MHz, composée de 60 éléments, sur un sabot incliné de 36°

au technicien d'inspection. Cependant, le TFM présente encore des limites dans certaines situations, par exemple lorsqu'il faut distinguer des géométries peu réfléchissantes ou bien dont la taille est petite par rapport à la longueur d'onde, et par opposition des surfaces hautement réfléchissantes comme le fond de la pièce (Lesage, Marvasti & Farla, 2021). Ainsi, de nombreux facteurs et méthodes d'imagerie ultrasonores basées sur la cohérence du signal ont été introduits au cours des dernières années pour améliorer la détectabilité des petits réflecteurs dans divers scénarios tels que les matériaux à forte atténuation, les matériaux anisotropes, etc. Le terme facteur désigne ici en réalité une simple modification du terme sommé dans un algorithme de reconstruction de type DAS, comme celui de la TFM. Nous nous intéresserons particulièrement aux méthodes utilisant la phase du signal pour cette étude. En général, les facteurs basés sur la cohérence sont utilisés sous forme de matrice ou de "carte" pour pondérer les pixels d'une image TFM, mais ils peuvent également être considérés comme des méthodes d'imagerie pertinentes qui se satisfont à elles-mêmes et conduisant à une reconstruction de la ROI ne reposant pas sur l'amplitude du signal (Baiotto, Knight-Gregson, Nageswaran & Clarke, 2018). Plusieurs facteurs de cohérence reposant sur la phase du signal seront ainsi présentés ci-après. Pour chaque cas, un exemple de l'image résultante de l'application de ce facteur ainsi que sa multiplication par l'image TFM, opérant ainsi une pondération de celle-ci, est présenté dans la Figure 1.11.

Rappelons enfin que la phase d'un signal mesurée à un instant t est obtenue, à partir du signal analytique par :

$$\phi_{k,l}(t) = \arctan\left(\frac{\tilde{y}_{k,l}(t)}{y_{k,l}(t)}\right). \tag{1.24}$$

1.3.3.1 Facteur de cohérence de la phase (PCF : Phase Coherence Factor)

Le facteur de cohérence de la phase (PCF : Phase Coherence Factor), basé sur l'analyse de la distribution de la phase du signal mesuré sur chaque élément de la sonde, a été introduit pour la première fois par (Camacho, Parrilla & Fritsch, 2009) et formulé comme suit :

$$I_{PCF}(x,z) = \max\left(0, 1 - \frac{\sigma_{\phi_{k,l}} \times \mu_{PCF}}{\sigma_0}\right), \tag{1.25}$$

où μ_{PCF} est un terme de sensibilité, σ_0 est généralement fixé à $\frac{\pi}{\sqrt{3}}$ et correspond à l'écart type nominal d'une distribution uniforme sur $[-\pi,\pi]$ de la phase et $\sigma_{\phi_{k,l}}$ est l'écart type de la phase instantanée du signal défini comme suit :

$$\sigma_{\phi_{k,l}(\tau_{k,l}(x,z))} = \sqrt{\frac{1}{N_e^2}\sum_{k=1}^{N_e}\sum_{l=1}^{N_e}\phi_{k,l}(\tau_{k,l}(x,z)))^2 - \left(\frac{1}{N_e^2}\sum_{k=1}^{N_e}\sum_{l=1}^{N_e}\phi_{k,l}(\tau_{k,l}(x,z)))\right)^2}. \tag{1.26}$$

Le PCF s'est avéré pertinent pour l'amélioration du rapport signal à bruit (SNR : Signal to Noise Ratio) dans les matériaux granuleux (Camacho & Fritsch, 2011b) lorsqu'il est utilisé comme facteur de pondération de la TFM ainsi que pour les applications d'imagerie par ondes planes (PWI : Plane Wave Imaging) (Cruza, Camacho & Fritsch, 2017). Baiotto et al. (Baiotto *et al.*, 2018) ont également étudié l'influence du μ_{PCF} sur l'image résultante et ont également considéré l'utilisation du PCF comme une image en lui-même. La Figure 1.11a. présente un exemple de PCF et le résultat de la pondération d'une image TFM par celui-ci.

1.3.3.2 Facteur de cohérence du signe (SCF : Sign Coherence Factor)

Certainement l'un des facteurs de cohérence les plus cités, le facteur de cohérence du signe (SCF : Sign Coherence Factor) a été introduit dans (Camacho *et al.*, 2009) comme un cas particulier du PCF reposant sur une version binarisée des signaux mesurés par les éléments de la sonde. Ainsi, la phase instantanée du signal est représentée par un seul bit $y^B(t)$ dérivé des traces temporelles brutes :

$$y^B(t) = \begin{cases} -1, & \text{if } y(t) < 0 \\ +1, & \text{if } y(t) \geq 0 \end{cases} . \tag{1.27}$$

Ensuite, de manière similaire au PCF, l'écart-type de $y^B(t)$ est évalué et le SCF est donnée par :

$$I_{SCF(x,z)} = \left| 1 - \sqrt{1 - \left[\frac{1}{N_e^2} \sum_{k=1}^{N_e} \sum_{l=1}^{N_e} y^B(\tau_{k,l}(x,z)) \right]^2} \right|^{\mu_{SCF}} , \tag{1.28}$$

où μ_{SCF} est un terme de sensibilité. Le principal avantage de cette méthode est sa simplicité et donc son efficacité en termes de calcul. Elle est préférée pour les applications en temps réel même si elle présente des discontinuités pour la représentation des réflecteurs, comme le PCF. Le SCF s'est avéré être un outil fiable pour produire simplement une carte de cohérence pour des matériaux à gros grains (Camacho & Fritsch, 2011b; Knight-Gregson, Peyton, Scully, Weston & Davis, 2016) et plus généralement anisotropes et inhomogènes (Baiotto *et al.*, 2018), pour les applications en imagerie par ondes planes (PWI : Plane Wave Imaging) (Lokesh B & Thittai, 2016; Cruza *et al.*, 2017), le dimensionnement des fissures (Camacho, Atehortua, Cruza, Brizuela & Ealo, 2018) et également pour les applications en ondes guidées (Prado, Higuti, Kitano, Martínez-Graullera & Adamowski, 2013; Lyu, Hong, Song & He, 2021). Lorsque le SCF est utilisé indépendamment comme une image en lui-même, on parle généralement d'imagerie par cohérence de signes (SCI : Sign Coherence Imaging) (Camacho *et al.*, 2018). La Figure 1.11b. présente un exemple de SCF et le résultat de la pondération d'une image TFM par celui-ci.

1.3.3.3 Facteur de cohérence circulaire (CCF : Circular Coherence Factor)

Le facteur de cohérence circulaire (CCF : Circular Coherence Factor) a été introduit par (Camacho & Fritsch, 2011a) comme un indicateur plus strict en termes de focalisation (par rapport au PCF) (Camacho & Fritsch, 2011b), reposant sur l'écart-type de la variable complexe

$X = e^{i\phi}$, la phase ayant une distribution circulaire, et définie par :

$$I_{CCF(x,z)} = 1 - \sqrt{Var(\cos(\phi_{k,l}(\tau_{k,l}(x,z)))) + Var(\sin(\phi_{k,l}(\tau_{k,l}(x,z))))}, \tag{1.29}$$

où $Var(\cdot)$ est l'opérateur de variance appliqué aux composantes instantanées en quadrature ou en phase du signal comme suit :

$$\begin{aligned} Var(\cos(\phi_{k,l}(\tau_{k,l}(x,z)))) = \frac{1}{N_e^2} \sum_{k=1}^{N_e} \sum_{l=1}^{N_e} \cos^2(\phi_{k,l}(\tau_{k,l}(x,z))) \\ - \left(\frac{1}{N_e^2} \sum_{k=1}^{N_e} \sum_{l=1}^{N_e} \cos(\phi_{k,l}(\tau_{k,l}(x,z))) \right)^2. \end{aligned} \tag{1.30}$$

Le CCF produit un facteur de cohérence ayant une apparence plus continue et plus lisse que le PCF ; il a été utilisé dans (Zhang, Drinkwater & Wilcox, 2013b), avec le SCF, pour pondérer une image TFM. Dans cette dernière étude, l'image résultante était appelée imagerie par cohérence de phase (PCI : Phase Coherence Imaging) et présentait un meilleur rapport signal/bruit (SNR) que la TFM ordinaire non pondérée tout en induisant une distorsion pour l'imagerie de fissures. Cependant, en raison de sa complexité de calcul et de sa sensibilité aux petits déphasages (Cruza *et al.*, 2017; Camacho, Fritsch, Fernandez-Cruza & Parrilla, 2019), des facteurs plus simples et plus pertinents ont été privilégiés au fil des ans. La Figure 1.11c. présente un exemple de CCF (on peut remarquer l'aspect plus lissé des indications par rapport au SCF ou PCF) et le résultat de la pondération d'une image TFM par celui-ci.

1.3.3.4 Facteur de cohérence vectorielle (VCF : Vector Coherence Factor)

Formulé et mentionné pour la première fois dans (Martínez-Graullera, Romero-Laorden, Martín-Arguedas, Ibañez & Ullate, 2012), puis nommé Vector Coherence Factor (VCF) dans (Cruza *et al.*, 2017), ce facteur constitue un bon compromis entre la caractéristique discontinue du PCF et la complexité de calcul du CCF tout en conservant son aspect visuel "lissé". En effet, il repose sur le calcul du module d'un ensemble de vecteurs unitaires dans le plan complexe défini par les phases instantanées. On le retrouve ainsi dans de nombreuses formulations différentes, mais équivalentes (Martínez-Graullera *et al.*, 2012; Camacho *et al.*, 2019; Cruza *et al.*, 2017; Zhang *et al.*, 2020; Gauthier, Painchaud-April, Le Duff & Bélanger, 2021; Lesage *et al.*, 2021; Gauthier *et al.*, 2021) :

$$\begin{aligned} I_{VCF(x,z)} &= \frac{1}{N_e^2}\sqrt{\left(\sum_{k=1}^{N_e}\sum_{l=1}^{N_e}\frac{\mathrm{Re}(\tilde{y}_{k,l}(\tau_{kl}(x,z)))}{|\tilde{y}_{k,l}(\tau_{kl}(x,z))|}\right)^2+\left(\sum_{k=1}^{N_e}\sum_{l=1}^{N_e}\frac{\mathrm{Im}(\tilde{y}_{k,l}(\tau_{kl}(x,z)))}{|\tilde{y}_{k,l}(\tau_{kl}(x,z))|}\right)^2} \\ &= \frac{1}{N_e^2}\sqrt{\left(\sum_{k=1}^{N_e}\sum_{l=1}^{N_e}\sin\left(\phi_{kl}(\tau_{kl}(x,z))\right)\right)^2+\left(\sum_{k=1}^{N_e}\sum_{l=1}^{N_e}\cos\left(\phi_{kl}(\tau_{kl}(x,z))\right)\right)^2} \\ &= \frac{1}{N_e^2}\left|\sum_{k=1}^{N_e}\sum_{l=1}^{N_e}\frac{\tilde{y}_{k,l}(\tau_{kl}(x,z))}{|\tilde{y}_{k,l}(\tau_{kl}(x,z))|}\right| \\ &= \frac{1}{N_e^2}\left|\sum_{k=1}^{N_e}\sum_{l=1}^{N_e}\mathrm{e}^{i\phi_{k,l}(\tau_{kl}(x,z))}\right|. \end{aligned} \tag{1.31}$$

Le VCF était également appelé facteur de cohérence de phase instantanée (IPCF : Instantaneous Phase Coherence Factor) dans (Zhang *et al.*, 2020) où un terme de sensibilité sous forme d'exposant a été ajouté, de la même manière que pour le SCF. Lorsque ce facteur n'est pas utilisé pour pondérer une image TFM mais utilisé en tant qu'image, on parle, à tort, d'imagerie par cohérence de phase instantanée (IPCI : Instantaneous Phase Coherence Imaging) dans (Gauthier *et al.*, 2021) et également d'imagerie par cohérence vectorielle (VCI : Vector Coherence Imaging) dans (Lesage *et al.*, 2021). À la différence que, pour le VCI, le VCF est d'abord transformé afin de refléter le contenu de l'information de Shannon suite à la sommation effectuée. Enfin, la Figure 1.11d. présente un exemple de VCF (à novueau, on peut remarquer l'aspect plus lissé des indications par rapport au SCF ou PCF) et le résultat de la pondération d'une image TFM par celui-ci. Le VCF sera le facteur privilégié pour la suite de cette étude et sera utilisé pour produire directement des images. On parlera alors d'imagerie VCF.

1.4 Application industrielle

Lors de la construction d'un oléoduc ou d'un gazoduc, les différents tronçons de tubes sont assemblés par des soudures dites circonférentielles, généralement réalisées à l'aide d'un robot.

La géométrie des extrémités des tronçons de tubes est préalablement préparée afin de faciliter la réception du cordon de soudure par la réalisation d'un chanfrein. On retrouve plusieurs géométries pour ces chanfreins, principalement celles en "V" et en "J". Dans cette étude, nous nous intéresserons tout particulièrement aux soudures réalisées sur des chanfreins en "J" qu'on retrouve majoritairement lors de fabrication de pipeline. Lors de la réalisation de la soudure, le robot va parcourir plusieurs fois la circonférence de l'interface entre deux tubes afin de venir la faire fondre localement et remplir le chanfrein de métal en fusion, passe après passe. L'inspection des soudures circonférentielles par des méthodes de contrôle non destructif ultrasonore, qui fait l'objet de la présente étude, est généralement effectuée juste après la réalisation de la soudure. De la même manière que lors de la réalisation du cordon de soudure, un robot d'inspection parcourt la circonférence de l'interface soudée des deux tubes (Ma, Wang, Li & Chang, 2011; Putsherry & Misra, 2018), muni de sondes monoélément et multiéléments comme illustré dans la Figure 1.12a., on parle alors d'inspection ultrasonore automatisée (AUT : Automated Ultrasonic Testing). Les sondes sont placées face à face, de chaque côté du cordon de soudure afin d'assurer un maximum de couverture de la zone à inspecter. L'objectif de l'inspection est la détection et la caractérisation des défauts les plus couramment identifiés dans les soudures, comme présenté dans la Figure 1.12b..

Actuellement, l'information présentée au technicien d'inspection provient à la fois des sondes monoélément utilisant la technique dite de diffraction par temps de vol (TOFD : Time-of-Flight Diffraction) ainsi que des sondes multiéléments utilisant des méthodes conventionnelles, comme le balayage sectoriel, à travers une méthode dite de discrimination par zone (Chapuis & Jenson, 2014). Cette méthode de discrimination par zone consiste simplement à cibler différentes zones le long du chanfrein de la soudure lors de la réalisation de la mesure par une série de tires, comme illustré dans la Figure 1.13a.. L'information issue des différentes méthodes est, dans le cas de la solution proposée par notre partenaire industriel, affichée sous forme de multiples graphiques composés de seuils colorés permettant d'identifier rapidement les irrégularités. Cependant, cet affichage demeure bien plus difficile à interpréter que d'autres méthodes de contrôle non destructif, comme illustré dans la Figure 1.13b. où une même fissure est représentée par radiographie, micrographie et par les graphiques produits à l'issue des mesures effectuées par le robot d'inspection ultrasonore. Rappelons en revanche que dans ce cas, la micrographie est une méthode destructive.

De cette dernière observation est venue la motivation de la présente étude visant à simplifier l'information fournie au technicien à travers l'inspection ultrasonore automatisée réalisée par le robot. En effet, les dernières avancées en matière d'algorithmes d'imagerie et d'électronique ainsi que les possibilités offertes par l'imagerie VCF permettent d'envisager l'utilisation du même robot et de la même configuration pour les sondes tout en produisant des images plus détaillées.

1.5 Conclusion et présentation des articles

Dans ce chapitre, nous avons pu voir que l'imagerie ultrasonore a largement évolué ces dernières années et que des méthodes précédemment réservées au domaine de la recherche, comme la TFM, son maintenant rendues possibles sur des appareils commerciaux. De plus, des méthodes dérivées de la TFM, comme l'imagerie VCF, reposant uniquement sur la mesure de la phase du signal, présentent des particularités intéressantes tant sur la facilité de leur mise en oeuvre, que sur leur sensibilité aux petits défauts diffractifs. Ces nouvelles méthodes, combinées à l'imagerie multivues, ouvrent la voie à une amélioration importante de l'information fournie au technicien d'inspection à travers l'image qui est produite par le système d'acquisition. En effet, une image plus détaillée et plus proche d'une image naturelle, comme c'est le cas pour les méthodes radiographiques, permettrait, par exemple, d'assurer une adoption plus large des méthodes par ultrasons pour l'inspection des soudures circonférentielles. Trois articles qui abordent cette problématique sont présentés dans la suite de ce document. Ces articles visent à répondre à l'objectif principal de l'étude qui est le développement de nouvelles techniques d'imagerie pour les soudures circonférentielles, à travers trois sous-objectifs :

- Évaluer les performances, les avantages et les inconvénients de nouvelles méthodes d'imagerie, dont celle utilisant le VCF, comparativement aux méthodes conventionnelles d'imagerie ou de contrôle par ultrasons.
- Optimiser les nouvelles méthodes proposées vis-à-vis du temps d'inspection et de la quantité de données générée.
- Développer une méthode permettant de synthétiser et optimiser l'information issue de l'imagerie multivues.

Le premier article, présenté dans le Chapitre 2, s'intéresse à la technique de diffraction par temps de de vol (TOFD), utilisée par les robots d'inspection de soudures circonférentielles en complément de l'inspection par discrimination zonale par sonde multiéléments. Dans cette étude, les performances de la méthode TOFD sont comparées à celles offertes par l'imagerie VCF pour ce qui est du dimensionnement de fissures. Les résultats des deux méthodes sont très similaires et permettent ainsi de considérer de ne plus utiliser la méthode TOFD en complément de l'imagerie multiéléments si l'imagerie VCF est choisie.

Le deuxième article, présenté dans le Chapitre 3, s'intéresse aux possibilités offertes par l'imagerie VCF en ce qui a trait à la réduction de la quantité de données générées lors de l'acquisition des signaux. En effet, l'un de désavantage de l'acquisition FMC, nécessaire à l'utilisation de l'imagerie VCF, est la quantité importante de données générées comparée aux méthodes multiéléments conventionnelles. L'imagerie VCF reposant uniquement sur la phase du signal, il est montré qu'il est possible, à partir d'un signal binaire ou simplement des fronts montants du ce dernier, de réduire de façon importante la quantité de données générées. Dans cette étude, la reconstruction de la phase du signal à partir d'une acquisition "légère", reposant sur un signal binarisé, permet d'obtenir des images VCF extrêmement proches de celle générée avec une acquisition FMC classique et donc plus "lourde". Ces résultats permettent également de considérer l'utilisation d'une électronique beaucoup plus simple, comme des comparateurs, et donc aussi beaucoup moins dispendieuse.

Enfin, le troisième article, présenté dans le Chapitre 4, traite de la fusion des images VCF issues de l'imagerie multivues. Il est montré que, à la différence des images reposant sur l'amplitude du signal, comme lorsque la méthode TFM classique est employée, des méthodes de fusion simples peuvent être considérées pour les différentes vues. En effet, puisque l'atténuation du signal n'affecte pas l'intensité des pixels des différentes vues (mais seulement la cohérence de la phase), des méthodes simples de fusion comme la sommation pixel par pixel, ou bien la sélection du maximum d'intensité des pixels entre les différentes vues, peuvent être considérées. De plus, cette étude montre que le bagage statistique qui accompagne le VCF permet de définir un seuil efficace permettant de filtrer une grande partie du bruit de fond sur les images produites. Ainsi, par l'utilisation de ce seuil, le contraste de l'image fusionnée issue des différentes vues est grandement amélioré.

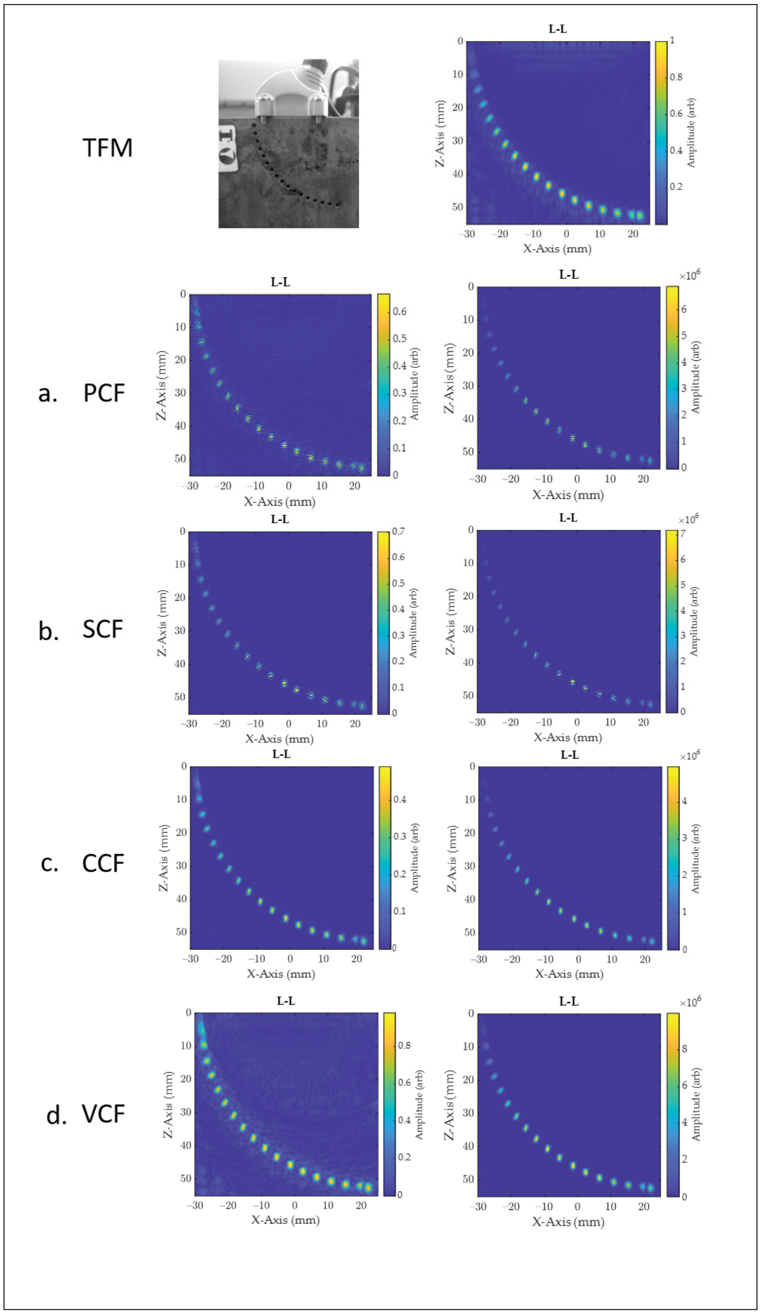

Figure 1.11 Image TFM et sa pondération par (a.) le Phase Coherence Factor (PCF), (b.) le Sign Coherence Factor (SCF), (c.) le Circular Coherence Factor (CCF) et (d.) le Vector Coherence Factor (VCF). Acquisition réalisée à l'aide d'une sonde linéaire de 32 éléments, 5 MHz, en contact avec un bloc d'acier percé de trous sur le côté de 2 mm de diamètre

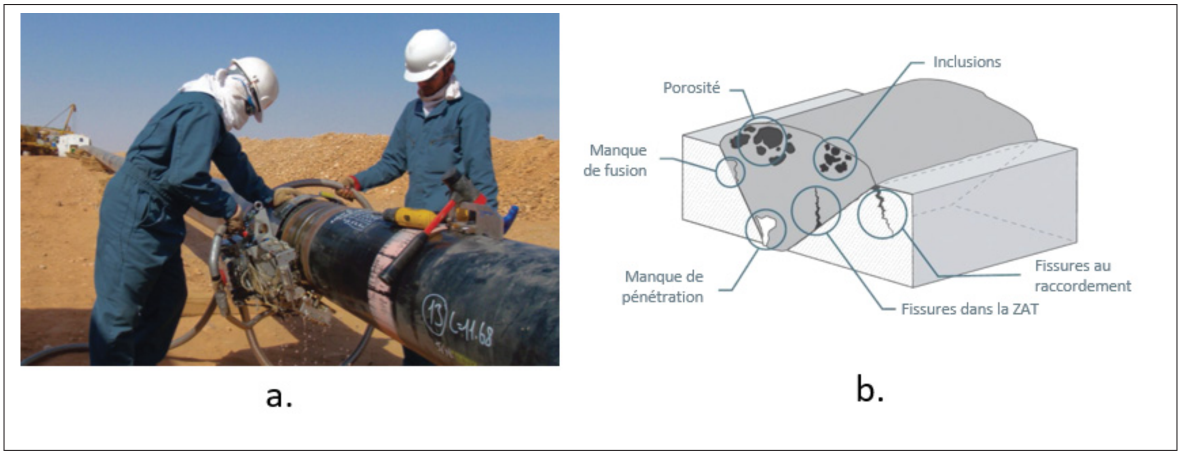

Figure 1.12 Photo présentant l'inspection robotisée d'une soudure circonférentielle (a.) et les différents défauts que l'on cherche à identifier dans une soudure (b.)
Adaptée de Olympus (2014)

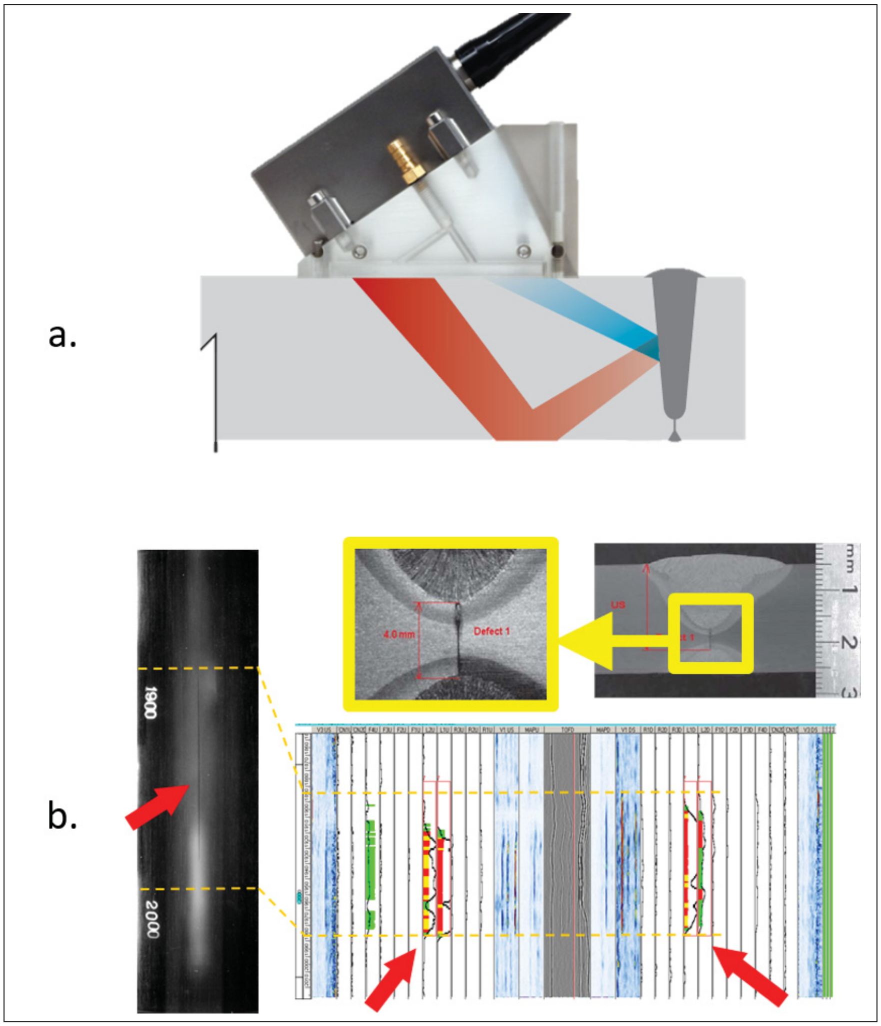

Figure 1.13 Principe d'un scan par discrimination zonale d'une soudure (a.) et représentation d'une fissure par différentes méthodes (b.) : radiographie (à gauche), micrographie (en haut) et par robot d'inspection ultrasonore (en bas)
Adaptée de Olympus (2014)

CHAPITRE 2

TOWARDS AN ALTERNATIVE TO TIME OF FLIGHT DIFFRACTION USING INSTANTANEOUS PHASE COHERENCE IMAGING FOR CHARACTERIZATION OF CRACK-LIKE DEFECTS

Baptiste Gauthier[1] , Guillaume Painchaud-April[2] , Alain Le Duff[2] , Pierre Bélanger[1]

[1] PULETS, Département de Génie Mécanique, École de Technologie Supérieure, 1100 Notre-Dame Ouest, Montréal, Québec, Canada H3C 1K3
[2] Evident Industrial, 3415 Rue Pierre-Ardouin, Québec, Québec, Canada G1P 0B3

Article publié dans «MDPI - Sensors», Janvier 2021.
https ://doi.org/10.3390/s21030730

Données, codes et matériel supplémentaire : https://pulets.ca/open-data/sensors-1058594

2.1 Abstract

Time of flight diffraction (TOFD) is considered a reliable non-destructive testing method for the inspection of welds using a pair of single-element probes. On the other hand, ultrasonic phased array imaging has been continuously developed over the last couple of decades, and now features powerful algorithms, such as the total focusing method (TFM) and its multi-view approach to rendering detailed images of inspected parts. This article focuses on a different implementation of the TFM algorithm, relying on the coherent summation of the instantaneous signal phase. This approach presents a wide range of benefits, such as removing the need for calibration, and is highly sensitive to defect tips. This study compares the sizing and localization capabilities of the proposed method with the well-known TOFD. Both instantaneous phase algorithm and TOFD do not take advantage of the signal amplitude. Experimental tests were performed on a ¾”-thick steel sample with crack-like defects at different angles. Phase-based imaging techniques showed similar characterization capabilities as the standard TOFD method. However, the proposed method adds the benefit of generating an easy-to-interpret image that can help in localizing the defect. These results pave the way for a new characterization approach, especially in the field of automated ultrasonic testing (AUT).

2.2 Introduction

Welds are used in a wide range of industries to assemble metal parts, such as pipes and plates. Their integrity is crucial to providing the safe and efficient operation of safety-critical components (Groover, 2007). Whether originating from the manufacturing process or in-service operations, defects can lead to dramatic failures if not detected at an early stage. Cracks, porosities, and lack of fusion are among the common discontinuities that have been observed in welds. Ultrasonic inspection techniques (UT) are among the most common methods used to identify and characterize such defects. For the inspection of girth welds, the typical inspection setup comprises conventional ultrasonic phased array (PA) probes and additional time of flight diffraction (TOFD) transducers operating at higher frequencies (Moles, Dubé, Labbé & Ginzel, 2005). Introduced in the early 1970s for nuclear industry vessels, TOFD relies on a pitch-catch configuration, in which diffracted ultrasonic energy allows accurate sizing of defects. However, this technique presents some limitations, notably related to the interpretation and localization of indications, important dead zones, and a strong signal attenuation (Charlesworth & Temple, 2001). On the other hand, conventional phased array ultrasonic testing methods, which have long been used for linear or raster scanning, are also very interesting for their electronic scanning capabilities. Indeed, such techniques allow almost any type of acquisition scheme to steer, focus, or sub-aperture the ultrasonic beam that is sent to the sample. Particularly, the full matrix capture (FMC) (Holmes *et al.*, 2005; Drinkwater & Wilcox, 2006) data acquisition scheme, and its total focusing post-processing method (TFM) (Schmerr Jr, 2015; Jeune, Robert, Dumas, Membre & Prada, 2015) have proven to be reliable, and provide easy-to-understand images, while using conventional probing hardware (Fan, Caleap, Pan & Drinkwater, 2014; Han, Wu, Li & Lin, 2014). Recently, the multi-view (or multi-mode) technique, using various combinations of ray path, backwall reflections, and mode conversions, has been explored (Zhang *et al.*, 2010; Zhang, Shen, Demirli & Amin, 2012; P. Yu, 2017). This technique mimics virtual probes, which should allow imaging of the same defect from different points of views. However, it also comes with some drawbacks, as the large number of views that can be considered can rapidly increase the complexity. Thus, at the time of writing, the selection of the relevant modes to image a given defect is highly reliant on the inspector's experience. Among the different strategies that are currently being developed to overcome such complexity, sensitivity maps (Budyn *et al.*, 2019; Sy *et al.*, 2018a; Sy, Brédif, Iakovleva, Roy & Lesselier, 2018b) and fusion of views (Sy *et al.*, 2018a) are very promising, but even they still rely on known defect characteristics. While conventional TFM consists of the summation of time domain amplitude signals, the phase of signals can however also be fed directly to delay and sum algorithms for image reconstruction, or as a weighting factor (Camacho *et al.*, 2009). Additionally, since defect sizing currently relies on calibrated amplitude, direct phase-based image reconstruction allows a different approach, in which calibration is no longer a requirement, as amplitude information is simply disregarded. It appears that in the case of narrow defects, tips are particularly well represented in such images, which allow accurate sizing and localization of reflectors (Camacho *et al.*, 2018). In this paper, instantaneous phase coherence imaging (IPCI) and conventional TFM are compared to TOFD. This comparison was motivated by the fact that both the IPCI and TOFD methods are not based on amplitude to detect and size indications. Performance, in terms of sizing and localization of notch-like defects, was compared and assessed on a low-carbon steel plate. The rest of the paper is divided as follows : Section 2 presents the materials and methods, including : a description of TOFD and its limitations, the instantaneous coherence imaging algorithm, as well as the experimental setup. Experimental results from different methods are depicted in Section 3, followed by a discussion in Section 4. Finally, conclusions are presented in Section 5.

2.3 Materials and methods

2.3.1 Time of Flight Diffraction and Its Limitations

In this section, TOFD is briefly introduced, and known limitations of the method are presented and discussed. As illustrated in Figure 2.1a, TOFD commonly relies on the use of two single-element probes on opposite sides of a region of interest acting in a pitch-catch configuration, with emitter Tx and receiver Rx. The distance between the center of the probes, s, also called

PCS (probe center spacing), can be calculated by :

$$s = 2 \times d \times \tan(\theta) \tag{2.1}$$

where d is the depth of focus, and θ the angle of the wedge. For samples of thickness, h, up to 50 mm, θ is usually equal to 60° or 70°, and d is defined by :

$$d = 2/3 \times h \tag{2.2}$$

for adequate coverage (Ginzel, 2013). Taking the example of a defect which has two extremities not breaking to the surface, TOFD is characterized by four well defined echoes (Figure 2.1b). First, the lateral wave (similar to creeping waves, a wave originating at the upper part of the envelope of a compression wave for which propagation occurs at a depth of a few millimeters and parallel to the surface) is recorded, and has the shortest time of flight. If it is not recorded, or received with a weak amplitude, then that is a good indication of a surface crack. Additionally, the lateral wave is often used for assessing coupling conditions and for calibration purposes. Then, when the ultrasonic beam encounters an indication along its path, typically a crack, a part of the energy will be reflected and the remainder diffracted from the tips of the indication, which are then acting like point sources emitting a spherical wavefront. This diffracted pattern will be recorded by the receiving probe, and the upper and lower tip will have a characteristic 180-degree phase shift. Lastly, the reflection of the backwall, with a high amplitude, is received.

2.3.1.1 TOFD Defect Sizing and Localization

The sizing (height) and localization (depth) of the defect can be estimated by measuring the time delay for the signals shown in Figure 1b, and using the knowledge of the sample longitudinal velocity, the wedge delay, and the PCS. Thus, considering an isotropic material, a flaw tip depth, d_i, is given by (Silk, 1987) :

$$d_i = \sqrt{\left(\frac{c\ (t - 2t_0)}{2}\right)^2 - \left(\frac{s}{2}\right)^2} \tag{2.3}$$

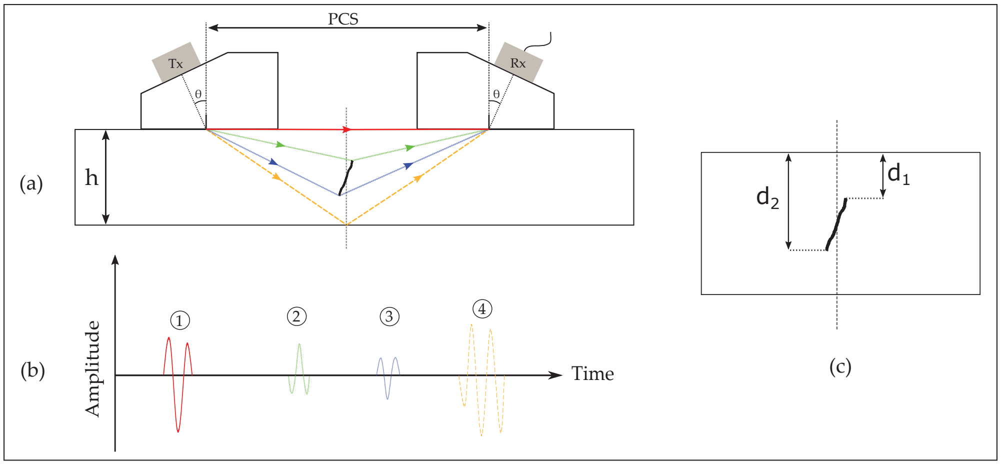

Figure 2.1 Time of flight diffraction principle : (a) setup constituted by two probes in opposition, mounted on a wedge of angle θ. The probes are separated by a distance, PCS (probe center spacing), and placed on a sample of thickness, h ; (b) time traces as recorded by the receiving transducers displaying the lateral wave (1), the upper diffraction response (2), the lower tip diffraction response (3), and the backwall echo (4) ; (c) measurement of the depth and height of a defect

with c being the longitudinal velocity in the sample material, t the total time from the transmitter to the receiver for the flaw tip indication, and t_0 the propagation time in the wedge material. The flaw height, b, can then be expressed as :

$$b = d_2 - d_1 \tag{2.4}$$

where d_1 is the upper tip depth, and d_2 the lower tip depth, as illustrated in Figure 1c. Here, a conventionally adopted assumption is made, that the defect lies exactly midway between the transducers (International, 2019). Additionally, a phase shift of π is observed between the upper and lower tips of the crack (Coffey & Chapman, 1983), enabling easy identification on time traces.

2.3.1.2 TOFD Limitations

Notwithstanding the apparent simplicity of this method and the fact that sizing does not rely on signal amplitude, TOFD presents several limitations that may affect the detectability, sizing, and localization of discontinuities.

2.3.1.2.1 Dead Zones and Spatial Resolution

There are two dead zones (Figure 2.2) related to the ring time, near the surface and the backwall. They can be easily evaluated considering the exciting pulse duration, PCS, and material velocity (Standards, 2009) :

- The lateral wave dead zone limits the detection capabilities directly beneath the surface of the sample. This dead zone usually has a significant depth of 4 to 8 mm (for frequencies in the 5 MHz–15 MHz range and steel samples of thickness below 25 mm) that can be limited by reducing PCS and/or reducing the pulse duration (i.e., using a higher frequency on a highly damped probe).
- The backwall dead zone limits the detection capabilities directly above the backwall of the sample. The thickness of this dead zone is usually less than 1 mm, and must therefore be considered when looking for small defects in this area.

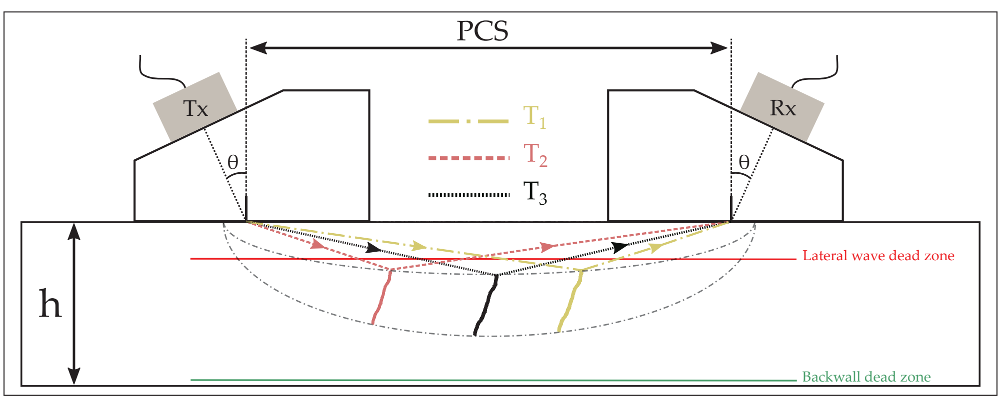

Figure 2.2 Dead zones of time of flight diffraction (TOFD) related to the ring time near the surface (lateral wave dead zone) and the backwall (backwall dead zone). Locus curve (dotted line) showing three possible defect locations for the exact same times of flight (T_1, T_2, and T_3)

Additionally, particular attention should be given to spatial resolution, which decreases with decreasing depth (Ogilvy & Temple, 1983). Thus, the shallowest defect for detection has to be considered when evaluating the acceptability of the method. However, the spatial resolution can be increased by increasing the frequency of the signal or reducing the PCS or pulse width.

2.3.1.2.2 Locus Curve

As mentioned earlier with respect to the localization and sizing of the defect, it is assumed that the defect lies in the middle of the two probes. Additionally, the measurement carried out relies solely on the arrival time of the different echoes. However, and for a given pair of transducers, several defect locations and sizes exist for the exact same recorded time traces. As illustrated in Figure 2.2, if the centers of the probes are considered as the foci of an ellipse, then the dotted line represents the locus of all points having the same travel time, $T_1 = T_2 = T_3$ (Charlesworth & Temple, 2001). Thus, if the defect is not perfectly centered between the two probes, errors can be made when estimating its depth and height.

2.3.2 Instantaneous Phase Coherence Imaging

A different approach, which also allows sizing and localization of defects through an imaging technique, and having the potential to become an alternative solution to traditional TOFD, is presented in this section. Instantaneous phase coherence imaging uses the complete set of signals (FMC) recorded from each pair of emitting elements, i, and receiving elements, j, of a 1-D linear array (Figure 2.3). After data is acquired, each signal is delayed and summed according to the distances between the emitter, the pixel, and the receiver. Finally, the result is mapped to the image domain. This imaging method, known as the total focusing method (TFM) (Holmes *et al.*, 2005), has traditionally relied on the summation of the delayed amplitude of signals. However, the amplitude is affected by numerous phenomena along the wave path, such as diffraction at the probe level, free propagation (i.e., geometric and inhomogeneities scattering losses), interaction with interfaces (i.e., transmission and reflection coefficients, mode conversions), and scattering by the flaw. Although the amplitude correction associated with these factors could be factored out by an appropriate model, the computational complexity may lead to performance issues. Currently, this issue is alleviated by acquiring empirical amplitudes obtained on representative flaws. The complete process, referred to as amplitude calibration, is time consuming and prone to statistical fluctuations (e.g., generically, the acquisition circumstances of the calibration step may differ from the actual inspection step). It is therefore desirable to obtain an imaging process that is less impacted by amplitude-based aberrations. Thus, in this section, an algorithm derived from TFM is presented ; it relies only on the coherent summation of signal instantaneous phase (Camacho *et al.*, 2009). This algorithm has been considered in the past as a weighting factor for amplitude-based images in order to reduce artefacts (Camacho *et al.*, 2018).

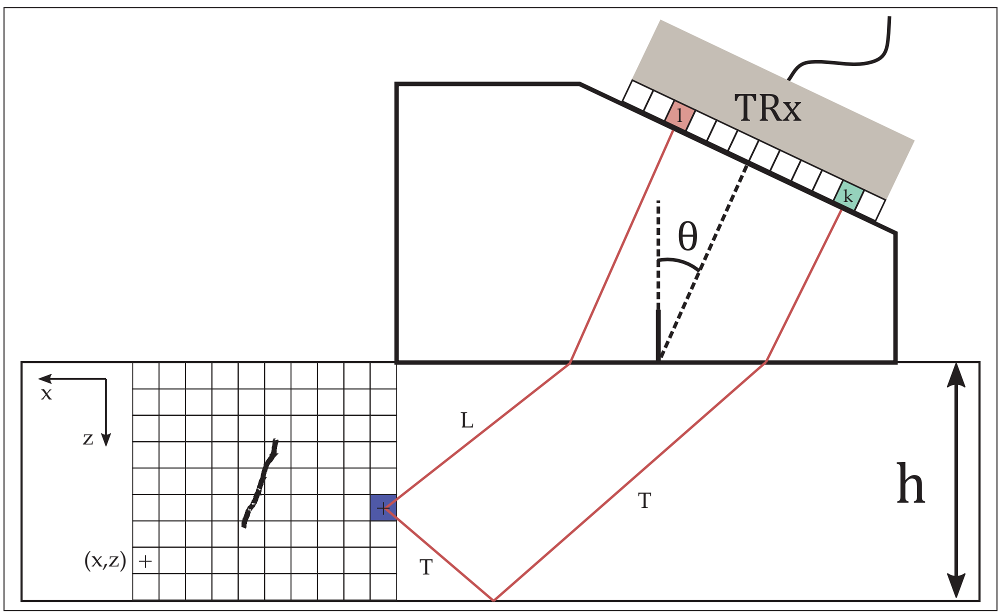

Figure 2.3 Data acquisition principle through full matrix capture (FMC) : a signal is emitted by element i and received by element j. Image reconstruction area is divided into pixels, each one denoted by its position (x,z)

Multi-view imaging is also explored as it has recently proven to be an interesting technique for defect characterization (Zhang *et al.*, 2010; P. Yu, 2017; Han, Wu, Zhang & Wan, 2019). A view is constituted of two ray paths : a transmitting path from the probe to the defect, and a receiving path from the defect to the probe. Each ray path can be composed of both the longitudinal (L) and transverse (T) wave modes, with or without reflection from the backwall. As the first and final legs of the ray path are in the wedge, which is only used for longitudinal wave propagation, they are omitted in the nomenclature (Budyn *et al.*, 2018). For example, the TT-L path is made of a TT half-skip path (transmission) from the probe to the defect, and an L direct path (reception) from the defect to the probe.

Considering a 1-D linear array of N elements, the received signal at element l from an emission at element k is denoted $h_{kl}(t)$ (Figure 2.4a). For a conventional TFM, every pixel intensity, I_{TFM}, of the image located at position (x, z) is obtained by summing the delayed amplitude of the signal (Holmes *et al.*, 2005) :

$$I_{TFM}\,(x,z) = \left|\sum_{k=1}^{N}\sum_{l=1}^{N}\hat{h}_{kl}(\tau_{kl}\,(x,z))\right| = \left|\sum_{k=1}^{N}\sum_{l=1}^{N}\left|\hat{h}_{kl}(\tau_{kl}\,(x,z)\right| e^{i\phi_{kl}(\tau_{kl}(x,z))}\right| \tag{2.5}$$

with $\hat{h}_{kl}\,(t)$ being the Hilbert transform of $h_{kl}(t)$, and $\tau_{kl}\,(x, z)$ the total time of flight from the transmitting to the receiving element for the considered view. In the case of IPCI, every pixel intensity, I_{IPCI}, of the image located at position (x, z) is obtained by summing the delayed in-phase and quadrature components of signals (Zhang *et al.*, 2020) :

$$I_{IPCI}\,(x,z) = \frac{1}{N^2}\left(\left(\sum_{k=1}^{N}\sum_{l=1}^{N}\sin(\phi_{kl}(\tau_{kl}\,(x,z))\right)^2 + \left(\sum_{k=1}^{N}\sum_{l=1}^{N}\cos(\phi_{kl}(\tau_{kl}\,(x,z))\right)^2\right)^m \tag{2.6}$$

with ϕ_{kl} being the instantaneous phase of the signal (Figure 2.4b) defined by :

$$\phi_{kl}\,(t_{kl}) = \arctan\left(\frac{\hat{h}_{kl}\,(t_{kl})}{h_{kl}\,(t_{kl})}\right). \tag{2.7}$$

Exponent m in Equation (2.6) is used as a modulation factor to increase or decrease the sensitivity to side lobes and reduce the main lobe. In this paper, the typical value of $m = 0.5$ is used, which corresponds to the envelope of the instantaneous phase. Thus, Equation (2.6) can be rewritten in a simpler form as :

$$I_{IPCI}\,(x,z) = \left|\sum_{i=k}^{N}\sum_{j=l}^{N} e^{i\phi_{kl}(\tau_{kl}(x,z))}\right|. \tag{2.8}$$

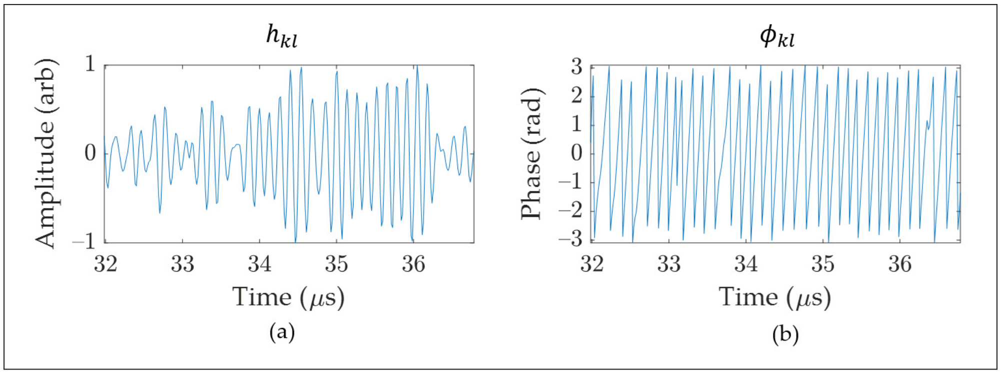

Figure 2.4 Sample time traces for : (a) amplitude signal, h_{kl}, and (b) instantaneous phase, ϕ_{kl}

The underlying principle supporting IPCI is the coherence of the phase when adequately delayed signals are summed. The scattered wave resulting from the interaction with a flaw propagates back and is received by each element of the probe. Compared to the phase resulting from the backscattering from a continuous distribution of random minor inhomogeneities in the material, it is assumed that a single major inhomogeneity, a flaw for instance, will produce a more coherent phase structure over the detection array. Hence, the summation of a large number of appropriately delayed coherent signals would result in a large response, in comparison to the summation of many random responses from lesser material inhomogeneities. Interesting properties can then be deduced from the principle of IPCI. The following subsections present three of them, considering only the L–L view for convenience and brevity.

2.3.2.1 Noise Level Sensitivity

Unlike conventional TFM, IPCI is conditional on the existence of a certain level of noise in the input signals. Indeed, if received signals are composed of perfectly equal or zero valued parts, those parts will be coherent, and hence produce artefacts in the final image (Figure 2.5). Additionally, the restitution of a given scatterer will also be affected by this noise level. To illustrate this behavior, three simple finite element simulations were conducted, modeling a 5 MHz (64 element) 0.5 mm pitch probe positioned above a low-carbon steel sample of dimensions 100 mm × 50 mm, as illustrated in Figure 2.6a.The three simulations successively modeled a side drilled hole (SDH) of a diameter of 0.4 mm located at different depths (simulation 1 :25 mm ; simulation 2 :50 mm ; and simulation 3 :75 mm). For each simulation, a 3 cycle Hann windowed toneburst, centred at 5 MHz, was transmitted, and the FMC was recorded and then used as input data for IPCI and TFM. Absorbing boundaries were added to the sample sides so as to prevent unwanted reflections and associated artefacts. Simulations were carried out using the Pogo FEA solver (Huthwaite, 2014), which allows fast computing of such configurations thanks to its GPU based architecture.

In reality, noise can originate from the acquisition chain, the properties of the material under inspection, or both (Fan *et al.*, 2014). Usually, electronic noise is alleviated by averaging over time, while the material noise is difficult to attenuate. Gaussian noise, with a signal-to-noise ratio (SNR) of either 5 dB, 10 dB, 15 dB, or 20 dB, was added to raw time traces during post processing for the purpose of this demonstration. This noise, as well as the raw time traces, were also filtered using a bandpass Butterworth filter between 2.5 MHz (half of the transducer central frequency) and 10 MHz (twice the transducer central frequency), so as to reflect a realistic inspection, and in accordance with the new ISO 23865 standard for TFM inspection. Figure 2.5 illustrates the influence of noise on the reconstructed images for both TFM and IPCI. For both algorithms, the image of the central scatterer (simulation 1) was computed for a noiseless case and for a SNR of 10 dB. A gamma correction factor of 0.5 was applied to images, and a linear scale was used to help the visualization by the reader. For IPCI, the noiseless case shows, as expected, a high level of background noise, due to the high level of coherence outside of the scatterer, while TFM remains lightly affected ; many elementary time series with 0 amplitude on all noiseless elementary time series produced large summation values when Equation (2.8) was applied.

Figure 2.6b,c shows the reconstructed images (both IPCI and TFM) for the three simulations and a 10 dB SNR. A similar behavior was observed, as the geometrical spreading tends to increase the horizontal extent of indications with increasing depth in both IPCI and TFM. Additionally, the vertical extent of the indications was smaller for TFM than IPCI. However, restitution of the scatterer differed slightly when changing the noise level to other values. Thus, the array

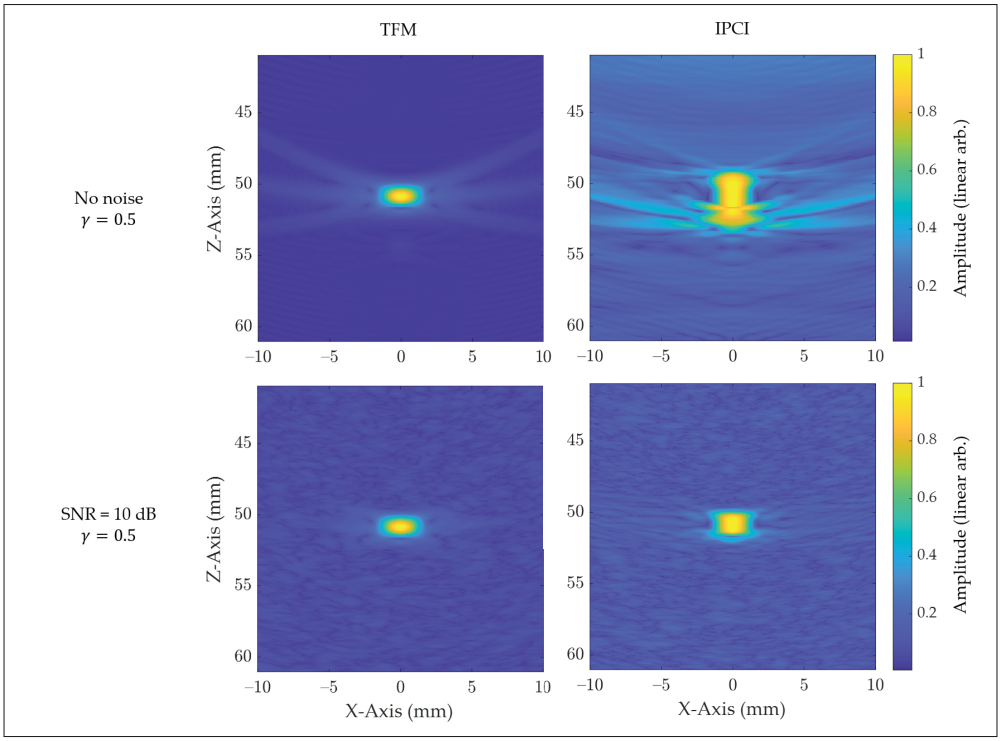

Figure 2.5 Simulated noise sensitivity for a point like scatterer, using both instantaneous phase coherence imaging (IPCI) and the conventional total focusing method (TFM). The upper row images were generated using raw time traces, while the lower row images where generated with a signal-to-noise ratio (SNR) of 10 dB. A gamma correction factor of 0.5 was applied to all images

performance indicator (API) (Holmes *et al.*, 2005) was calculated for all noise levels and simulations. Table 2.1 depicts that, with increasing SNR, the API tended to increase when using IPCI, while remaining at acceptable levels. On the other hand, the API was almost unchanged for any noise level when using TFM.

Given that the noiseless case would only be encountered in a simulated inspection, IPCI qualifies for most experimental studies, as a minimal noise level will always be present.

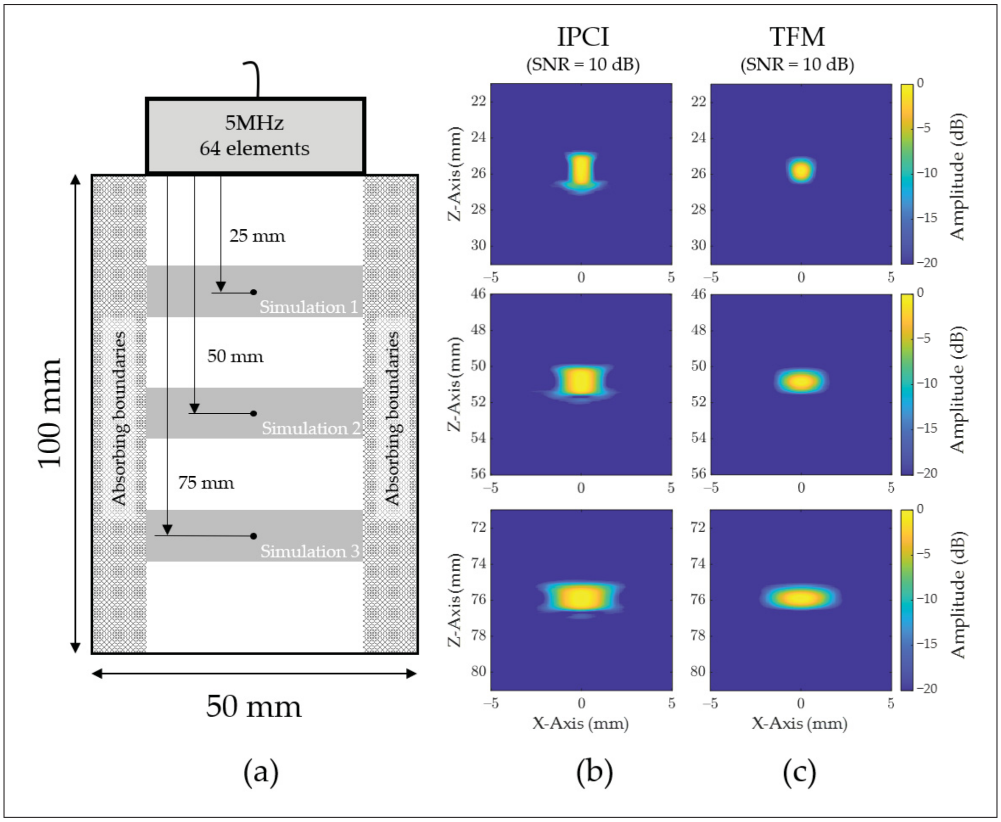

Figure 2.6 Simulated noise level sensitivity analysis principle for a point like scatterer, using both IPCI and conventional TFM : (a) simulation setup showing the 3 different simulations that were conducted, modeling a 5 MHz, 64 element probes and 0.4 mm diameter side drilled holes ; (b) images obtained for each scatterer, and each simulation using IPCI and an added band-limited Gaussian noise with a SNR of 10 dB ; (c) images obtained for each scatterer, and each simulation using TFM and an added 10 dB Gaussian noise

2.3.2.2 Attenuation Robustness

IPCI is by definition an amplitude free imaging method. Indeed, the coherent summation of signals happens independently of the amplitude of the signals, and hence produces indications with a high contrast level. This is particularly useful when the appropriate gain to be used for ensuring the detection of a given flaw is unknown. To illustrate this property, an experimental study was conducted in which a 5 MHz (32 element) 1 mm pitch probe was positioned above an ASTM E2491 low-carbon steel test block (Figure 2.7a). The FMC was acquired and then used

Tableau 2.1 Noise level sensitivity analysis results for a point like scatterer using both IPCI and conventional TFM algorithms where array performance indicator (API) was computed for each simulated configuration

	SNR	**Simulation 1**	**Simulation 2**	**Simulation 3**
TFM	5 dB	0.54	0.93	1.35
	10 dB	0.54	0.94	1.35
	15 dB	0.54	0.94	1.35
	20 dB	0.54	0.94	1.35
IPCI	5 dB	0.89	1.37	1.77
	10 dB	1.04	1.66	2.22
	15 dB	1.45	1.93	2.6
	20 dB	1.78	2.37	2.96

to feed IPCI and TFM algorithms. From Figure 2.7b,c it can clearly be seen that all SDH are displayed with the same amplitude for IPCI, whereas the effect of attenuation can be perceived for TFM on the lower SDH, and the effect of the beam transmitted amplitude on the upper SDH. To allow visualization of the whole information of the reconstructed image and to help comparison, a linear scale was used in Figure 2.7b,c.

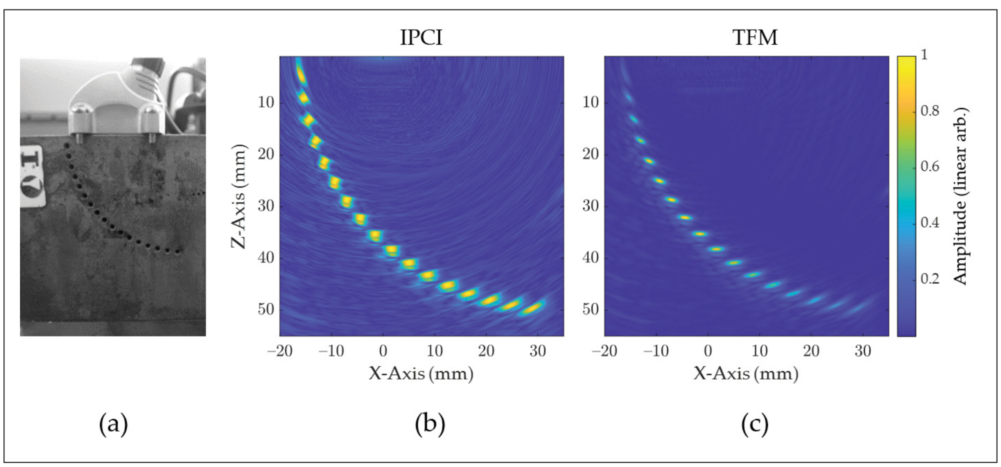

Figure 2.7 Experimental example of reconstructed defect consistency and attenuation robustness, using IPCI instead of TFM : (a) inspection setup composed of a 5 MHz (32 element) probe and an ASTM E2491 low-carbon steel test bloc ; (b) reconstructed image of the sample obtained using IPCI ; (c) reconstructed image of the sample obtained using TFM

2.3.2.3 Defect Tips Sensitivity

Another interesting property of IPCI is its sensitivity to defect tips, which allows accurate sizing of discontinuities. Indeed, it appears that the specular reflections coming from large scatterers are reduced with respect to amplitude summation, as only a few common phase terms actually contribute to the summation Equation (2.8). These few common phase terms do, however possess large amplitude, hence the strong signal from specular reflection in amplitude Equation (2.5). IPCI, then, tends to be more robust for narrow and point-like reflectors. The same simulation and processing scheme as in Section 2.2.1 was used, modeling the same probe above a 70 mm × 80 mm sample. A thin horizontal notch (0.1 mm thick and 15 mm wide) was modeled, and was located at the center of the block (Figure 2.8a). Again, the FMC was collected, and fed to IPCI and TFM algorithms. Band-limited Gaussian noise (10 dB SNR) was added to the time traces in a similar fashion to the simulation in Section 2.2.1. Images displayed in Figure 2.8b,c were scaled on a −6 dB range, so as to apply the usual 6 dB drop sizing technique for such defects (Felice & Fan, 2018). Using TFM and the aforementioned sizing method, the crack width was estimated to be 15.1 mm (Figure 2.8c). On the other hand, using IPCI and the distance between the two tips of the notch in Figure 2.8b, the crack width was estimated to be 14.7 mm.

Thus, even if in this case TFM gives a more accurate evaluation of the exact extent of the notch, IPCI, thanks to its important sensitivity to defect tips, allows accurate sizing of notch-like defects without using semi-empirical considerations that could be easily misled by a calibration process or attenuation in the material.

2.3.3 Experimental Setup

The experimental study aimed to assess and compare the performances of both methods (TOFD and IPCI) as reflectors that would be close to what can be encountered in a typical weld inspection process. Thus, experiments were conducted on a medium low-carbon steel 19 mm sample plate within which angled notches of 0.3 mm width were machined using electrical discharge machining (EDM). Notches were centered in the middle of the plate thickness and

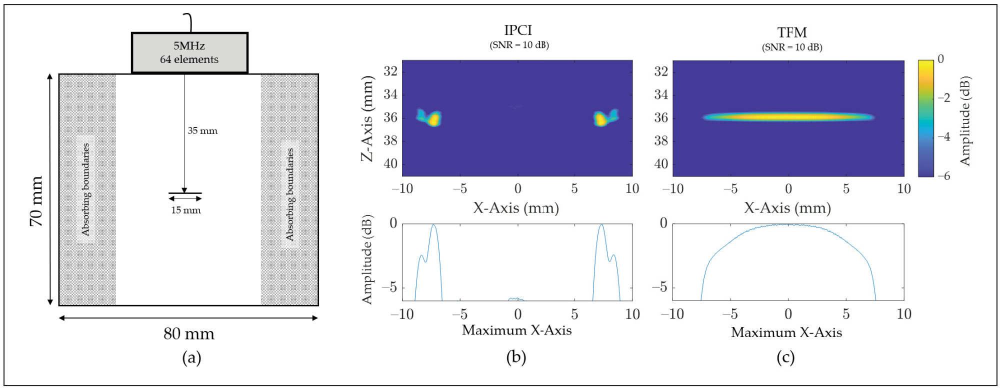

Figure 2.8 Simulated tips sensitivity analysis on a thin horizontal, using both IPCI and conventional TFM : (a) simulation setup showing the modeled notch (0.1 mm thick and 15 mm width) as long as the 5 MHz (64 element) probe above it ; (b) image obtained using IPCI and added band-limited Gaussian noise with a SNR of 10 dB, as well as its maximum intensity according to X-axis ; (c) image obtained using TFM and added band-limited Gaussian noise with a SNR of 10 dB, as well as its maximum intensity according to X-axis

four different angles were investigated : 90° (notch A), 80° (notch B), 70° (notch C), and 60° (notch D) respective to the horizontal plane (Figure 2.9). Each notch had the same vertical extent of 5 mm, and the same center position at 9.5 mm from the top or bottom of the plate.

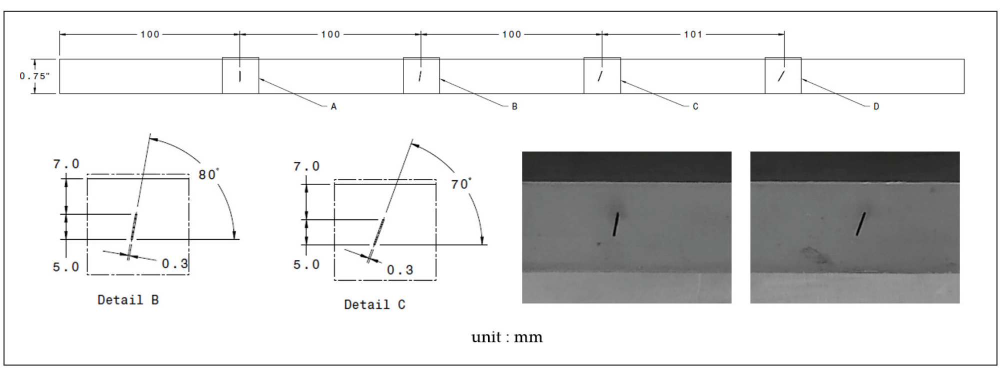

Figure 2.9 The ¾″ thick low-carbon steel sample plate. Four angled notches of 0.3 mm width were grooved using electrical discharge machining (EDM). Details (left) and pictures (right) are for a 70° (notch C) and 80° (notch B)

A Vantage 64 LE (Verasonics Inc., Kirkland, WA, USA) phased array acquisition system was used to record FMC for IPCI. TOFD measurements were performed on the commercial phased array platform, Omniscan X3 (Olympus Canada Inc., Quebec, QC, Canada). Single-element transducers used for TOFD had a center frequency of 15 MHz, an element size of 3 mm, and were excitepd by a square negative pulse. The PCS was set to 69.8 mm according to (2.2). The 60 element 1-D linear array transducer used for IPCI had a center frequency of 7.5 MHz, an elementary pitch of 1.0 mm, and an element width of 10 mm. A 3-cycle sinusoidal Hann-windowed signal was sent to each element for excitation. The full experiment parameters are listed in Table 2.2.

Tableau 2.2 Experiment parameters

Parameters	**TOFD**	**IPCI**
Probe		
Model	V564-SM	PWZ1
Central frequency	15 MHz	7.5 MHz
Elements	1	60
Elements pitch	-	1 mm
Elements width	∅ 3 mm	10 mm
Wedge		
Model	ST1-70L	SPWZ1-N55S
Angle (Refracted)	22° (70°)	36.1° (55°)
Material	Rexolite®	Rexolite®
Acquisition		
Voltage	295V	50V
Sampling frequency	100 MHz	62.5 MHz
PCS	69.8 mm	-
Sample		
Longitudinal velocity	5953 m/s	
Shear velocity	3243 m/s	

The linear array was placed on the right side of the notch, as shown in Figure 2.10a, mimicking the inspection setup that would be used to scan a weld bead and potential defects that could arise on the weld bevel. A 3D printed frame was used to hold both TOFD probes, and to adjust the PCS. Again, they were placed on each side of the notch, as would be done for an automated weld inspection (Figure 2.10b). Signals were processed in MATLAB R2019b (MathWorks, Natick, MA, USA), and sample time traces are shown in Figure 2.10a,b for each method. For convenience, signals were time-delayed to remove the excitation signal. It can be noted that the acquisition time was much longer for IPCI, due to the time of flight in the wedge, as well as the multiple reflections to consider for multi-view imaging. However, once a specific view and reconstruction area were defined, a useful time sample could be extracted, and the overall required data considerably reduced. While similar results can easily be obtained with small variations of the linear array position for IPCI, TOFD is very sensitive to PCS (Mayworm, Alvarenga & Costa-Felix, 2021), the position of the probes relative to the defect, and the coupling quality.

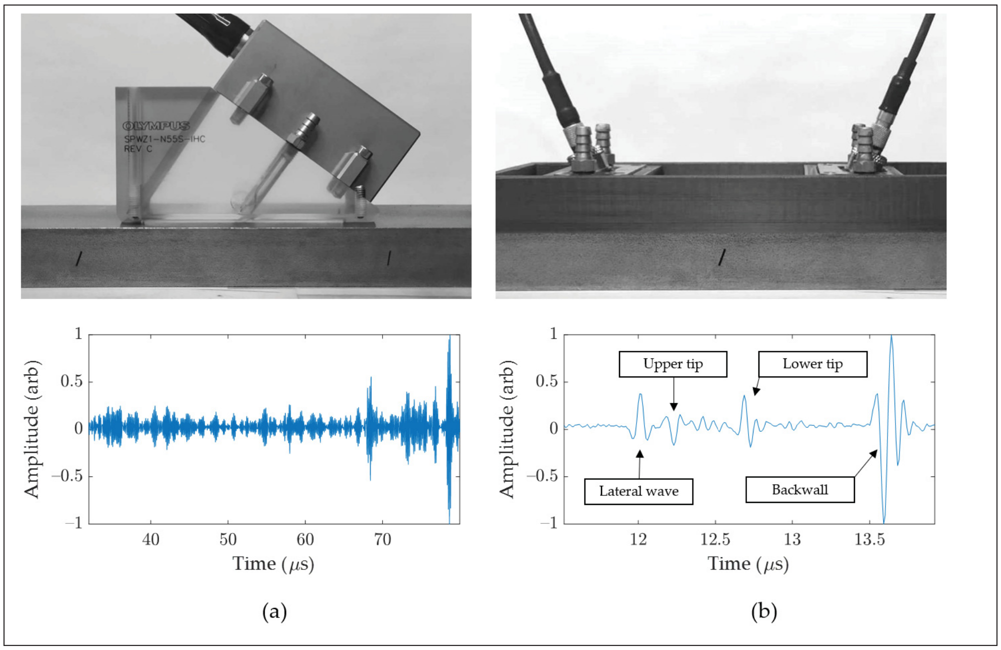

Figure 2.10 Measurement setup, and typical signal acquired signal for IPCI (a) and TOFD (b)

2.4 Results

First, results obtained for the TOFD characterization of notches A to D are detailed in Table 2.3. The measured height, as well as the defect center position, were calculated according to (2.3) and (2.4), and compared to expected values. TOFD performances in terms of localization were very satisfactory, with errors below 5%, and sizing showed a good agreement with errors, below 10%.

Tableau 2.3 Defect height, center position, and related errors using TOFD

Defect	Height (mm)	Error Height (%)	Defect Center (mm)	Error Position (%)
A	5.37	7.4	9.66	1.6
B	5.37	7.4	9.64	1.5
C	5.26	5.1	9.81	3.2
D	5.24	4.7	9.66	1.7

In order to compare the TOFD results with IPCI, the best view was first selected. Several views considering direct, half-skip, and full-skip paths were generated to help the selection, and are presented in Figure 2.11 for notch A. Additionally, conventional TFM images are also presented and used for characterization, in order to give the reader an element of comparison with a well-adopted method (Figure 2.12). It can be seen that L-based views had low sensitivity to the notches, and consisted mainly of strong artefacts, for both IPCI and TFM. All views composed only of transversal waves denoted a partial, or very clear, reconstruction of the defect. Comparing Figure 2.11 to Figure 2.12, we find fewer artefacts and a higher sensitivity to defect tips using IPCI in the former. The same observations were made for images relative to notches B, C, and D. To reduce the number of views considered in the present paper, only views T–T and TT–TT were kept for the rest of the comparison. T–T had a lower acquisition time, while allowing sizing and localization for most cases. Additionally, TT–TT was the better view for the characterization of the notches, but had a longer acquisition time.

Once T–T and TT–TT views were generated for each notch and each imaging algorithm (TFM and IPCI), the maximum intensity according to the Z-axis could be plotted to allow easy characterization of the defect in terms of position and sizing, as shown in Figure 2.13 for notch B. Both Z positions of local maxima corresponding to crack tips were measured to obtain the height and the center depth of each notch, as detailed in Tables 2.4 and 2.5. Additionally, using the TT–TT view and a −10 dB threshold, the angle of the defect could be determined using the principal axis, determined through calculation of the moment of the image (Rocha, Velho & Carvalho, 2002).

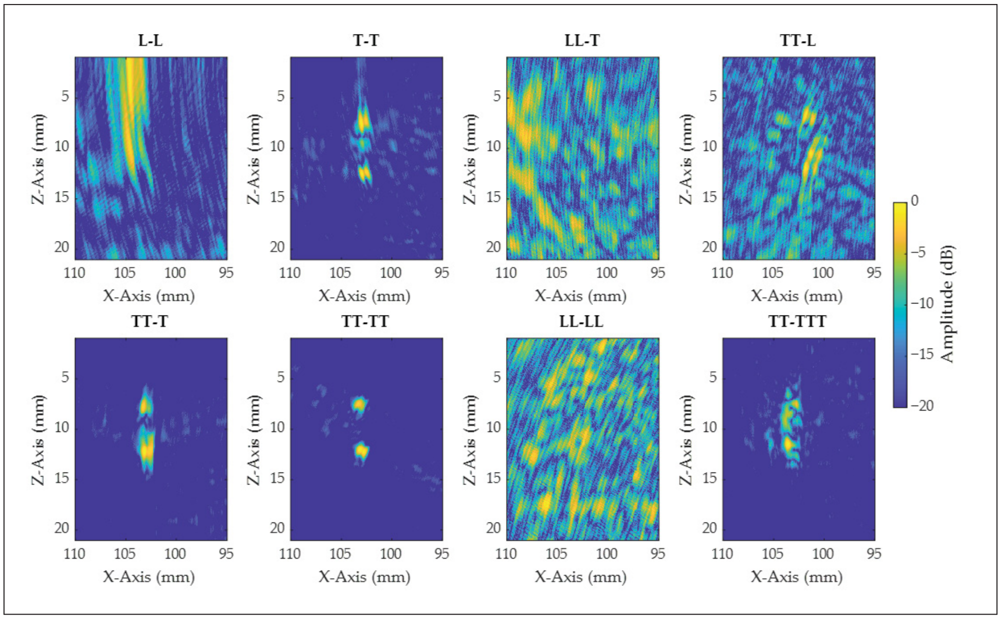

Figure 2.11 IPCI imaging algorithm applied to different views for notch A. The X-axis corresponds to the lateral distance from the wedge and the Z-axis to the vertical distance in the sample

For the results displayed in Tables 2.4 and 2.5, some values are in brackets, as they can be discarded because of the poor ability of the reconstructed image to allow the identification of defect tips. This is mainly observed for notches having an angle (Figure 2.9) below 70° for IPCI and below 80° for TFM. This can easily be explained by a greater part of the energy being reflected away from the path considered for the view. Moreover, this phenomenon was mainly observed for the T–T view, because, as the angle of the notch was increased, the energy was reflected away from the direct path to the array. This observation is accentuated for TFM as the reconstructed image is less sensitive to defect tips and is a better representation of the notch side, as shown in Figure 2.14, where this property is particularly notable for notch C.

2.5 Discussion

When comparing both results obtained for TOFD and imaging techniques, it can be seen that the positioning error (below 7%) was smaller than the sizing error (below 10%). Thus, both the T–T and TT–TT views can be considered for characterization of notch-like defects if their angle

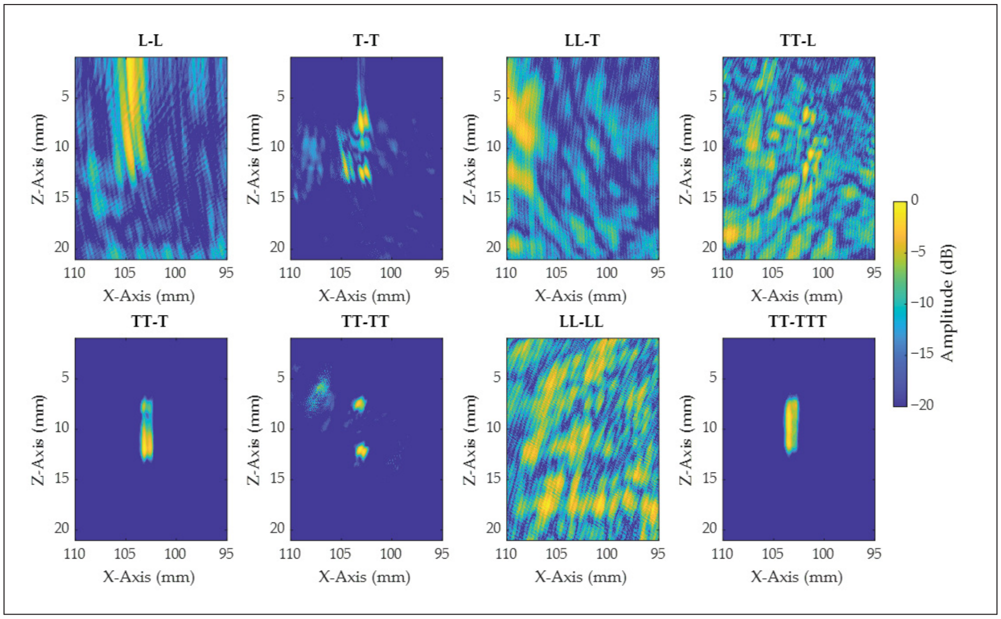

Figure 2.12 TFM algorithm applied to different views for notch A. The X-axis corresponds to the lateral distance from the wedge and the Z-axis to the vertical distance in the sample

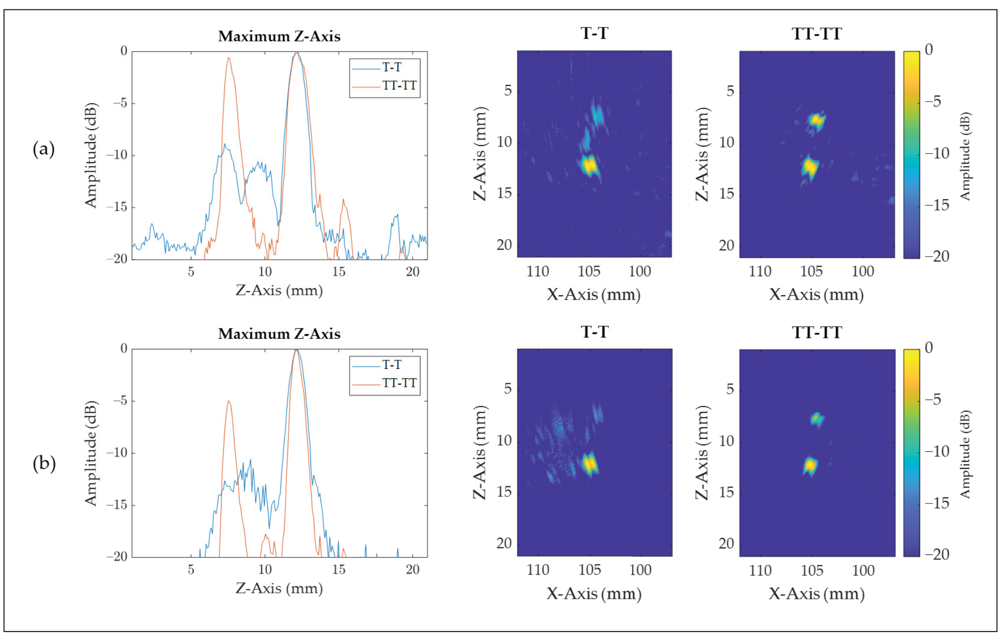

Figure 2.13 T–T and TT–TT views of notch B and their maximum intensity according to Z-axis for (a) IPCI and (b) TFM

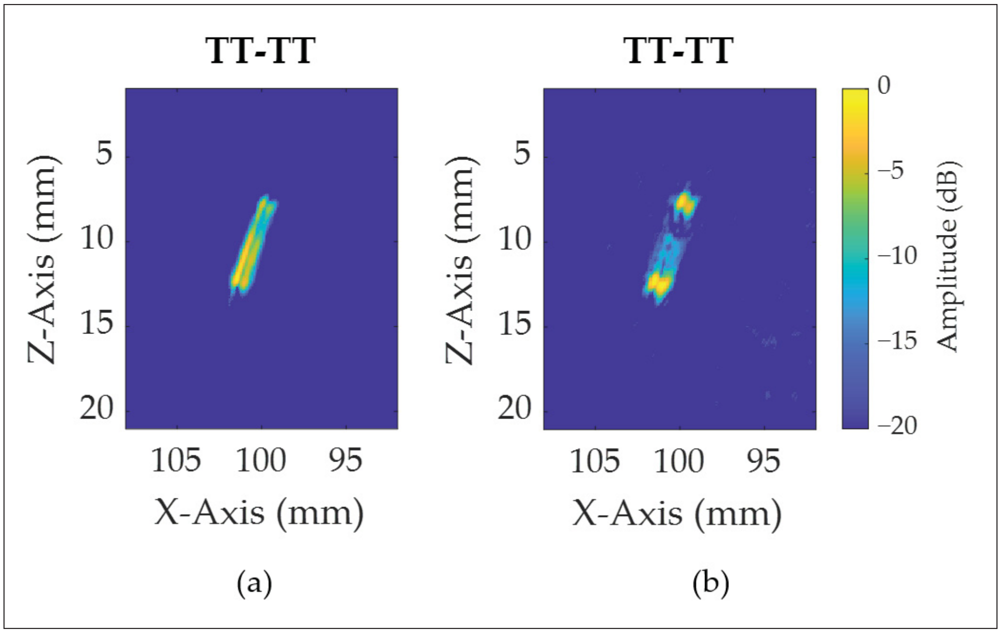

Figure 2.14 TT–TT views of notch C for (a) TFM and (b) IPCI

Tableau 2.4 Defects height, center position, and related errors for both T–T and TT–TT views using the IPCI algorithm. Angle of the defect determined using the principal axis of the TT–TT view

View	Defect	Height (mm)	Height Error	Defect Center (mm)	Position Error	Angle (°)
T–T	A (90°)	5.02	0.5%	10.04	6%	-
	B (80°)	4.77	4.7%	9.83	3%	-
	C (70°)	(2.67)	(46.5%)	9.28	2%	-
	D (60°)	(7.03)	(40.6%)	(11.30)	(19%)	-
TT–TT	A (90°)	4.52	9.5%	9.79	3%	93.6
	B (80°)	4.60	7.9%	9.83	3%	82.2
	C (70°)	4.77	4.6%	10.00	5%	72.7
	D (60°)	(3.79)	(24.2%)	9.99	5%	62.9

respective to the horizontal plane remains above 80°. For higher angles, IPCI and the TT–TT view should be preferred, as they show a better accuracy for sizing (angles up to 70°) and a stable accuracy for localization (angles up to 60°). Angle limitation was however not observed for TOFD. A comparison of the TT–TT views in both TOFD and in the imaging techniques is summarized in Figure 15 for notches A, B, and C (T–T view and notch D presented too many

Tableau 2.5 Defects height, center position, and related errors for both T–T and TT–TT views using the TFM algorithm. Angle of the defect determined using the principal axis of the TT–TT view

View	Defect	Height (mm)	Height Error	Defect Center (mm)	Position Error	Angle (°)
T–T	A (90°)	4.85	3.0%	10.04	6%	-
	B (80°)	4.60	8.0%	9.91	4.3%	-
	C (70°)	(3.51)	(29.8%)	9.53	0%	-
	D (60°)	(7.11)	(42.2%)	(11.42)	(20%)	-
TT–TT	A (90°)	4.61	7.9%	9.75	3%	95.5
	B (80°)	4.60	7.9%	9.83	3%	84.03
	C (70°)	(4.27)	(14.6%)	10.00	5%	74.2
	D (60°)	(2.01)	(59.8%)	9.45	0%	61.1

discarded values). It can be seen that the results were very similar among all presented defects and metrics, although TOFD still has the better accuracy.

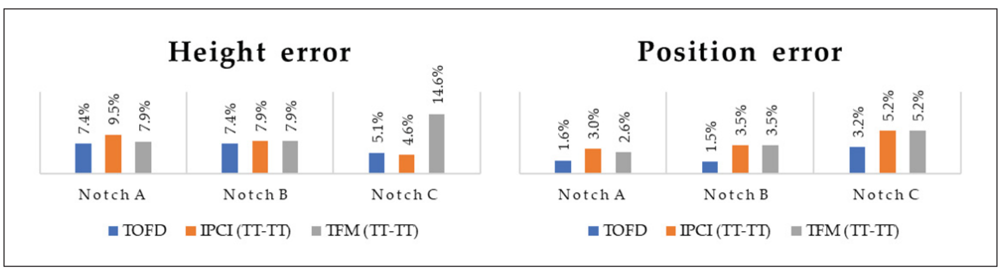

Figure 2.15 Comparison of height and position error between TOFD, IPCI TT–TT view, and TFM TT–TT view for notches A, B, and C

Beyond sizing and localization capabilities, imaging also allows a more comprehensive interpretation of inspection data, which is now fully accessible, as commercial phased array units are now capable of real-time TFM processing. As an example, while the inclination and length of defects were easily determined using TT–TT views, the orientation and length of notches, on the other hand, cannot be estimated using TOFD. While imaging techniques present some advantages over TOFD, there are also many advantages in using non-amplitude-based imaging methods. Thus, for the studied case, several benefits of IPCI over TOFD and TFM were identified :

- The inspection requires only one probe, reducing the footprint of the overall scanning setup as compared to TOFD. This allows the characterization of corner or tee joints. However, the orientation of the defect is critical for its detection, as incident energy has to be reflected back to the probe.
- Setting up the scanning is easier and less sensitive to the probe distance relative to the defect, unlike with TOFD.
- The image can be directly interpreted by the inspector and additional characteristics can be estimated, such as the defect orientation and exact location, avoiding uncertainties encountered with TOFD and the locus curve.
- Unlike with the TFM, the reconstructed image is not based on a signal amplitude, and therefore, no calibration is required for sizing, and the gain can be set to a very low value. Indeed, as can be observed in Figures 11–14, the contrast is better on IPCI images relative to TFM ones.
- Sensitivity to defect tips, and more generally to diffractive geometries, is enhanced, and allows an accurate and easier sizing of the notch compared to TFM (Figure 2.14).

2.6 Conclusions

In this paper, TOFD was compared to instantaneous phase coherence imaging (IPCI) in terms of sizing and localization of crack-like defects. IPCI multi-view imaging was explored for the first time. The use of the TT–TT view showed characterization performances similar to those of TOFD. EDM notches machined in the center of the studied sample plate demonstrated that the angle of the defect plays an important role in the relevance of the IPCI method. Indeed, both the T–T and TT–TT views were shown to be usable for angles above 80° relative to the horizontal plane, while only the TT–TT gave satisfactory results for angles between 60° and 80°. On the other hand, TOFD showed relatively stable results among different notch angles. However, in the case of welds, reflectors are mostly located along the bevel, and it is highly unlikely to encounter angles below 70°. Conventional amplitude-based TFM images were also provided, and showed a similar behavior, while being less sensitive to defect tips.

IPCI presents a competitive advantage over TOFD, as it requires a single probe, is easier to set up and interpret, and allows the estimation of additional characteristics of the defect, such as orientation. It also has clear advantages over the amplitude TFM, as it is more sensitive to defect tips, making sizing easier, and image interpretation is not based on amplitude-calibrated signals. Finally, while imaging represents an easier approach for inspection interpretation, further work has to be done in order to reduce the number of acquired signals, the data size, and the acquisition time, in order to fully compete with TOFD.

CHAPITRE 3

LIGHTWEIGHT AND AMPLITUDE-FREE ULTRASONIC IMAGING USING SINGLE-BIT DIGITIZATION AND INSTANTANEOUS PHASE COHERENCE

Baptiste Gauthier[1] , Guillaume Painchaud-April[2] , Alain Le Duff[2] , Pierre Bélanger[1]

[1] PULETS, Département de Génie Mécanique, École de Technologie Supérieure,
1100 Notre-Dame Ouest, Montréal, Québec, Canada H3C 1K3
[2] Evident Industrial, 3415 Rue Pierre-Ardouin, Québec, Québec, Canada G1P 0B3

Article publié dans «IEEE - Transactions on Ultrasonics, Ferroelectrics, and Frequency Control», Mars 2022.
https ://doi.org/10.1109/TUFFC.2022.3163621

Données, codes et matériel supplémentaire : https://pulets.ca/open-data/TUFFC-11682-2022

3.1 Abstract

In the field of ultrasonic nondestructive testing (NDT), the total focusing method (TFM) and its derivatives are now commercially available on portable devices and are getting more popular within the NDT community. However, its implementation requires the collection of a very large amount of data, with the full matrix capture (FMC) as the worst-case scenario. Analyzing all the data also requires significant processing power, and consequently, there is an interest in a) reducing the required storage capacity used by imaging algorithms such as delay and sum (DAS) imaging and b) allowing the transmission and post-processing of inspection data remotely. In this study, a different implementation of the TFM algorithm is used, based on the vector coherence factor (VCF) which is used as an image itself. This method, also generally known as phase coherence imaging, presents certain advantages, such as a better sensitivity to diffracting geometries, consistency of defect restitution among different views, and an amplitude-free behavior as only the instantaneous phase of the signal is considered. Some drawbacks of this method must also be mentioned, including the fact that it poorly reproduces planar reflectors and presents a lower signal-to-noise ratio (SNR) than amplitude-based methods. However, previous studies showed that it can be used as a reliable tool for crack-like defect sizing. Thus, a lightweight acquisition process is proposed through a single-bit digitization of the signal,

followed by a phase retrieval method based on the rising and falling edge locations, allowing to feed the phase coherence imaging algorithm. Simulated and experimental tests were first performed in the present study on several side-drilled holes (SDH) in a stainless steel block, and then extended to an experimental study on angled notches in a 19.05 mm ($\frac{3}{4}''$) thick steel sample plate through multi-view imaging. Results obtained using the array performance indicator (API) and the contrast-to-noise ratio (CNR) as quantitative evaluation parameters showed that the proposed lightweight acquisition process, which relies on binary signals, allows a reduction of data throughput of up to 47 times. This throughput reduction is achieved while still presenting very similar results to phase coherence imaging based on the instantaneous phase derived from the Hilbert transform of the full waveform. In an era of increasing wireless network speed and cloud computing, these results allow to consider interesting perspectives for the reduction of inspection hardware costs and remote post-processing.

3.2 Introduction

Since its inception in the early 70s, ultrasonic imaging has always represented a safe and accurate method for diagnosis, but one that requires costly investments. Under current trends, each professional can be equipped with their own personal device, even as the device footprints and acquisition costs have been brought down, and they are becoming ever more compatible with smart devices (smartphones, etc.) and cloud computing. In this context, two primary fields of application have emerged : medical ultrasound and ultrasonic nondestructive testing (NDT) for industrial applications. Historically, medical ultrasound has often been a step ahead of ultrasonic NDT in terms of electronics and signal processing, with the two technologies facing different realities. As an example, medical ultrasound can currently leverage the benefits of capacitive micromachined ultrasonic transducers (CMUT), allowing a probe to be powered solely by a smartphone (Joyce Y Liu, 2019). The same technology is however very limiting for ultrasonic NDT, where the acoustic impedance mismatch between the probe, the coupling material and the sample material can lead to a weak transmission of the signal as compared to the medical insonification of water-like human tissues. Hence, ultrasonic NDT generally require more powerful electronics. Consequently, ultrasonic NDT probes and driving electronics have hardly evolved over the last twenty years, with related efforts focused on fitting acquisition units with more computing power. Indeed, it took almost ten years between the first implementation of the total focusing method (TFM) and its commercial availability in a portable instrument (Holmes *et al.*, 2005).

Today, acquisition units are able to compute complex paths and images very rapidly through CPU, GPU or FPGA implementations of post-processing algorithms. There is still an interest in reducing the size of the generated data, particularly given the increasing popularity of heavy acquisition patterns such as the full matrix capture (FMC) and the half matrix capture (HMC). The goal is, on the one hand, to reduce the storage capacity required to save and archive inspection records, and on the other hand, to allow the post-processing and transmission of inspection data remotely. The scope of this study does not extend to working on the storage of images, but rather on the relevant amount of information necessary for the production of such images, which can be achieved through various methods, either directly, during inspection, or later, during analysis. Of course, any impact on the image quality, the probability of detection or the ease of interpretation should be minimal when considering such an approach.

The first ultrasonic imaging data reduction approach reported in the literature consists of the data compression of raw time traces. This has been studied from various angles over the years. The use of compression algorithms based on domain transformation has been extensively investigated, using discrete wavelet transform (DWT), discrete cosine transform (DCT), Walsh-Hadamard transform (WHT) and similar methods (Cardoso & Saniie, 2004; Sharov, Orlov & Persiantsev, 2006; Zhang, Chen, Que & Xing, 2008; Govindan & Saniie, 2015). As well, parameter estimation or extraction methods have also been examined. These include continuous wavelet transform (CWT) and its modified version (MCWT) (Cardoso & Saniie, 2005), matching pursuit decomposition (MP) (Ruiz-Reyes, Vera-Candeas, Curpián-Alonso, Mata-Campos & Cuevas-Martínez, 2005; Nabil, Toufik & Morad, 2015), chirplet signal decomposition (CSD) (Lu, Demirli, Cardoso & Saniie, 2006) and maximum likelihood estimation (MLE) (Demirli & Saniic, 2004). Other methods that have been explored include linear predictive coding (LPC) (Pesavento, Burow & Ermert, 1997), the exploitation of data redundancy and Glomb coding (Mansour & Ali, 2010), waveform modeling using a sum of Gaussian (SOG) in combination with space-alternating generalized expectation maximization (SAGE), or a sum of exponential (SOE) in combination with the matrix pencil (MPe) algorithm. More recently, angle-based adjacent basis grouping (ABBG) (Fan, Aeron, Pedrycz & Valero, 2017) and the sum of binary cluster (BL) (Kim *et al.*, 2018) have shown promising results for fast screening and real-time imaging applications. All these methods share the same principle, which is the ability to reconstruct with minimal or without loss of the original signal while achieving good compression ratios (between 30% and 97%). Additionally, the methods can be helpful for velocity determination, target identification and object classification. Finally, the signal-to-noise ratio (SNR) is usually improved through the filtering properties of the aforementioned algorithms.

Another approach that has been used for data reduction consists in evaluating the interest of acquiring all the fluctuations of the ultrasonic signal, i.e., the AScan signal, when the targeted application is performing imaging. For example, in an interesting proposition presented in (Soto-Cajiga, Pedraza-Ortega, Rubio-Gonzalez, Bandala-Sanchez & Romero-Troncoso, 2012), only the time of occurrence and amplitude of maximum echoes of the measured signal are recorded in order to determine the remaining thickness of a pipe. The question here is if a similar approach could be adopted for ultrasonic imaging : recording only the information needed to achieve a good quality reconstruction. Of note, proceeding with this analogically would reduce the cost of the analog-to-digital conversion. (Camacho *et al.*, 2009) introduced the phase coherence factor (PCF), sign coherence factor (SCF) and later vector coherence factor (VCF) (Cruza *et al.*, 2017) concepts as means of improving the dynamic range of a synthetic aperture focusing technique. Usually, the method applying these concepts is used to weigh an existing TFM image, but it can also be used on its own as a more contrasted representation of the inspected sample relative to the coherence of the instantaneous phase or sign of reflector echoes (Camacho *et al.*, 2018; Gauthier *et al.*, 2021; Zhang *et al.*, 2020). The use of phase- or sign-based imaging methods comes with several advantages. First, when relying solely on the phase or sign of the signal, the reconstruction is achieved without considering the amplitude, which therefore removes the need for an amplitude calibration process. Weak reflectors that would normally be missed or mixed up with artefacts due to attenuation on resulting image are thus enhanced provided the measured scattered signal by the reflector is still above the noise floor. Then, the acquisition process during which the phase or sign of the signal is collected becomes much simpler and lighter in terms of data throughput. Finally, it allows the use of a simplified and faster electronic architecture, as used by (Isla & Cegla, 2019), employing comparators for signal acquisition. There are many applications based on this approach ranging from its implementation in a light and portable device to the use of high-speed wireless networks for remote post-processing, or even the development of a very dense array setup.

In the preceding parts, two types of approaches for data reduction were identified : compression after acquisition, as illustrated in Figure 3.1.a, and selective acquisition (such as single-bit digitization), as illustrated in Figure 3.1.b. We investigated the *lightest* way of producing realistically usable ultrasonic images as a means of providing a lightweight and low-cost solution while maintaining the benefits of coherence imaging. A selective acquisition scheme was used, relying on single-bit digitization, followed by a phase retrieval method based on rising and falling edge locations. The retrieved phase is then used to calculate the vector coherence factor (VCF) which in this case is used as an image itself. The performance of the proposed method, in terms of data reduction and imaging quality, as compared to conventional TFM and VCF, was assessed through simulations and experiments on a stainless-steel block comprising side-drilled holes (SDH) and on a low-carbon steel plate. The rest of the paper is divided as follows : Section 2 presents the materials and methods, including a description of the binary quantization procedure, the instantaneous phase retrieval method, the VCF image reconstruction, the proposed indicators used for comparison, and the simulation and experimental setup. Simulations and experimental results are presented in Section 3. A discussion is presented in Section 4, followed by conclusions in Section 5.

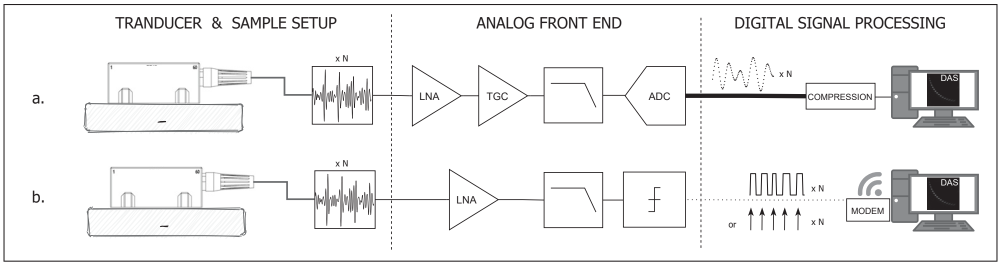

Figure 3.1 Different approaches for ultrasonic data reduction. On the one hand (a.), a compression after conventional acquisition is considered : N analog signals acquired from elements of a linear array are processed using a Low-Noise Amplifier (LNA), Time Gain Compensation (TGC), low-pass filter and an Analog to Digital Converter (ADC). Finally, a compression algorithm is applied on the sampled date before storage on the processing unit. On the other hand (b.), a selective single-bit digitization process is considered : N analog signals acquired from elements of a linear array are processed using a LNA and low-pass filter and then binarized by a comparator (keeping the full binary version of the signal or only rising and/or falling edges of this later). This allows an easier wireless transmission of the data to the processing unit

3.3 Materials and methods

3.3.1 Vector Coherence Factor (VCF) and Total Focusing Method (TFM)

Vector Coherence Factor (VCF), first introduced in (Martínez-Graullera *et al.*, 2012) and later named in (Cruza *et al.*, 2017), is used in this study as an image itself along with its multi-view implementation (Zhang *et al.*, 2010; Budyn *et al.*, 2019). The method was extensively detailed in (Gauthier *et al.*, 2021) where it was referred as Instantaneous Phase Coherence Imaging (IPCI), and is briefly recalled in the case where a Full Matrix Capture (FMC) is recorded using a 1D linear array of N_e elements.

Consider a region of interest (ROI) in the test piece, discretized by a pixel grid in which each pixel is located by its position (x, z). The intensity of each pixel in the ROI after applying a conventional delay-and-sum (DAS) reconstruction algorithm based on signal amplitude, such as

TFM, is given by :

$$
\begin{aligned}
I_{\mathrm{TFM}}(x,z) &= \left| \sum_{k=1}^{N_e} \sum_{l=1}^{N_e} \tilde{y}_{kl}(\tau_{kl}(x,z)) \right| \\
&= \left| \sum_{k=1}^{N_e} \sum_{l=1}^{N_e} |\tilde{y}_{kl}(\tau_{kl}(x,z))| \mathrm{e}^{i\phi_{kl}(\tau_{kl}(x,z))} \right|,
\end{aligned} \tag{3.1}
$$

where $\tilde{y}_{kl}(t)$ denotes the analytic signal of the amplitude received signal $y_{kl}(t)$ at a given time $\tau_{kl}(x,z)$, corresponding to the total time of flight between the emitting element k, a pixel, and the receiving element l.

While still relying on a DAS pattern, the calculation of VCF differs slightly by discarding the amplitude term and using the in-phase and quadrature components of the signal, and is given by :

$$
I_{\mathrm{VCF}}(x,z) = \left(\left(\sum_{k=1}^{N_e} \sum_{l=1}^{N_e} \sin\left(\phi_{kl}(\tau_{kl}(x,z))\right) \right)^2 + \left(\sum_{k=1}^{N_e} \sum_{l=1}^{N_e} \cos\left(\phi_{kl}(\tau_{kl}(x,z))\right) \right)^2 \right)^m \tag{3.2}
$$

with ϕ_{kl} being the instantaneous phase of the signal obtained using (3.8), (3.10) or the Hilbert transform (this latter being referred as ϕ_H). Exponent m is a modulation factor used to tweak the sensitivity to side lobes (Lyu *et al.*, 2021), and is generally set to $m = \frac{1}{2}$, which corresponds to the $\mathcal{L}_2$ norm. If $m = \frac{1}{2}$, (4.2) can be rewritten :

$$
I_{\mathrm{VCF}}(x,z) = \left| \sum_{k=1}^{N_e} \sum_{l=1}^{N_e} \mathrm{e}^{i\phi_{kl}(\tau_{kl}(x,z))} \right|. \tag{3.3}
$$

3.3.2 Single-bit quantization and SCF

The first stage of the proposed method aims to quantize the analogue signal between two different levels, typically 0 and 1. Considering a temporal AScan signal $y(t)$, the binarized version of this

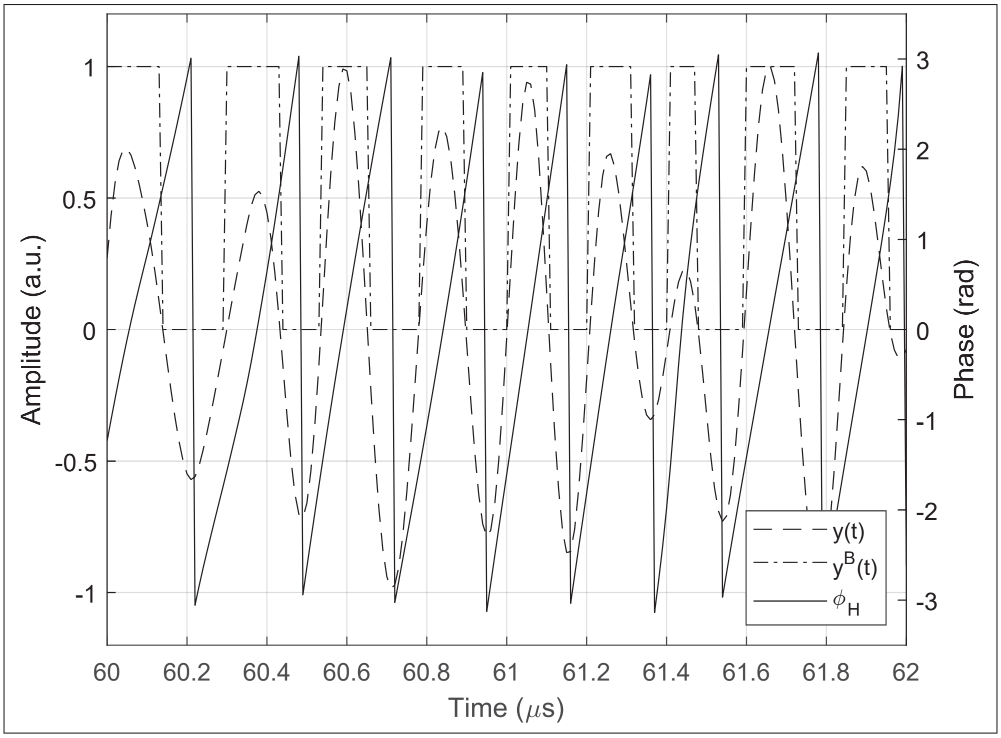

Figure 3.2 Example of an ultrasonic raw signal (dashed line), binarized signal (dash-dot line) and instantaneous phase of the signal using the Hilbert transform (ϕ_H - solid line)

signal $y^B(t)$ is given by :

$$y^B(t) = \begin{cases} 1, & \text{if } y(t) \geq 0 \\ 0, & \text{if } y(t) < 0 \end{cases}. \tag{3.4}$$

Practically, this single-bit digitization can be achieved through analogue components such as a comparator. For this study, the binarization is performed on a previously digitized FMC. Using a 1D linear array of N_e elements, binarized signals for each combination of emitting element k and receiving element l can be obtained by :

$$y^B_{kl}(t) = \frac{1}{2} \cdot \{1 + \text{sign}[y_{kl}(t)]\} \quad \forall \{k, l\} \in [1, N_e]. \tag{3.5}$$

An example of a previously digitized signal and its binarized version using (3.5) is shown in Figure 3.2.

It should be noted that such binarized signals are generally used to compute the SCF, introduced by (Camacho *et al.*, 2009) and extended to FMC acquisitions in (Zhang *et al.*, 2013a), which is defined as follows :

$$I_{SCF}(x,z) = 1 - \sqrt{1 - \left[\frac{1}{N_e^2}\sum_{k=1}^{N_e}\sum_{l=1}^{N_e} y^B(\tau_{k,l}(x,z))\right]^2}. \tag{3.6}$$

3.3.3 Instantaneous phase retrieval

As the intended imaging algorithm used in this paper is based on the signal instantaneous phase, it has to be estimated using the previously binarized signal. In this section, two retrieval methods are presented based on the observation that, as illustrated in Figure 3.2, the instantaneous phase shows a roughly segmented linear behavior between $[-\pi, 0]$ and $[0, +\pi]$ for each half period of the signal. The first retrieval method presented below has the advantage of relying only on the rising edge position of the binarized signal while the second one relies on rising and falling edge positions. The underlying interest of proposing two methods is related to the resulting data throughput reduction.

3.3.3.1 Two-step retrieval

For this first retrieval method, it is assumed that the phase varies linearly between $[-\pi, \pi]$ for each period of the signal. From the observed variation of the instantaneous phase (Figure 3.2), the rising edge positions of the binarized signal are used to define four equal length time periods, as illustrated in Figure 3.3b. These time periods are then used to define the starting and ending time increments for the linear regression between $-\pi$ and π.

First, the derivative of the binarized signal, $d_1(t)$, is computed to obtain the rising edge time positions, and gives :

$$d_1(t) = \sum_{n=1}^{N_{re}} \delta(t - t_n) \tag{3.7}$$

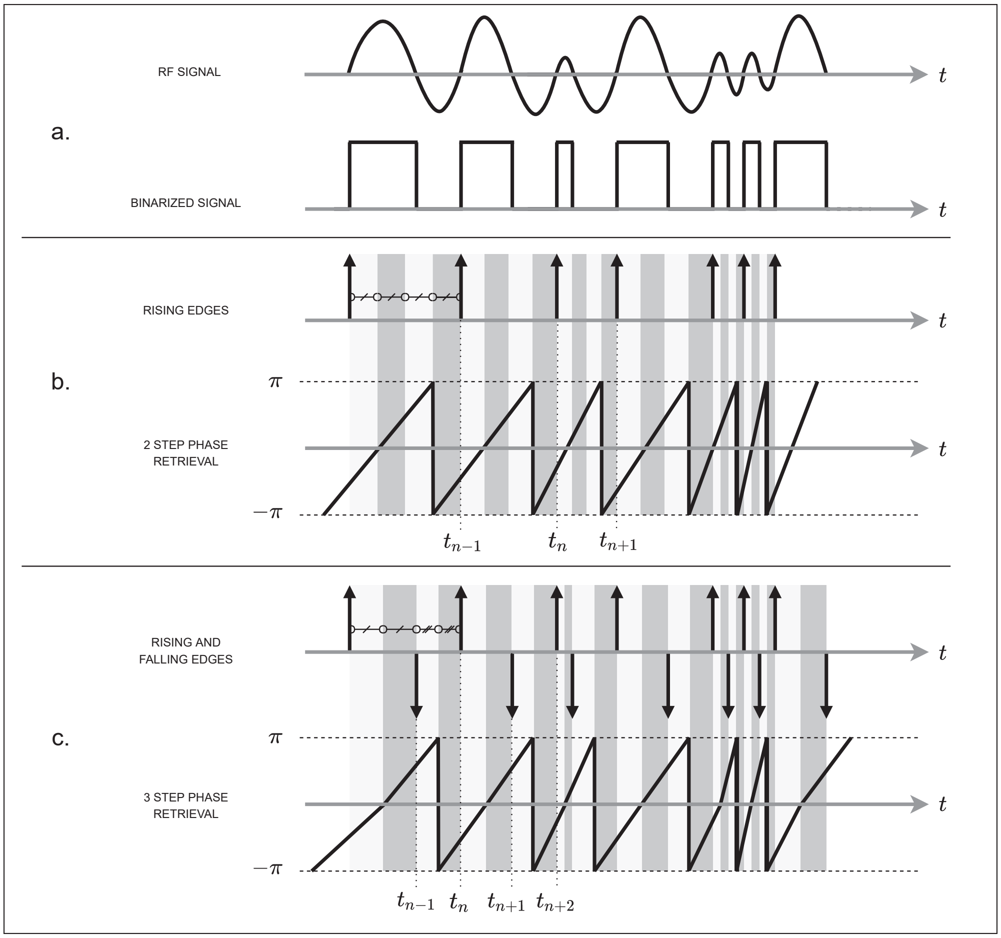

Figure 3.3 Instantaneous phase reconstruction principle based on a. the binarized signal, using b. a 2-step retrieval or c. a 3-step retrieval method

where N_{re} is the number of rising edges, δ the Dirac distribution and t_n the time increment corresponding to the rising edge. Then, the phase retrieval is obtained through :

$$\phi_1(t) = 2\pi \left(\frac{t - \frac{1}{4}(t_{n-1} + 3t_n)}{\frac{1}{4}(3t_{n+1} - 2t_n - t_{n-1})} \right) - \pi \mod 2\pi, \tag{3.8}$$

where t_{n-1}, t_n and t_{n+1} are the time increments corresponding to three successive rising edges, respectively (Figure 3.3b). A detailed demonstration of this formula is presented in the supplementary downloadable material. A comparison between the instantaneous phase obtained using the Hilbert transform, ϕ_H, and the retrieved phase using (3.8), ϕ_1, is presented and can be appreciated qualitatively in Figure 3.4 but is also compared quantitatively through a difference plot in Figure 3.5a. It can be observed that this first method leads to a sufficient approximation of the real phase with major divergence occurring for values of phase close to $\pm\pi$ that are slightly offset.

3.3.3.2 Three-step retrieval

For this second retrieval method, it is assumed that the phase varies linearly between $[-\pi, 0]$ and $[0, +\pi]$ for each period of the signal. Again, and from the observed variation of the instantaneous phase, the rising and falling edge positions of the binarized signal are used to define two equal length time periods, as illustrated in Figure 3.3c. These time periods are then used to define the starting and ending time increments for the linear regression between $[-\pi, 0]$ and $[0, +\pi]$.

First, the derivative of the binarized signal, $d_2(t)$, is computed to obtain the rising and falling edge time positions, and gives :

$$d_2(t) = \sum_{n=1}^{N_{rfe}} [\delta(t - t_n) - \delta(t - t_{n+1})], \tag{3.9}$$

where N_{rfe} is the number of rising and falling edges, δ the Dirac distribution, t_n and t_{n+1} the time increment corresponding to the rising edge and falling edge, respectively. Then, the phase retrieval is obtained through :

$$\phi_2(t) = \begin{cases} \phi_a(t) & \text{for } \frac{t_n + t_{n-1}}{2} < t < \frac{t_{n+1} + t_n}{2}, \\ \phi_b(t) & \text{for } \frac{t_{n+1} + t_n}{2} < t < \frac{t_{n+2} + t_{n+1}}{2} \end{cases} \tag{3.10}$$

where

$$\phi_a(t) = \pi \left(\frac{2t - t_n - t_{n-1}}{t_{n+1} - t_{n-1}} \right) - \pi \mod 2\pi \tag{3.11}$$

and

$$\phi_b(t) = \pi \left(\frac{2t - t_n - t_{n+1}}{t_{n+2} - t_n} \right) \mod 2\pi \tag{3.12}$$

where t_{n-1}, t_n and t_{n+1},t_{n+2} are two successive couples of time increments corresponding to a falling edge and a rising edge, respectively (Figure 3.3c). A detailed demonstration of this formula is also presented in the supplementary downloadable material. A comparison between ϕ_H and the retrieved phase using (3.10), ϕ_2, is presented and can be appreciated qualitatively in Figure 3.4 but is also compared quantitatively through a difference plot in Figure 3.5b. . It can be observed that this latter method leads to a sharper reconstruction of the true phase and represents a significant improvement with quite the same offset for values of phase close to $\pm\pi$.

3.3.3.3 Data throughput estimation

As mentioned earlier, the main interest of using single-bit quantization is the induced reduction in terms of generated data transiting from the analog front end to the digital processing end (Figure 3.1). In this section, this gain is evaluated through the required storage for an FMC data collection and a typical NDT hardware configuration. A 5 MHz, 64-element linear probe and an acquisition device sampling at 100 MHz are considered. Additionally, for the full waveform digitization case, an analog-to-digital converter (ADC) having a resolution, R_b, of 12 bits is considered. Finally, the recorded length, N_s, is assumed to be 10 k-samples – corresponding to a 100 μs acquisition time - which is long enough to capture the different reflections using a wedge in the sample piece for a weld inspection scenario.

Four estimations are presented in Table 3.1, and is used for SCF imaging. Rising and falling edge positions correspond to the storage of the number of time increments between rising and falling edges, coded in P bits and considering N_p sample points for a period of the signal at its center frequency. P can be estimated by comparing N_p to its closest power of 2 (upper limit). In our case, $N_p = 20$ for a 5 MHz probe and a 100 MHz sampling frequency which lead $2^4 \leq N_p \leq 2^5$ and hence $P = 5$. For each method, the formula used to estimate the data size generated by the example case is presented. Thus, for the presented example, data reduction can reach up to 47 times the original size.

Tableau 3.1 Estimation of the data throughput generated by different data collection methods. An example and the related compression ratios are presented considering a 5 MHz, 64-element linear probe and an acquisition device sampling at 100 MHz

Method	**Formula**	**Example**	**Compression ratio**
Full waveform digitization	$N_s R_b N_e^2$	61.4 MB	1 :1
Single-bit quantization	$N_s N_e^2$	5.1 MB	12 :1
Rising and falling edges positions	$2PN_p N_e^2$	2.6 MB	24 :1
Rising edges positions	$PN_p N_e^2$	1.3 MB	47 :1
$N_s = 10000; R_b = 12; N_e = 64; P = 5$ and $N_p = 20$			

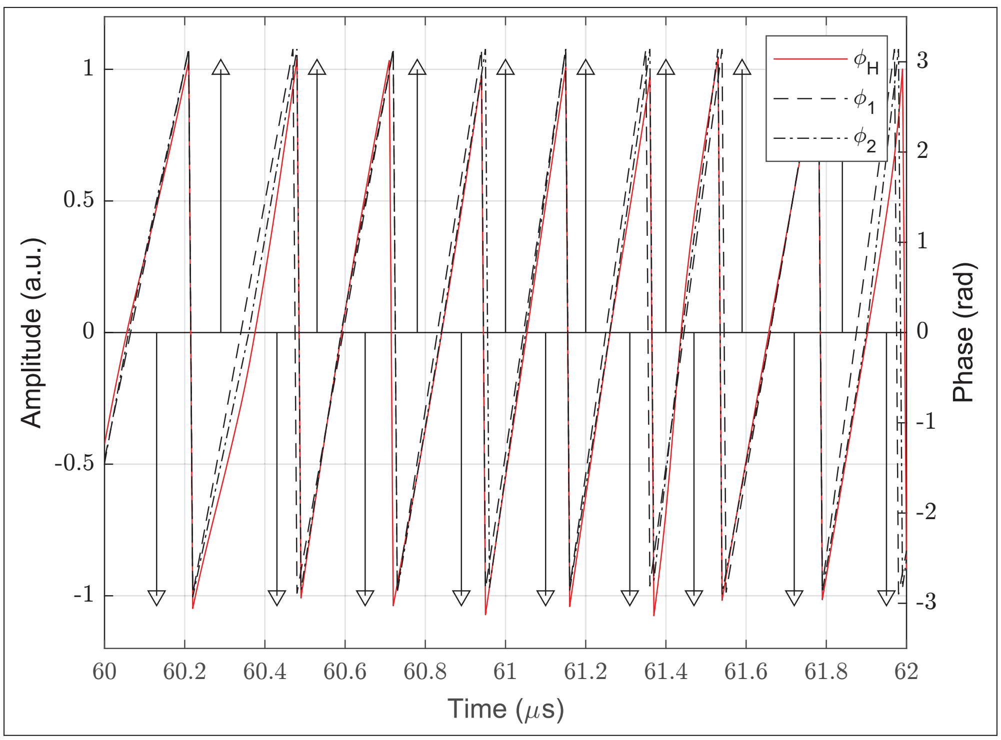

Figure 3.4 Comparison between the instantaneous phase of an ultrasonic signal obtained using Hilbert transform (ϕ_H - solid line), the 2-step retrieval method (ϕ_1 - dashed line), and the 3-step retrieval method (ϕ_2 - dash-dot line). Rising and falling edges are identified by upward-pointing and downward-pointing triangles respectively

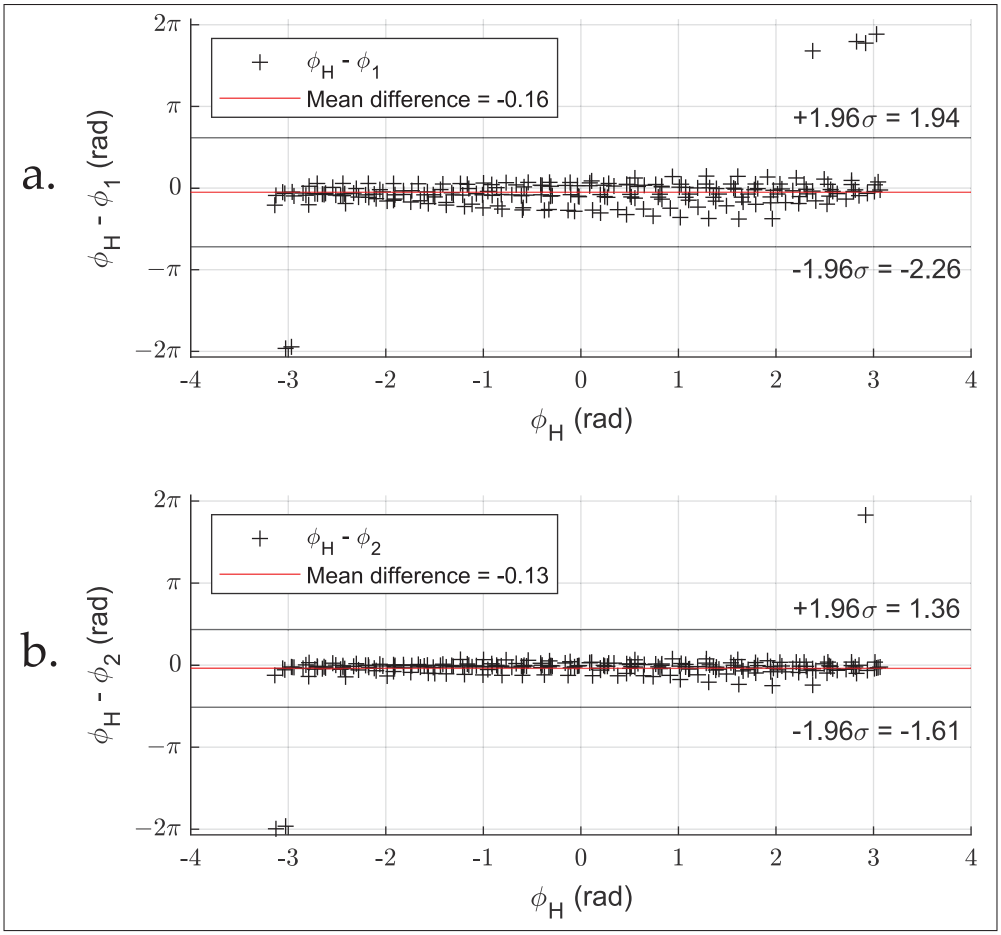

Figure 3.5 Difference plot showing the differences between a. the retrieved phase ϕ_1 and ϕ_H and b. the retrieved phase ϕ_2 and ϕ_H. For each difference plot, the mean difference is displayed (red solid line) as well as ± 1.96 standard deviation of the difference, σ, which corresponds to 95% limits of agreement (black solid line)

3.3.4 Quantitative evaluation of the imaging performance

Assessing the performance of an imaging algorithm or method is not an easy feat as the human perception and interpretation are necessarily subjective. However, because a study involving a sample of trained inspectors evaluating such imaging methods would be beyond the scope of this paper, commonly adopted indicators are used to quantitatively evaluate the results presented.

3.3.4.1 Array Performance Indicator (API)

The API was introduced by (Holmes *et al.*, 2005) and is a parameter characterizing the restitution, by a given imaging algorithm, of a point-like scatterer. This is defined as follows :

$$API = \frac{A_{-6dB}}{\lambda^2} \tag{3.13}$$

where λ is the wavelength at the probe center frequency and in the inspected material and A is the area where the point spread function is greater than a −6 dB threshold with respect to the maximum. Being adimensional, this parameter allows to evaluate the sharpness of the reconstructed image for a given defect, where a smaller API will be related to a sharper restitution of the latter.

3.3.4.2 Contrast-to-Noise Ratio (CNR)

When the defect does not behave like a point-like scatterer, other indicators related to the general perception of the rendered defect shape in relation to the rest of the image should be considered. In this study, the CNR is used to achieve this goal, and is defined as follows (Gomi & Nakajima, 2012; Welvaert & Rosseel, 2013) :

$$CNR = \frac{|\mu_{df} - \mu_{bg}|}{\sigma_{bg}} \tag{3.14}$$

where μ_{df} is the mean pixel value in a subset of the ROI around the defect location and μ_{bg} and σ_{bg} are the mean and standard deviation of pixel values in a subset of the ROI outside defect location, respectively. Both subsets are of equal size.

3.3.5 Simulated and experimental setup

Two configurations were considered to evaluate the performance of VCF using the phase retrieved from a single-bit digitized signal. These configurations aimed to be as generic as possible to allow conclusions to be applied to a wide variety of defects. The first configuration presents simulated and experimental SDH in a stainless-steel block located at different depths, while the second one presents experimental notches with different angles in a low-carbon steel plate.

3.3.5.1 SDH Configuration

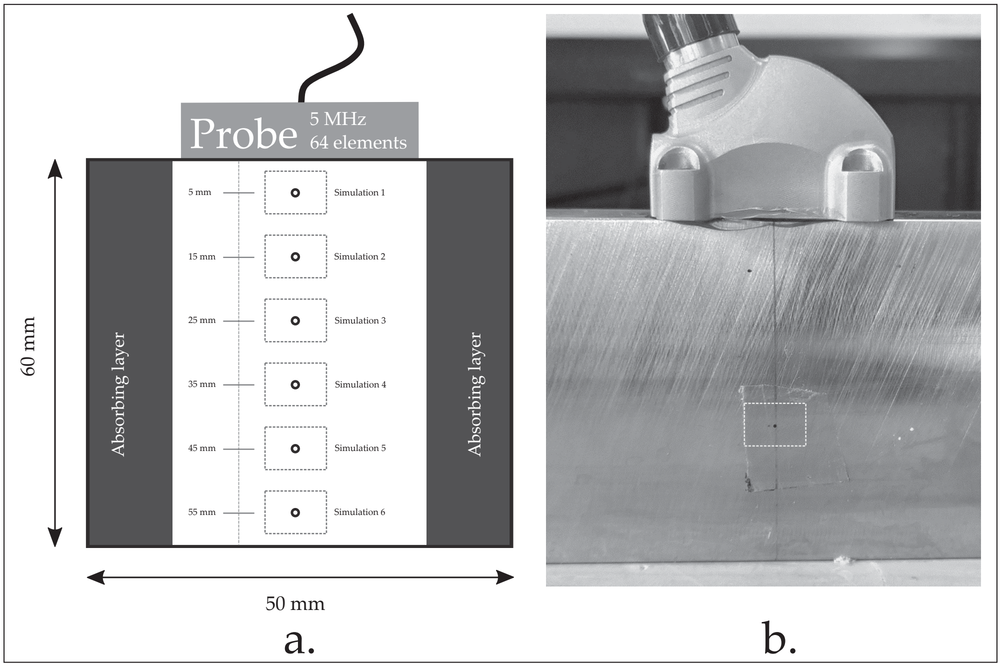

Figure 3.6 Configuration for a. simulated SDH and b. experimental measurements

A simple case was first considered both through simulations and experiments. The Pogo FEA solver was used for simulations (Huthwaite, 2014). A 2D 60 mm × 50 mm stainless steel block with SDH having a diameter of 0.5 mm at different depths (simulation 1 : 5 mm, simulation 2 : 15 mm, simulation 3 : 25 mm, simulation 4 : 35 mm, simulation 5 : 45 mm and simulation 6 : 55 mm) was modeled, as illustrated in Figure 3.6a. A 1D 5 MHz center frequency probe having 64 elements and a pitch of 0.5 mm located on the top of the block was simulated with a 3-cycle Hann windowed toneburst applied to the top surface nodes of the mesh. Absorbing boundaries (Pettit, Walker, Cawley & Lowe, 2014) were added to the block sides to avoid unwanted reflections. Finally, 64 simulations were run in order to model a single FMC acquisition scenario and an additive white gaussian noise with 15 dB SNR was added on each time trace for greater realism and to prevent the generation of unwanted artefacts, as discussed in (Gauthier *et al.*, 2021).

Experimentally, a stainless-steel block (V_L = 5700 m/s) comprising 6 similar successive SDH was used to conduct the exact same acquisition as the simulated one (Figure 3.6b). A 5L64-A32 linear 5 MHz, 64-element probe (Olympus Inc., State College, PA, USA) in combination with a Vantage 64 LE (Verasonics Inc., Kirkland, WA, USA) ultrasonic acquisition system was used to perform an FMC over each SDH.

3.3.5.2 Angled notch configuration

A more complex scenario was then considered experimentally using two low-carbon steel 19.05 mm ($\frac{3}{4}''$) thick plates within which 0.3 mm angled notches were machined by electrical discharge machining (EDM), as illustrated in Figure 3.7. The goal here was to simulate cracks and usual defect that could be found on the bevel of a weld. Inspections of weld bevels are typically performed using a wedge to allow insonification with shear waves. The first plate comprised four notches centered in its middle, with different angles with respect to the horizontal : 90° (Notch C1), 80° (Notch C2), 70° (Notch C3) and 60° (Notch C4). The second one comprised four surface breaking notches located near the bottom of the plate with, again, different angles with respect to the horizontal : 90° (Notch B1), 80° (Notch B2), 70° (Notch B3) and 60° (Notch B4). A 7.5L60 PWZ1, linear, 7.5 MHz, 60-element probe (Olympus Inc., State College, PA, USA) mounted on top of an SPWZ1-N55S rexolite wedge (Olympus Canada Inc., Quebec, QC, Canada) was used in combination with a Vantage 64 LE (Verasonics Inc., Kirkland, WA, USA) system to perform an FMC for each notch.

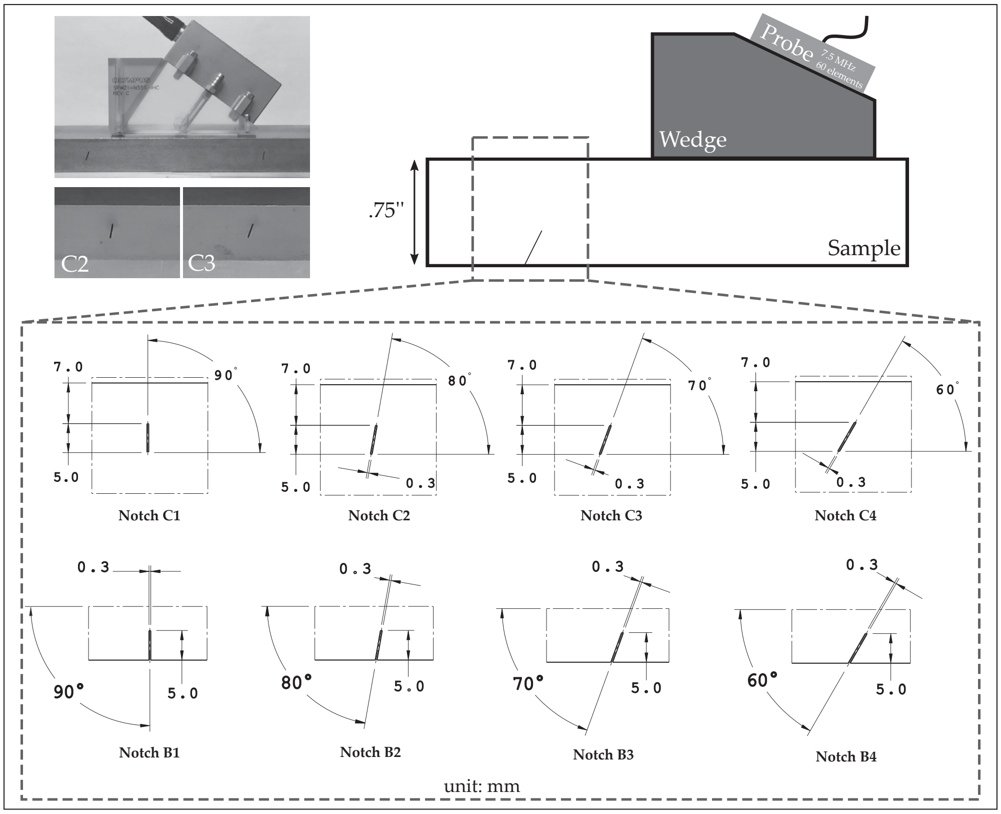

Figure 3.7 Experimental configuration for eight different angled notches (0.3 mm wide) machined using Electrical Discharge Machining (EDM) in low-carbon steel 19.05 mm ($\frac{3}{4}''$) thick plates. Schematic for the 4 notches located at the center of the plate (respectively notch C1, C2, C3 and C4) and the 4 surface breaking notches (respectively notch B1, B2, B3 and B4) are provided. A linear ultrasonic array mounted on a wedge is used. Pictures of notches C2 and C3 as well as of the experimental configuration are provided

3.4 Results

3.4.1 SDH configuration results

Following the acquisition of the FMC from the simulations and experiments on SDH, the VCF reconstruction was applied using the instantaneous phase obtained using ϕ_1 (3.8) and ϕ_2 (3.10) from the binarized signals (3.5). Additionally, VCF was also applied to phase ϕ_H, and the TFM and SCF (also presented as an image itself) were also calculated for reference. The resulting images are presented in Figure 3.8 for simulated data and in Figure 3.9 for experimental data.

For each individual image, a ROI of 10 mm × 10 mm was considered centered on the SDH location, which is denoted by a red circle.

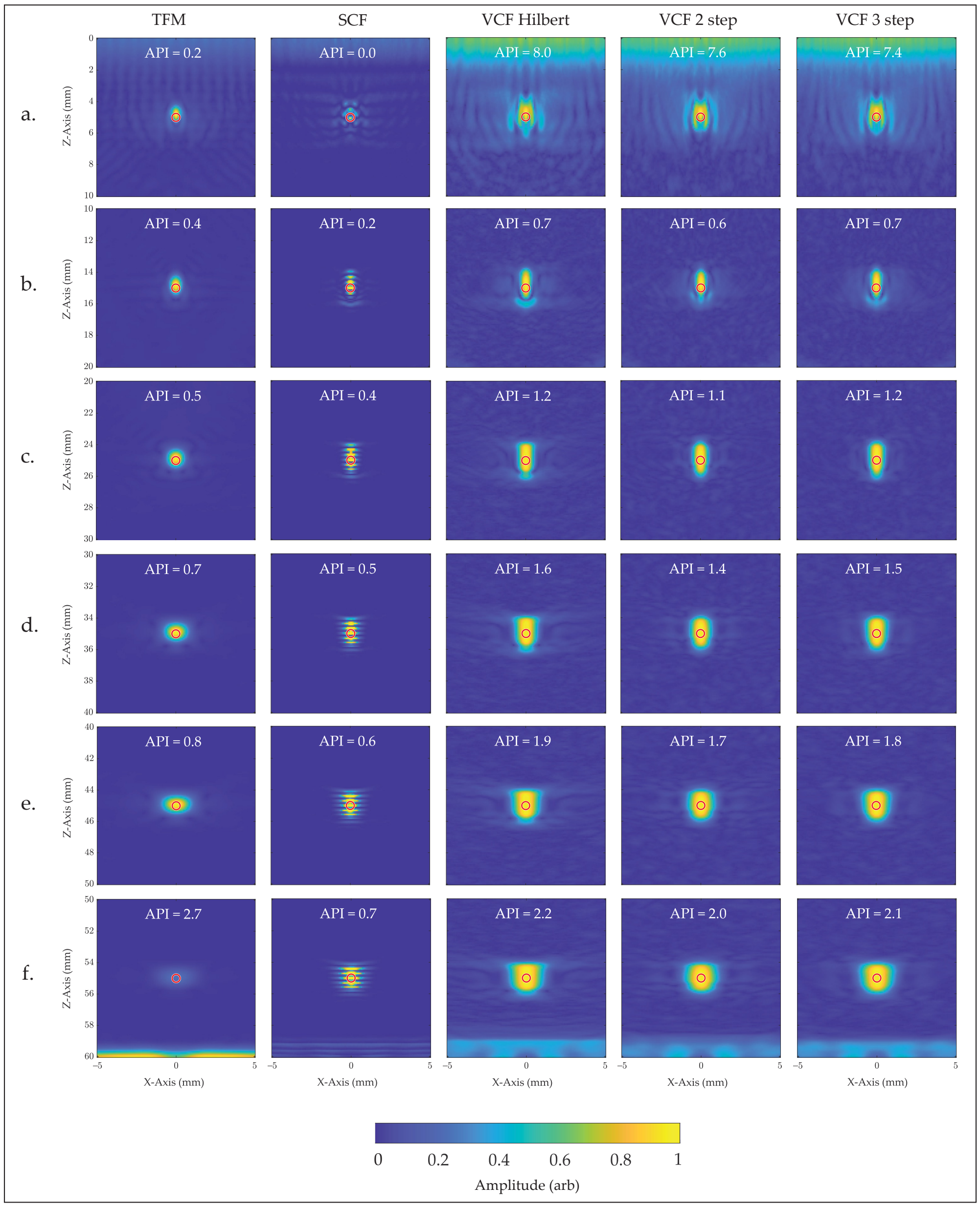

Figure 3.8 TFM and VCF images obtained from simulated data for a. a SDH located at a depth of 15 mm, b. a SDH located at a depth of 30 mm and c. a SDH located at a depth of 45 mm

Qualitatively, and as expected, the TFM shows a sharper restitution of the SDH top surface as compared to SCF and VCF in both simulation and experimental images. This is mainly due

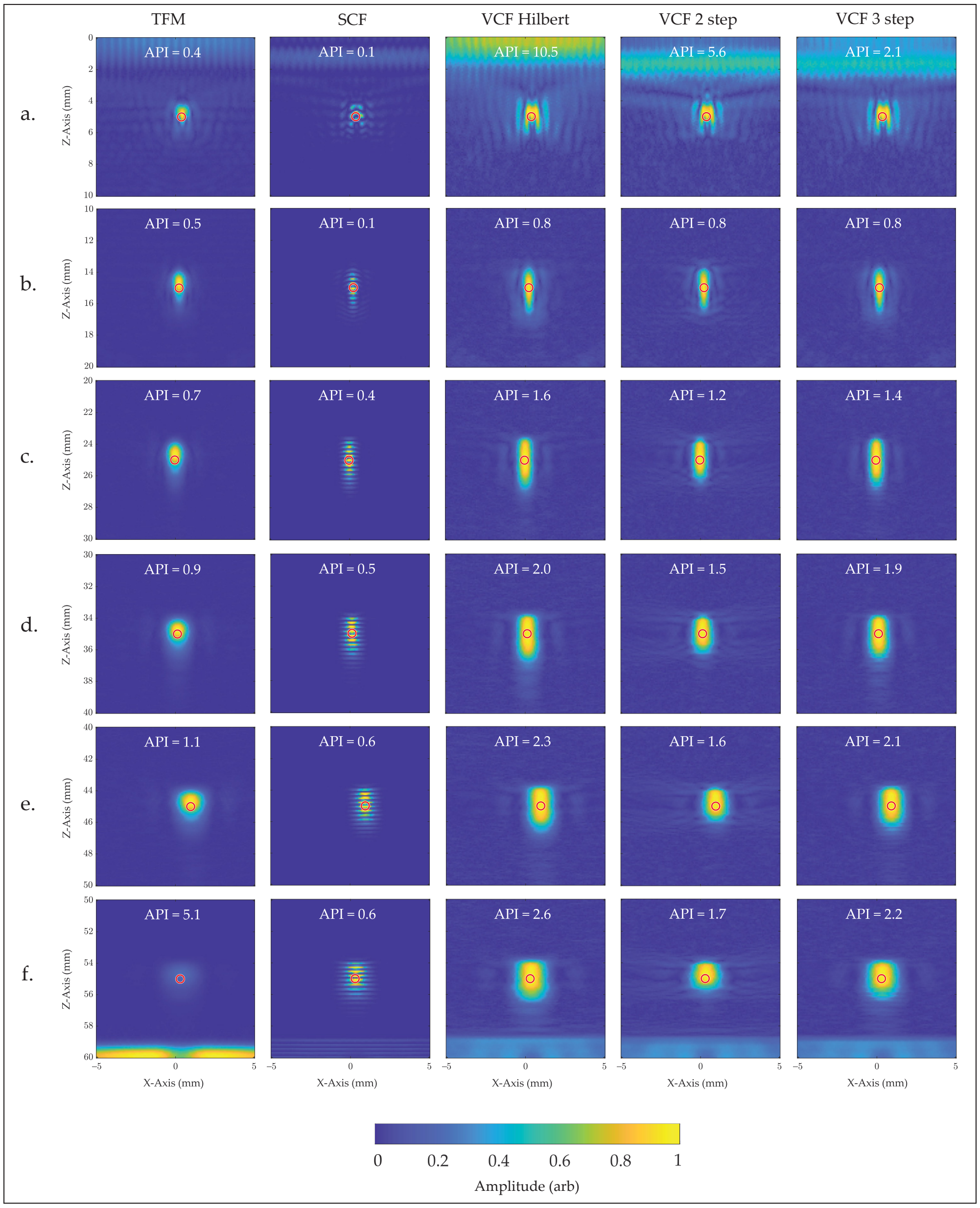

Figure 3.9 TFM and VCF images obtained from experimental results for a. a SDH located at a depth of 15 mm, b. a SDH located at a depth of 30 mm and c. a SDH located at a depth of 45 mm

to the nature of the constructive interference being generated by the DAS algorithm, which is longer in the case of a sign or phase summation (same sign or phase across the whole echo length), as compared to the amplitude summation (higher amplitude at the center of the echo). It can also be observed that SCF generates a more fragmented indication than VCF which could lead to misinterpretations. There is generally a good agreement between the simulation and the experimental results, except for the fact that the signal from the echo of the SDH is generally longer in the experimental case, resulting in larger indications (against z-axis) on images. When comparing the six SDH depths : 5 mm in Figure 3.8a. and 3.9a., 15 mm in Figure 3.8b. and 3.9b., 25 mm in Figure 3.8c. and 3.9c., 35 mm in Figure 3.8d. and 3.9d., 45 mm in Figure 3.8e. and 3.9e. and 55 mm in Figure 3.8f. and 3.9f., it can be noted that a higher level of artefacts is present when the discontinuity is close to the probe, which is mainly due to the near-field effect, and a larger indication (against x-axis) when the discontinuity is far from the probe, which is mainly due to beam spreading. Additionally, and as images are normalized against the maximum pixel intensity, strong restitution of the backwall vs. weak restitution of the SDH can be observed for TFM images in 3.8f. and 3.9f.. The opposite is observed for SCF and VCF reconstructions in the same figures, which is the expected behavior due to sensitivity to attenuation effects for TFM and weak coherence for specular reflectors for SCF and VCF. Finally, and what is certainly the most interesting result of this first setup, VCF images obtained using ϕ_1 or ϕ_2 are very similar the one using ϕ_H for both the simulated and experimental cases.

Quantitatively, the API (3.13) was calculated and presented at the top of each image in Figure 3.8 and 3.9, and its values summarized in Figure 3.10. Qualitative observations are confirmed, i.e. :

- A lower API for simulation results (ranging from near 0 to 8.0) as compared to experimental ones (ranging from 0.1 to 10.5)
- A lower API for TFM images (ranging from 0.2 to 5.1) as compared to VCF images (ranging from 0.6 to 10.5)
- A higher API for SDH affected by the near-field (5 mm depth) or further from the probe (55 mm depth)
- A similar API for VCF images based on ϕ_H, ϕ_1 and ϕ_2 (maximum discrepancy below 0.2 for simulated cases and below 0.9 for experimental cases, except for the SDH located a 5 mm depth which is in the near-field of the probe)

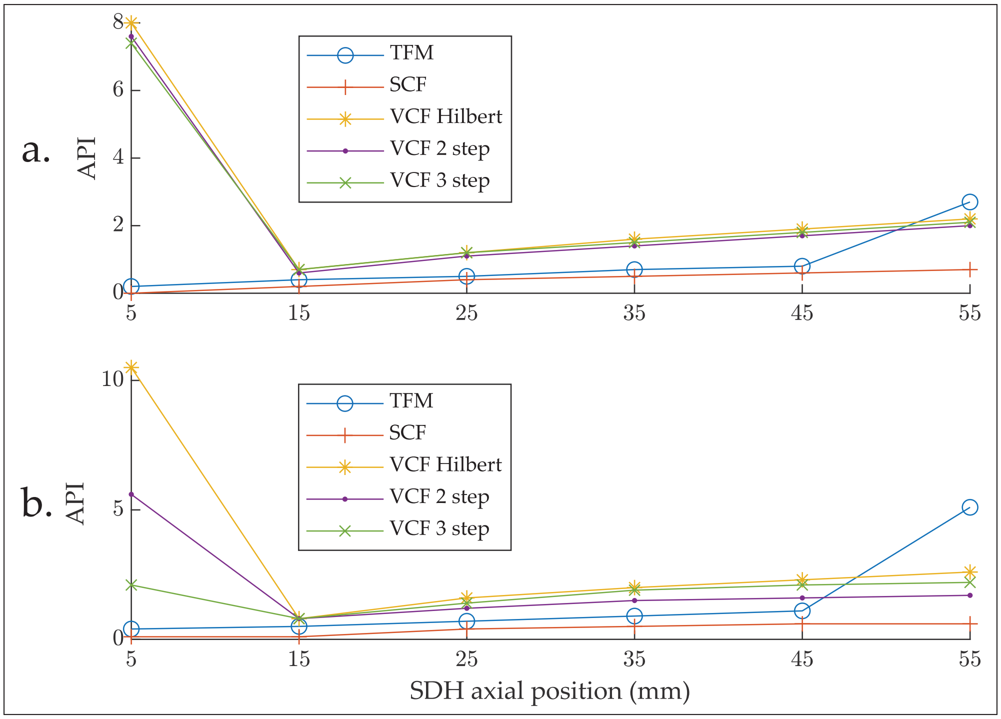

Figure 3.10 API calculated for each TFM, SCF and VCF image from both simulation (a.) and experimental (b.) results at each SDH location

3.4.2 Angled notches configuration results

Following the encouraging results presented in the previous section on the use of binarized signals for the instantaneous phase retrieval and then VCF reconstruction, a more complex case is now considered, mimicking crack-like defects located along the bevel of a weld as introduced in Section 3.3.5.2. After experimental FMC data acquisition, TFM images and VCF images were computed, and are presented in Figure 3.11 for surface breaking notches and in Figure 3.12 for mid-wall notches. For each individual image, a ROI of 19.20 mm × 20 mm was considered centered on the notch location. The reconstructed view or mode selection is based on sensitivity maps generated for each notch angle, considering a 2D crack model as presented in (Budyn *et al.*, 2019), and using the Arim package developed by Budyn et al. Computed sensitivity maps are presented in the supplementary downloadable material. For each notch angle, the view presenting the best TFM amplitude was selected. Thus, and using the same nomenclature as (Budyn *et al.*, 2019, 2018), the TT-T view was used for 90° and 80° notches and the TT-TT view

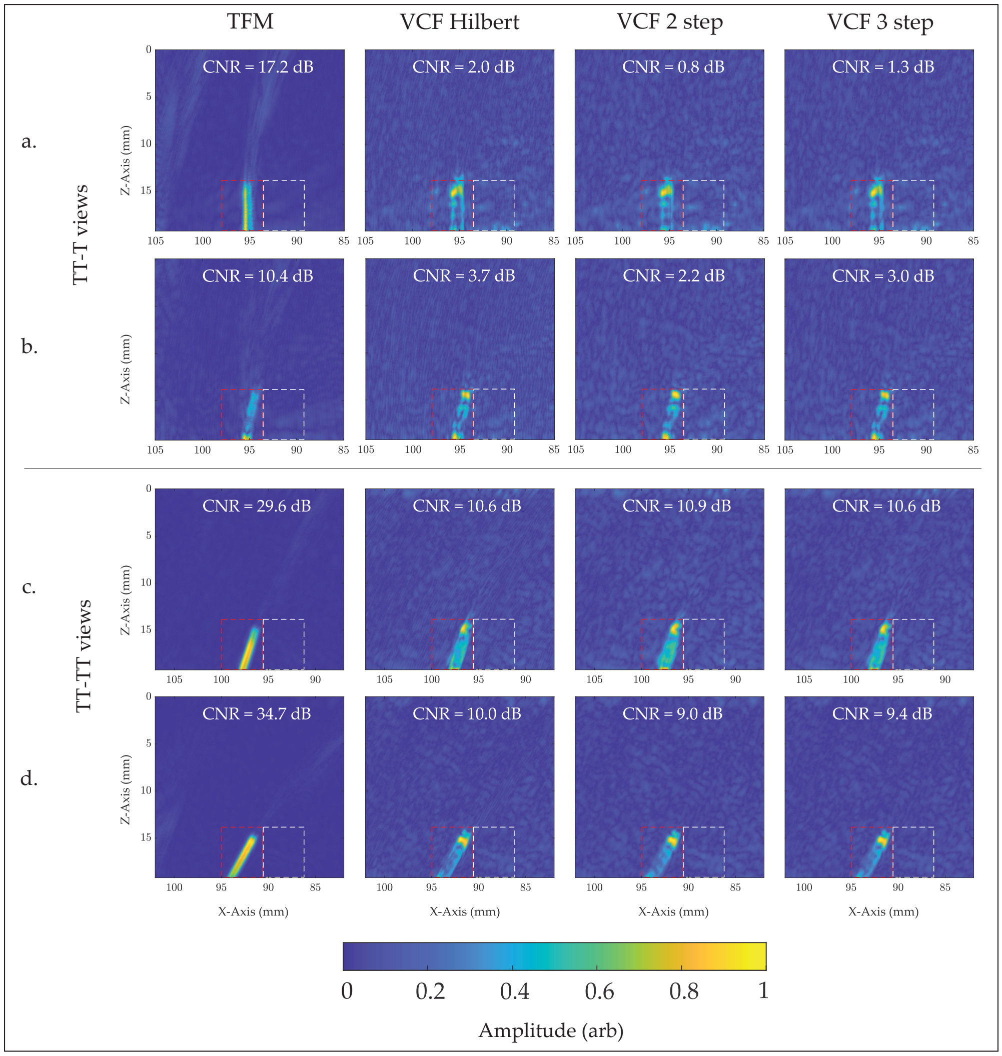

Figure 3.11 TFM and VCF images obtained from experimental results on the surface breaking angled notch sample for a. notch B1, b. notch B2, c. notch B3 and d. notch B4. Each subset of the ROI, used for calculation of the CNR, is represented by a red rectangle (dashed line) around the defect location and by a white rectangle (dashed line) outside the defect location

was used for 70° and 60° notches. The relevance of using sensitivity maps for the view selection when using VCF will be discussed later. Finally, CNR (4.13) was also computed, and is reported in the top of each image. The subset of the ROI around the defect location (red rectangle, dashed line) and outside the defect location (white rectangle, dashed line) used for its calculation is also represented on each image.

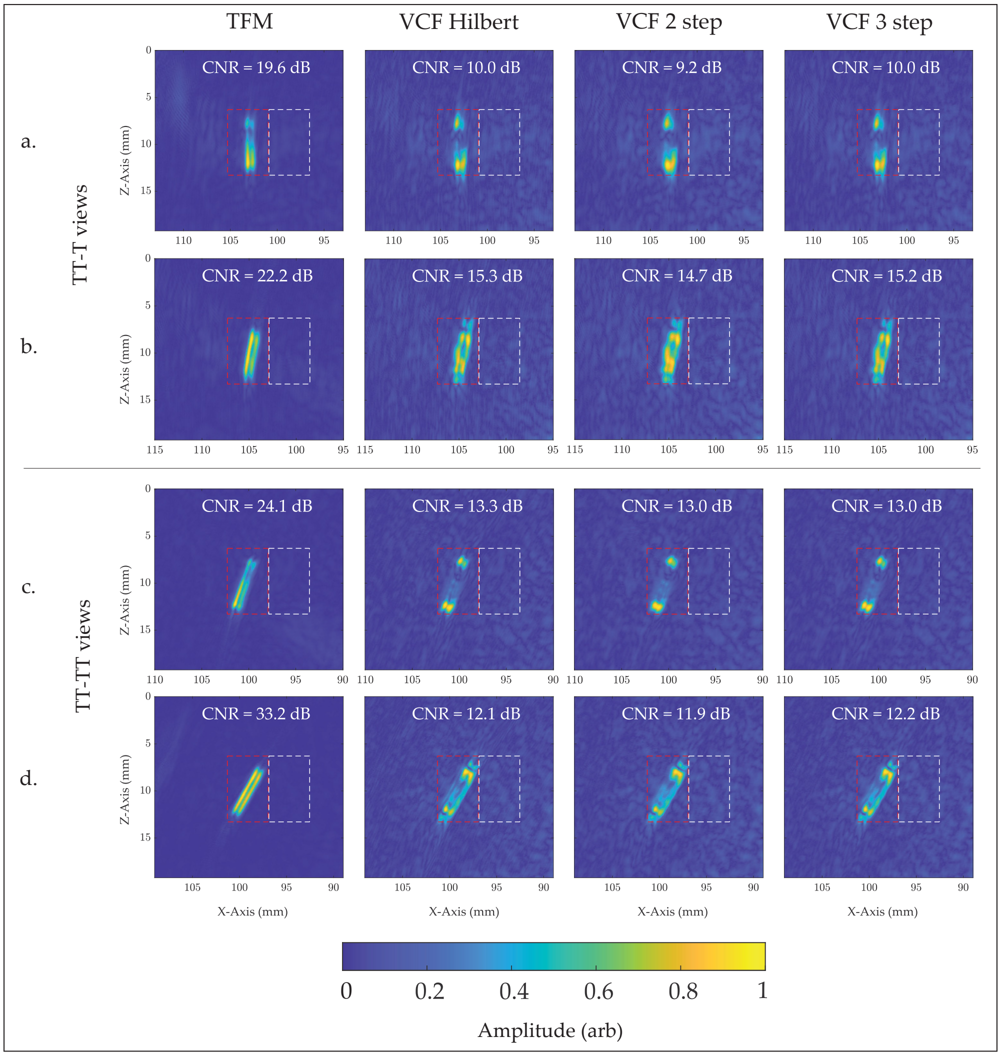

Figure 3.12 TFM and VCF images obtained from experimental results on the mid-wall angled notch sample for a. notch C1, b. notch C2, c. notch C3 and d. notch C4. Each subset of the ROI, used for calculation of the CNR, is represented by a red rectangle (dashed line) around the defect location and by a white rectangle (dashed line) outside the defect location

For both Figures 3.11 and 3.12, and as expected, CNR is higher for TFM images (ranging from 10.4 dB to 34.7 dB) as VCF images (ranging from 0.8 dB to 15.3 dB) are generally more prone to reconstruction artefacts due to a high coherence of the signal instantaneous phase. However, it should be noted that in this case, CNR is a useful quantitative comparison tool between imaging algorithms for a specific notch, as comparing two different notches involve considering the ray path difference and the associated attenuation. Additionally, it can be noted that similarly to what was published earlier (Camacho *et al.*, 2018; Gauthier *et al.*, 2021), and in Figures 3.11 and 3.12, VCF is more sensitive to defect tips as compared to TFM images. This higher sensitivity allows an easier and more accurate sizing of flaws than when using the −6 dB drop technique on TFM images. Then, when qualitative or quantitative comparisons are carried out using CNR, VCF images obtained using ϕ_H, ϕ_1 or ϕ_2 are very similar with an average CNR discrepancy of 0.7 dB between ϕ_H and ϕ_1, and 0.3 dB between ϕ_H and ϕ_2. Finally, results are consistent between both the mid-wall and surface breaking notches, with the 90° notch representing the worst case (low CNR) for VCF images.

3.5 Discussion

Through the different configurations that were investigated, and beyond the usual observations that can be made when comparing TFM to VCF, the results are very encouraging in terms of the use of binarized signals for imaging using the vector coherence factor. Differences in the resulting images between the 2-step and 3-step phase retrieval methods were minimal and the 2-step method could be preferred for its reduced data throughput (see Table 3.1). Although VCF images may seem less natural (representative of the real defect geometry) for the end user, one must remember that such images were generated using almost 50 times less data than a regular TFM, and that the process can be performed using greatly simplified, and hence less expensive electronics. Compared to TFM, pixel amplitude on VCF images is proportional to the degree of phase coherence and not associated with ultrasonic wave amplitude. Hence, the results are not affected by attenuation, provided the signal is still above the noise floor and the phase is retrievable. Consistency of defect restitution among different views is also straightforward when using VCF while requiring the use of sensitivity maps for TFM. Some drawbacks of this method should also be mentioned, as specular reflectors tend to be weakly represented (examples are backwalls or planar faces, as can be observed in Figure 3.8f., Figure 3.9f., Figure 3.11d. and in Figure 3.12d.). Therefore, one of the main interests of the presented procedure would be to provide a simple and lightweight imaging technique for crack-like defects. Additionally, while multiple configurations were tested in this study, and showed a good applicability for different scenarios, further investigations should be conducted on real defects. Also, natural cracks are not as flat as machined notches. Since VCF seems to respond strongly to diffractive flaws (corners and tips), natural cracks would probably be better imaged than notches. As mentioned earlier, sensitivity maps were used for the selection of the most relevant views for multi-view imaging (angled notch configurations). While multi-view imaging has a number of benefits in terms of the detailed restitution of a defect, it also has the disadvantage of allowing the selection of only a limited number of views for a given application when the defect is unknown, since considering all possible views would increase the computation time and interpretation complexity. However, while sensitivity maps are relevant for TFM, as they are based on the calculation of the maximum amplitude of the TFM at a given pixel for a given reflector, they are less appropriate for VCF applications. To illustrate this observation, an example is provided in Figure 3.13, where the TT-TT view is presented for notch B1 and the different imaging algorithms introduced earlier. As expected, and in accordance with sensitivity maps, the resulting TFM image has a very low contrast when compared to VCF images, which are more contrasted than their respective TT-T views presented earlier. Thus, there would be an interest in developing a similar tool to sensitivity maps, but for vector coherence factor used as an image, in order to help with view selection, enhance the performance of the method, and to study whether VCF is less dependent on the view choice.

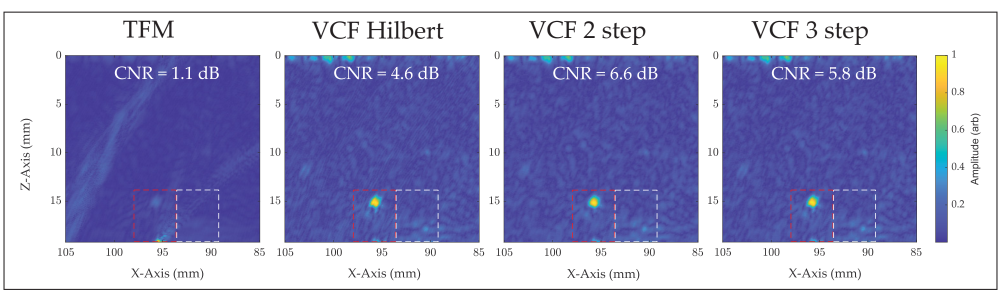

Figure 3.13 TFM and VCF images obtained from experimental results on notch B1 considering the TT-TT view

Finally, such a reduction in the data throughput and the development of high speed wireless networks, such as 5G, should allow to separate the acquisition unit from the processing unit.

Hardware cost reductions, easier processing software updates and enhanced storage are among the possibilities that could be offered.

3.6 Conclusion

This study investigated the use of VCF as an image itself in combination with a single-bit digitized signal to provide a lightweight and amplitude-free imaging technique. To apply the VCF algorithm using binarized data, the instantaneous phase was retrieved using a 2- or 3-step reconstruction process based on rising and falling edge positions. Both processes were evaluated qualitatively and quantitatively (using the API) in simulated and experimental conditions for six 0.5 mm SDH located at different depths. A more in-depth experimental evaluation was also conducted on angled surface breaking and mid-wall notches mimicking defects that could be found on weld bevels. CNR was computed for each individual image for comparison purposes. Results showed that the use of binarized data in combination with a phase retrieval procedure allows a very satisfying VCF reconstruction as compared to that using the instantaneous phase directly derived from the Hilbert transform with a maximum API value discrepancy being below 0.9 for the SDH in simulation or experimentally and an average CNR value discrepancy being below 0.7 dB for the angled notches. The estimated data throughput gain with using VCF from binarized data as compared to a full waveform digitization is around 50 times when a 12-bit ADC is considered. The use of sensitivity maps for imaging with VCF applications was also questioned in the light of the results that were obtained. Finally, this study paves the way for a different approach for NDT inspection units, where acquisition and processing could be split thanks to a reduced data throughput and a high speed network connection.

CHAPITRE 4

ULTRASONIC MULTI-VIEW DATA MERGING USING THE VECTOR COHERENCE FACTOR

Baptiste Gauthier[1] , Guillaume Painchaud-April[2] , Alain Le Duff[2] , Pierre Bélanger[1]

[1] PULETS, Département de Génie Mécanique, École de Technologie Supérieure, 1100 Notre-Dame Ouest, Montréal, Québec, Canada H3C 1K3
[2] Evident Industrial, 3415 Rue Pierre-Ardouin, Québec, Québec, Canada G1P 0B3

Article soumis dans «NDT&E International», Octobre 2022.

Données, codes et matériel supplémentaire : https://pulets.ca/open-data/NDTEINT-D-22-00500

4.1 Abstract

Over the years, ultrasonic imaging, both in the context of medical and industrial applications, has ushered in the development of many advanced techniques, some based on the use of the phase of the measured signal instead of its amplitude. These techniques use what is called coherence factors to enhance image quality. Leveraging these factors when calculating the image provides an effective solution to the low restitution of small scatterers, where specular reflectors in conventional ultrasonic imaging are strongly restituted, by weighting an amplitude-based beamformer output. In the field of nondestructive testing, this solution generally boils down to multiplying the well-known Total Focusing Method (TFM) image by a coherence factor map which is also obtained through delay-and-sum (DAS). It has also been demonstrated that coherence factor maps, especially in the case of the vector coherence factor (VCF), can be used as interpretable images themselves, which then results in an amplitude-free imaging process with many potential advantages. Additionally, the fusion of multi-view (or multi-mode) TFM images is still of particular interest since the burden of selecting a single or several views for an inspection scenario highly depends on the geometry and position of the defect that needs to be identified. Although sensitivity maps have been introduced to help in the selection of relevant views, no similar tool currently exists for views generated using directly coherence factor maps. In this study, two different merging approaches for multi-view VCF images are explored

and evaluated : pixel-by-pixel summation and maximum pixel value selection. A probabilistic threshold, derived from the VCF statistical background, is also defined to enhance the resulting merged view contrast. The images obtained through the proposed methods were evaluated both qualitatively and quantitatively using the Contrast-to-Noise Ratio (CNR). Experiments were conducted on two sets of samples. The first one was a 20 mm thick steel plate with Flat Bottom Holes (FBH) machined on its edge mimicking reflectors used for calibration of a circumferential weld inspection apparatus. The second one was composed of two 19.05 mm ($\frac{3}{4}''$) thick steel plates with EDM notches at several angles centered at the mid-wall or surface-breaking on the backwall. Since the experimental setup, consisting of a 60-element probe, with a center frequency of 7.5 MHz, standing on a 36° Rexolite wedge, involved exciting mostly shear waves, only views composed of the transversal wave path (i.e., T-T, TT-T, TT-TT, and TT-TTT) were considered for merging. Results show that by applying either one of the proposed merging methods, all artificial defects are reconstructed with a satisfactory CNR (above 30 dB), irrespective of the shape or location of the defects. Overall, the pixel-by-pixel summation and the maximum pixel value methods gave similar results. Applying the proposed threshold on the merged view improved the CNR by up to 15.8 dB. Finally, these simple but generic and robust multi-view merging methods and their associated thresholds could be employed while using a simplified hardware setup, as demonstrated previously in the literature.

4.2 Introduction

Ultrasonic nondestructive testing (NDT) has undergone many developments since the middle of the 20th century. From the single piezoelectric element or electromagnetic acoustic transducer, which is still widely used for thickness measurements or flaw detection, to the array composed of multiple elements, innovation has slowly drifted from the manufacture of probes to signal electronic control and post-processing. The field of ultrasonic imaging has thus seen no real improvement in multi-element probe fabrication over the last decade (except for specific applications such as high-temperature (Vithanage *et al.*, 2021) and non-contact methods, such as laser-ultrasonics (Shaloo, Schnall, Klein, Huber & Reitinger, 2022)), but significant progress has been made in terms of the performance of acquisition units. Simplicity of use (by limiting the number of parameters for the user), speed of acquisition (by limiting the amount of data or the number of firings) and improvements of the general performance of the acquisition units (to ensure a higher probability of detection) are among the major innovations of recent years. Imaging methods previously reserved for research and requiring several hours of computation can now be implemented in real time in commercial portable devices (Felice & Fan, 2018; Wang, Zhong, Lee, Fancey & Mi, 2020). There is also a growing interest in leveraging possibilities offered by machine learning and big data. However, industrial applications of ultrasonic NDT are still often slower to evolve than their medical or geophysical counterparts, mainly due to the conservative character of affiliated industries and the slow evolution of standards. They are also often challenged by other NDT methods such as radiography (Kah, Mvola, Martikainen & Suoranta, 2014). For these reasons, new imaging methods that do not completely change the way signals are acquired are being developed, to allow more information to be extracted from the same dataset.

Currently, the most widely used signal acquisition technique for advanced ultrasonic image processing is the Full Matrix Capture (FMC), where the elements of the probe are fired sequentially while simultaneously recording backscattered signals from the test piece on all elements. The resulting matrix of recorded time traces is processed using a delay-and-sum (DAS)-based beamformer to produce an image of the Region of Interest (RoI) (Holmes *et al.*, 2005). The Total Focusing Method (TFM) currently represents the gold standard of ultrasonic NDT beamformers and relies on the constructive interference of multiple time trace amplitudes at the location of the reflectors.

More recently, imaging methods based on so-called coherence factors, and that exploit the coherence of the signal instantaneous phase, have attracted great interest because of their high sensitivity to diffractive discontinuities. These methods are similar to the TFM in the sense that they also rely on a DAS beamforming process to generate coherence factor maps. These maps, only based on the signal phase analysis, present an amplitude-free characteristic as each pixel of the map is directly proportional to the degree of phase coherence (Camacho *et al.*, 2009; Prado *et al.*, 2015). If not used to weight an existing TFM, which enhances the contrast (Zhang *et al.*, 2013b), maps can be used directly for imaging, as demonstrated by (Gauthier *et al.*, 2021), and this method is generally referred to as Phase Coherence Imaging (PCI). Generating images in this way can also help reduce the data throughput during the acquisition of signals (Gauthier, Painchaud-April, Le Duff & Belanger, 2022).

Of all the different implementations of coherence factors found in the literature, such as the Phase Coherence Factor (PCF), the Sign Coherence Factor (SCF), and the Circular Coherence Factor (CCF) (Camacho *et al.*, 2019), and the Vector Coherence Factor (VCF) (Cruza *et al.*, 2017), the latter has proven to be the best suited for direct imaging. Indeed, it has been demonstrated that VCF can be used as an image itself for easier sizing and characterization of small omnidirectional reflectors such as crack tips (Camacho *et al.*, 2018; Zhang *et al.*, 2020). Using VCF in this way represents a good trade-off between the discontinuous indications produced by PCF and the computational complexity of CCF while maintaining a smoother aspect of the indications, similarly to using the signal envelope for the TFM. Additionally, the VCF formulation, which boils down to the summation of random unit vectors, comes with a strong statistical background, especially when imaging pristine regions of the test piece. As demonstrated by (Lesage *et al.*, 2021), this existing statistical knowledge, initially studied by Lord Rayleigh in 1880, can be leveraged to define threshold in order to enhance phase-based imaging methods.

One of the attributes of DAS-based beamformers is their ability to render different views (images) of the RoI considering multiple paths and modes for ultrasonic waves propagating in the test piece (Zhang *et al.*, 2012; Budyn). These different paths usually account for different speeds of sound and multiple reflections on the sample edges. This multi-view (also sometimes called multi-mode (Budyn *et al.*, 2019)) approach can be considered similar to the use of several view angles for the RoI, allowing a better characterization and sizing of the defect geometry. The main drawback of this method is the large number of views that can be generated, therefore increasing the complexity and time required for the analysis. One way to address this problem is to generate a merged view of all relevant information. Several approaches have already been suggested to create a merged view, ranging from simple summation to the selection of the relevant information in each view based on the expected defect response (Sy, 2018; Wilcox *et al.*, 2020), but these are usually affected by attenuation or require pre-existing knowledge of the type and orientation of defects to be detected.

In this study, the amplitude-free aspect of PCI and the strong statistical background of its VCF implementation are leveraged, for easier multi-view merging as compared to the original TFM. Two generic and simple merging methods are proposed based on a pixel-by-pixel summation and a maximum pixel value selection, each followed by the application of a statistical threshold. The methods were evaluated experimentally on two sets of samples. The first one was composed of two 19.05 mm ($\frac{3}{4}''$) thick steel plates with Electrical Discharge Machined (EDM) notches at several angles centered at the mid-wall or surface-breaking on the backwall. The second one was a 20 mm thick steel plate with Flat Bottom Holes (FBH) machined on its edge mimicking reflectors used for the calibration of circumferential weld inspection apparatus. The rest of the paper is divided as follows : Section 2 presents the materials and methods, including the VCF image reconstruction procedure, its statistical background, the related proposed threshold, and the methods used for merging the different views. The validation of the theoretical model and experimental results are presented in Section 3. A discussion is presented in Section 4, followed by conclusions in Section 5.

4.3 Materials and Methods

4.3.1 Vector Coherence Factor (VCF)

The Vector Coherence Factor (VCF) (Martínez-Graullera *et al.*, 2012; Cruz *et al.*, 2017), initially formulated to weigh and enhance the contrast of a TFM image, will be used as an image itself in this study, along with its multi-view implementation (Zhang *et al.*, 2010; Budyn *et al.*, 2019). The same method was already detailed in (Gauthier *et al.*, 2021, 2022), and presents several advantages in terms of data throughput reduction during acquisition and enhanced sensitivity to omnidirectional reflectors. The principle of VCF calculation is briefly recalled in the case where a FMC is recorded using a 1D linear array of N_e elements.

Consider a RoI in the test piece, discretized by a pixel grid in which each pixel is located by its position (x, z). The intensity of each pixel in the RoI after applying a DAS reconstruction algorithm based on signal amplitude, such as TFM, is given by :

$$\begin{aligned} I_{\mathrm{TFM}}(x,z) &= \left| \sum_{k=1}^{N_e} \sum_{l=1}^{N_e} \tilde{y}_{kl}(\tau_{kl}(x,z)) \right| \\ &= \left| \sum_{k=1}^{N_e} \sum_{l=1}^{N_e} |\tilde{y}_{kl}(\tau_{kl}(x,z))| \mathrm{e}^{i\phi_{kl}(\tau_{kl}(x,z))} \right|, \end{aligned} \tag{4.1}$$

where $\tilde{y}_{kl}(t)$ denotes the analytic signal of the amplitude received signal $y_{kl}(t)$ at a given time $\tau_{kl}(x, z)$, corresponding to the total time of flight between the emitting element k, a pixel located at (x, z), and the receiving element l.

Then, the calculation of VCF differs slightly from TFM by removing the amplitude term $\tilde{y}_{kl}(t)$, sensitive to attenuation effects (diffraction, scattering and absorption), and considering the in-phase and quadrature components of the signal derived from its instantaneous phase :

$$\begin{aligned} I_{\mathrm{VCF}}(x,z) = \Bigg(\left(\sum_{k=1}^{N_\mathrm{e}} \sum_{l=1}^{N_\mathrm{e}} \sin\left(\phi_{\mathrm{kl}}(\tau_{\mathrm{kl}}(x,z))\right) \right)^2 \\ + \left(\sum_{k=1}^{N_\mathrm{e}} \sum_{l=1}^{N_\mathrm{e}} \cos\left(\phi_{\mathrm{kl}}(\tau_{\mathrm{kl}}(x,z))\right) \right)^2 \Bigg)^m \end{aligned} \tag{4.2}$$

where ϕ_{kl} denotes the instantaneous phase of the analytic signal which is not directly influenced by attenuation effects. Exponent m is a modulation factor used to tweak the sensitivity to side lobes (Lyu *et al.*, 2021) and is generally set to $m = \frac{1}{2}$, which corresponds to the $\mathcal{L}_2$ norm. If $m = \frac{1}{2}$, (4.2) can be rewritten :

$$I_{\mathrm{VCF}}(x,z) = \left| \sum_{k=1}^{N_\mathrm{e}} \sum_{l=1}^{N_\mathrm{e}} \mathrm{e}^{i\phi_{\mathrm{kl}}(\tau_{\mathrm{kl}}(x,z))} \right|. \tag{4.3}$$

Additionally, note that for the multi-view implementation of VCF imaging, the nomenclature presented in (Budyn *et al.*, 2018) is used. Hence, a view is constituted of a transmitting path from the probe to the reconstructed pixel in the RoI, and a receiving path from the reconstructed pixel in the RoI to the probe. Each ray path can be composed of both the longitudinal (L) and transverse (T) wave modes, with or without reflection on the backwall. Generally, the first and final legs of the ray path are in the wedge and are assumed to be longitudinal waves and are omitted. As an example, the TT-L path is made of a TT half-skip path (transmission) from the probe to the defect, and an L direct path (reception) from the defect to the probe.

4.3.2 VCF Statistical Background and Possible Thresholding

As highlighted by (Lesage *et al.*, 2021), an interesting property of VCF is the statistical background related to its formulation which relies on the modulus of the summation of N_e^2 sines and cosines of unit vectors. Hence, the coherent response from a reflector will be characterized by an uniform phase across the different time traces at the corresponding ToF, while, on the other hand, a pristine area of the RoI should be characterized by an incoherent phase distribution. It turns out that for a sufficient number of signals to sum, i.e., $N_\mathrm{e}^2 \gg 1$, the conditional Probability Density Function (PDF) of VCF values corresponding to the summation of N_C coherent phases (meaning that they all have the same value) and N_I incoherent phases (meaning that they have a random uniform distribution between $[-\pi, +\pi]$), at a pixel location, is well described by a Rician distribution as will be discussed below. From there, a threshold can be defined to remove most of the background noise in the resulting image.

4.3.2.1 Distribution of VCF Values

First, when studying the statistical distribution of VCF values at a pixel location in the resulting image, a generic case can be formulated, where the sum performed at a given pixel location and corresponding ToF is composed of a mixture of N_C coherent values (that should correspond to the response from a reflector) and N_I incoherent values (that should correspond to the response from a pristine region in the sample). Note that $N_\mathrm{I} + N_\mathrm{C} = N_\mathrm{e}^2$ if, as considered in this study, the summation is based on an FMC. It turns out that this general case is very similar to previous results presented by Rice et al. (Rice, 1948, 1974; Hashemi, 1993; Abdi, Hashemi & Nader-Esfahani, 2000) when studying the summation of sine waves and random noise and extended to the transmission of Radio Frequency (RF) signals that propagate along several paths. Hence, it has been demonstrated that in the case of interest of this paper, the resulting VCF value distribution for a pixel follows a Rician distribution with noncentrality parameter $\nu = N_\mathrm{C}$ and scale parameter $\sigma = \sqrt{N_\mathrm{I}^2/2}$, and is defined by :

$$P(I_\mathrm{VCF}|\nu,\sigma) = \frac{2I_\mathrm{VCF}}{N_\mathrm{I}}\mathrm{e}^{\frac{-\left(I_\mathrm{VCF}^2+N_\mathrm{C}^2\right)}{N_\mathrm{I}}} I_0\left(\frac{2I_\mathrm{VCF}N_\mathrm{C}}{N_\mathrm{I}}\right) \tag{4.4}$$

where I_0 is the modified Bessel function of the first kind of order zero. The related Cumulative Distribution Function (CDF) is then defined as follows :

$$P(I_\mathrm{VCF} \leq Z|\nu,\sigma) = 1 - Q_1\left(\frac{\nu}{\sigma}, \frac{I_\mathrm{VCF}}{\sigma}\right) \tag{4.5}$$

where Z corresponds to a fixed value of I_VCF and Q_1 is the Marcum Q-function.

A first specific case is obtained if the phase ϕ is randomly and uniformly distributed between $[-\pi, +\pi]$ for all the phase sets, corresponding to a perfectly incoherent scenario ($N_C = 0$) where the resulting VCF values are only due to noise. In this case, the VCF value for a pixel follows a Rayleigh distribution (Rayleigh, 1880; Durand & Greenwood, 1957) – a special case of the Rician distribution – with scale parameter $\sigma = \sqrt{N_\mathrm{e}^2/2}$, and is defined by :

$$P(I_\mathrm{VCF}|\sigma) = \frac{2I_\mathrm{VCF}}{N_\mathrm{e}^2}\mathrm{e}^{\frac{-I_\mathrm{VCF}}{N_\mathrm{e}^2}}. \tag{4.6}$$

The associated CDF is then defined as follows :

$$P(I_\mathrm{VCF} \leq Z|\sigma) = 1 - \mathrm{e}^{\frac{-I_\mathrm{VCF}}{N_\mathrm{e}^2}}. \tag{4.7}$$

The generic case and first special case are illustrated in Figure 4.1, where the simulated VCF distribution, along with the related Rician theoretical PDF and CDF, from (4.4) and (4.5), for a single pixel and different mixes of N_C and N_I values are presented as if acquired with a 16-element probe ($N_e^2 = 256$) in a FMC acquisition. As can be observed in Figure 4.1a., the simulated VCF amplitude distribution and the theoretical Rician PDF are in agreement in all cases.

Finally, another special case is obtained if the phase ϕ is the same across all elements of the summation ($N_I = 0$). It corresponds to a perfectly coherent scenario, which would be the case for an ideal point-like reflector where there is no angle discrepancy for the phase recorded at the different elements of the array. In this case, the resulting VCF value for a given pixel is straightforward as, given that components of unit vectors are summed, it simply equals the number of summed signals, i.e. N_e^2.

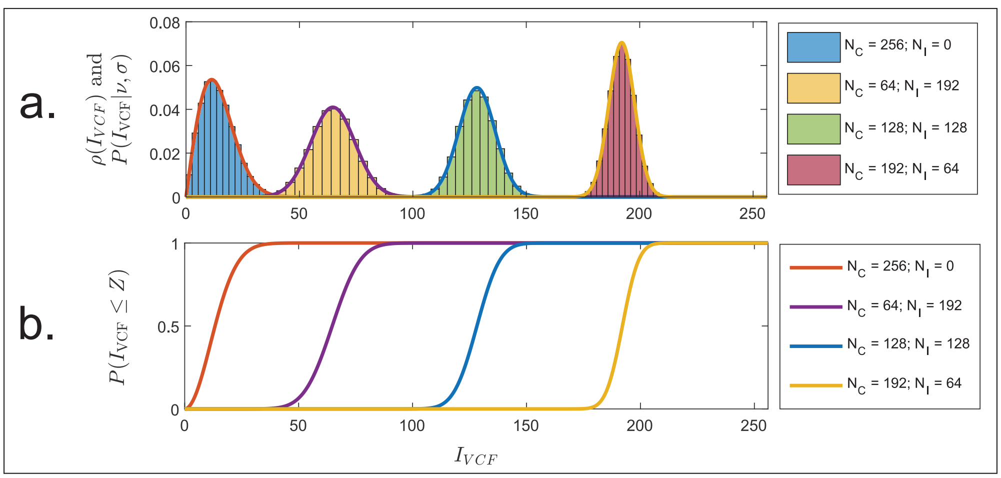

Figure 4.1 (a.) VCF simulated distribution and related theoretical Rician PDF and (b.) theoretical Rician CDF for different mixes of coherent and incoherent signal phases considering a a 16 elements linear probe and a FMC

4.3.2.2 VCF Threshold Definition

Over the years, several thresholds have been suggested to enhance VCF image contrast with still no significant consensus having been reached. Indeed, the use of Chebyshev's inequality (Prado, Higuti, Kitano & Martinez-Graullera, 2014) was considered along with a method to leverage Shannon information content relative to the number of pixels (Lesage *et al.*, 2021). In this paper, a simple probabilistic threshold to remove background noise is proposed. This threshold is derived from the perfectly incoherent scenario presented earlier, and relies only on the number of probe elements. Hence, one would consider a background noise removal threshold as relevant if it is related to a significant probability of having a VCF pixel value associated with noise, 99% is suggested. That means that it is assumed that rejecting VCF values below a threshold of 99% of the perfectly incoherent CDF would be sufficient to remove most of the background noise (assuming it is randomly and uniformly distributed). Thus, the proposed threshold, $\gamma_{99\%}$, directly derived from (4.7), is defined as follows :

$$\gamma_{99\%} = N_\mathrm{e}\sqrt{\ln\left(\frac{1}{1-0.99}\right)} \quad \forall N_\mathrm{e} \geq 4 \quad where \quad N_\mathrm{e} \in \mathbb{N}. \tag{4.8}$$

It introduces a linear dependency between $\gamma_{99\%}$ and N_e, but an inverse-square dependency between $\gamma_{99\%}/N_\mathrm{e}^2$ and N_e, which tends to apply a stricter threshold when a small quantity of time traces are summed up as one would expect.

4.3.3 Merging Methods for VCF Views

The merging of multiple views is already well documented for TFM (Sy, 2018; Wilcox *et al.*, 2020), and generally relies on preexisting knowledge of the type of defect and/or its orientation. If the geometry of the defect is known, sensitivity maps (Budyn *et al.*, 2019) or estimators (Sy *et al.*, 2018b) are used to partially or fully reject a view before applying merging method. On the one hand, these methods cannot be directly replicated when VCF is used as an image itself, as sensitivity maps or estimators are designed for amplitude-based images. On the other hand, applying a simple merging method, such as pixel-by-pixel summation or maximum pixel value selection, is still valid. Some of the drawbacks introduced by using these simple merging methods, such as an increased noise floor, can be compensated for by using the previously introduced threshold. In this study, the merging of multi-view VCF images is achieved through a thresholded pixel-by-pixel summation or a maximum pixel value selection. In the case of pixel-by-pixel summation, it is achieved, for each view, as follows :

$$S_{\mathrm{VCF}}(x, z) = \sum_{i=1}^{N_{views}} I_{\mathrm{VCF}}^{i}(x, z) \tag{4.9}$$

where N_{views} denotes the number of views considered for the summation and $I_{\mathrm{VCF}}^{i}(x, z)$ corresponds to a specific view at a pixel location (e.g. : T–T or T–TT). The resulting merged image after applying the threshold is obtained by :

$$I_{\mathrm{MergedVCF}}(x, z) = \begin{cases} S_{\mathrm{VCF}}(x, z), & \text{if } S_{\mathrm{VCF}}(x, z) > N_{\mathrm{views}} \times \gamma_{99\%} \\ N_{views} \times \gamma_{99\%}, & \text{if } S_{\mathrm{VCF}}(x, z) \leq N_{\mathrm{views}} \times \gamma_{99\%} \end{cases} \tag{4.10}$$

In the case of using a maximum pixel value selection for merging, it is achieved in the same manner, that is to say :

$$M_{\mathrm{VCF}}(x, z) = \max\{I_{\mathrm{VCF}}^{i}(x, z)\} \quad \text{with} \quad i \in [1, N_{\mathrm{views}}] \tag{4.11}$$

and the resulting merged image after applying the threshold is obtained by :

$$I_{\mathrm{MergedVCF}}(x, z) = \begin{cases} M_{\mathrm{VCF}}(x, z), & \text{if } M_{\mathrm{VCF}}(x, z) > \gamma_{99\%} \\ \gamma_{99\%}, & \text{if } M_{\mathrm{VCF}}(x, z) \leq \gamma_{99\%} \end{cases} \tag{4.12}$$

One could wonder whether the threshold could be applied before a pixel-by-pixel summation or maximum pixel value selection, but the authors have generally observed better performances (i.e., mainly better contrast) by applying the threshold after merging the different views. Hence, only this option will be considered in this study.

4.3.4 Quantitative Evaluation of Imaging Performance

To evaluate the benefits of applying the proposed threshold on the merged image, the Contrast-to-Noise Ratio (CNR) is used as a quantitative indicator of performance. CNR is particularly suitable when the discontinuity cannot be considered as a point-like scatterer. In our case, the CNR is defined as follows :

$$CNR = \frac{|\mu_{I_{-6\text{dB}}} - m_{\text{I}}|}{\sigma_I} \tag{4.13}$$

where $\mu_{I_{-6\text{dB}}}$ is the mean value of pixels above a -6 dB threshold, and m_{I} and σ_{I} are the median and standard deviation of all pixel values, respectively.

4.3.5 Experimental Setup

A set of two experimental configurations comprising 17 different artificial defects were considered to evaluate the performances of the proposed merging method for VCF views. These configurations aimed to be as generic as possible to allow conclusions to be applied to different defects within the scope of weld inspection. The first configuration presents machined FBHs at several angles and depths having a diameter of 3 mm, as well as surface and backwall grooves having a width of 3 mm in a 20 mm thick cold-rolled steel plate, as illustrated in Figure 4.2. The second configuration presents 0.3 mm notches machined EDM at several angles centered at the mid-wall or surface-breaking on the backwall in 19.05 mm ($\frac{3}{4}''$) thick low-carbon steel plates, as illustrated in Figure 4.3. As inspections of weld bevels are usually performed using a wedge to allow shear wave insonification of the sample, a 7.5L60 PWZ1, linear, 7.5 MHz, 60-element probe (EVIDENT Industrial, State College, PA, USA) mounted on top of an SPWZ1-N55S rexolite wedge (EVIDENT Industrial, Quebec, QC, Canada) was used in combination with a Vantage® 64 LE (Verasonics Inc., Kirkland, WA, USA) system to perform an FMC for each artificial defect presented in Figures 4.3 and 4.2. Signals were processed in Matlab® 2021b (MathWorks, Natick, MA, USA) and the pixel grid size for each VCF image calculation was set to 67 μm (15 pixels/mm).

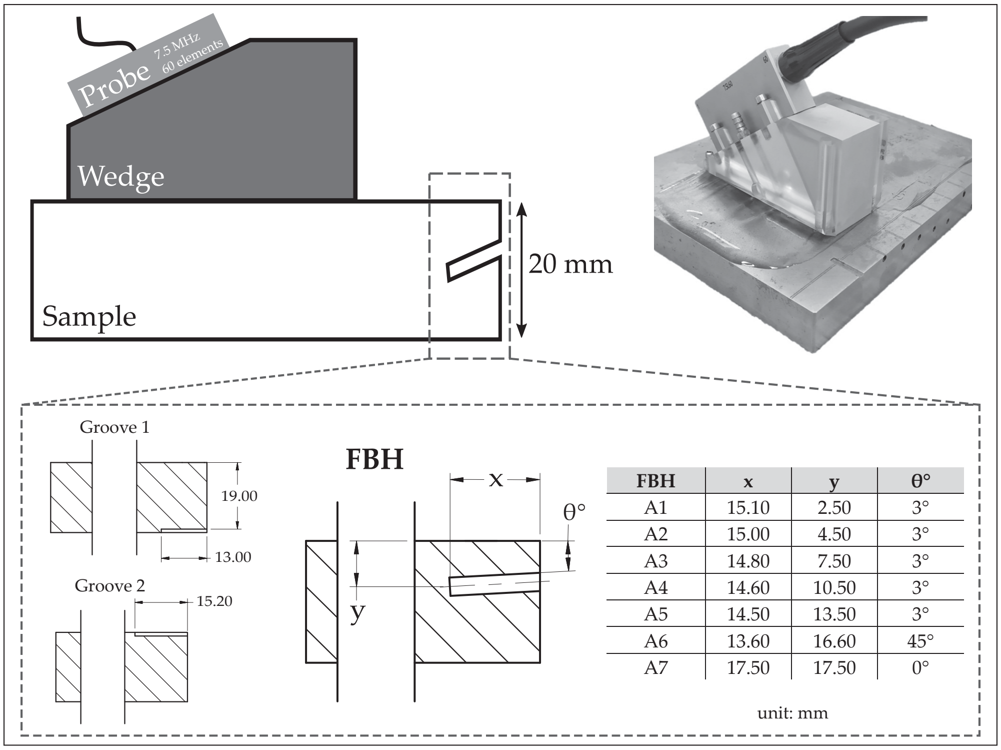

FBH	x	y	θ°
A1	15.10	2.50	3°
A2	15.00	4.50	3°
A3	14.80	7.50	3°
A4	14.60	10.50	3°
A5	14.50	13.50	3°
A6	13.60	16.60	45°
A7	17.50	17.50	0°

Figure 4.2 Experimental configuration for seven FBHs (3 mm diameter) as well as two grooves (3 mm width) machined in a cold-rolled steel 20 mm thick plate. Schematics for the seven FBHs (respectively FBH A1, A2, A3, A4, A5, A6 and A7) and the two grooves (Groove 1 and Groove 2) are provided. A linear ultrasonic array mounted on a wedge was used. A picture of the experimental configuration is provided

4.4 Results

4.4.1 Validation of the Theoretical VCF Values Distribution

The statistical model introduced in Section 4.3.2.1 was first evaluated on experimental data to validate the proposed thresholding method. Hence, two VCF views for FBH A2 are presented in Figure 4.4 (the TT-TTT and T-T views, respectively) along with their pixel amplitude distribution in a pristine region (red boxes) of the sample and the related Rayleigh and Rician fits.

On the one hand, the TT-TTT view has a relatively high CNR (44.4 dB) where pristine regions are low in amplitude (mean VCF value of 61.8) and the FBH can easily be identified on the

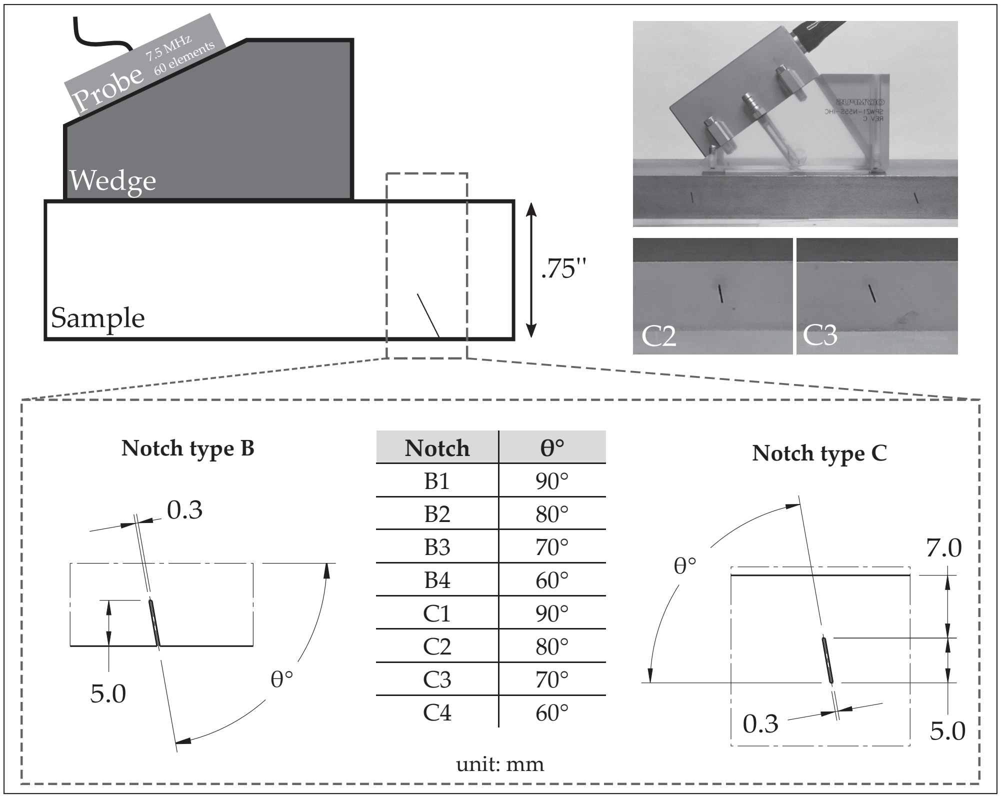

Notch	θ°
B1	90°
B2	80°
B3	70°
B4	60°
C1	90°
C2	80°
C3	70°
C4	60°

Figure 4.3 Experimental configuration for eight angled notches (0.3 mm wide) machined using EDM in low-carbon steel 19.05 mm ($\frac{3}{4}''$) thick plates. Schematics for the four surface-breaking notches (type B, respectively Notches B1, B2, B3 and B4) and the four notches located at the center of the plate (type C, respectively notch C1, C2, C3 and C4) are provided. A linear ultrasonic array mounted on a wedge was used. Pictures of Notches C2 and C3 as well as of the experimental configuration are provided

upper left corner of the image. On the other hand, the T-T view presents a much lower contrast (22.6 dB) with pristine regions having a higher pixel amplitude (mean VCF value of 111.7) and the FBH is harder to distinguish. Although VCF relies only on the signal phase, it is still expected that some views will be less sensitive to a given defect geometry or orientation simply because the reflected wave may not be captured by probe aperture. Additionally, VCF imaging can be affected by artifacts resulting from the occasional coherence of the signals phase in pristine locations. On the one hand, and as shown in Figure 4.4, one would expect that a pristine region of the TT-TTT view will be described by a pixel amplitude distribution close to the perfectly incoherent scenario presented in 4.3.2.1. On the other hand, a pristine region of the

T-T view should be better described by the generic case, where the phase set is composed of a mix of coherent phases (irrespective of whether they originated from a defect or artifacts) and incoherent phases. That is indeed the case when observing the pixel amplitude distribution of the selected pristine region for each view : in the case of the TT-TTT view, the theoretical Rayleigh distribution for the perfectly incoherent scenario corresponding to the use of a 60-element probe fits well with the highlighted pristine region pixels amplitude distribution. For the T-T view, the highlighted pristine region pixels amplitude distribution is well fitted by a Rician distribution (corresponding to the generic case), but not by the Rayleigh distribution (corresponding to the perfectly incoherent scenario). In conclusion to this first analysis, the theoretical VCF statistical background presented in 4.3.2.1 is observed experimentally. However, pristine regions of some views are better described by the generic case (as for the T-T view in the example of Figure 4.4) and hence would require a specific threshold definition. Still, and for simplicity, the proposed threshold presented in Section 4.3.2.2 will be used in all cases, as it will already provide a significant improvement of the resulting VCF image contrast and it is also assumed that most of the incoherent noise in the different views will be averaged out by the merging method. Hence, this threshold will be all the more effective where artifacts are low in amplitude. It should also be noted that, even if the statistical model developed in Section 4.3.2.1 was for a single pixel, all pixels in the resulting image, especially in pristine regions with low coherence, should be described by the same distribution. Hence, the same model can be employed when studying a set of pixels such as the one highlighted in Figure 4.4.

4.4.2 Example of VCF Multi-view Thresholded Merging

In this section, an example of the merging of different views and their thresholded version is presented for FBH A4. For both experimental configurations introduced in Section 4.3.5, only views involving a transversal mode of propagation were used, representing a subset of views that are generally selected for this type of inspection. The main goal of selecting a sub-set of views, which should remain the same for a given inspection scenario, is simply to reduce the computational burden associated with the calculation of more than 20 different views for each

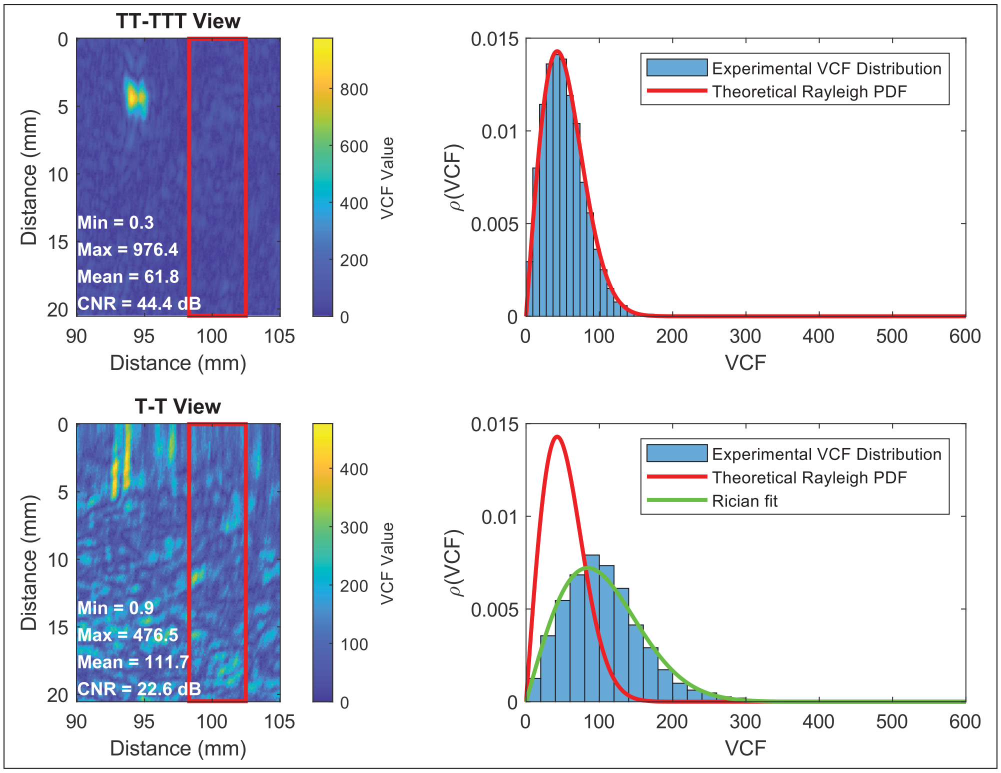

Figure 4.4 TT-TTT and T-T views (unnormalized) for FBH A2 and their related pixels amplitude distribution for a pristine region

FMC acquisition. After the selection of this subset, the merging method was applied as shown in Figure 4.5, in the case of using a pixel-by-pixel summation followed by the application of the proposed threshold (see Section 4.3.3). As can be observed, not all the views provide relevant information (i.e., a high level of coherence for a given scatterer), while on the merged view a strong indication of the FBH can be observed. Finally, applying the threshold allows a significant increase in the contrast of the final image.

4.4.3 FBH Configuration Results

The proposed merging methods and related thresholds were applied to all artificial defects presented in Section 4.3.5. Starting with the FBH configuration and for the sake of brevity half of the results are presented in Figure 4.6. The other results can be found in the supplementary material. The CNR was calculated and displayed on merged views that were individually

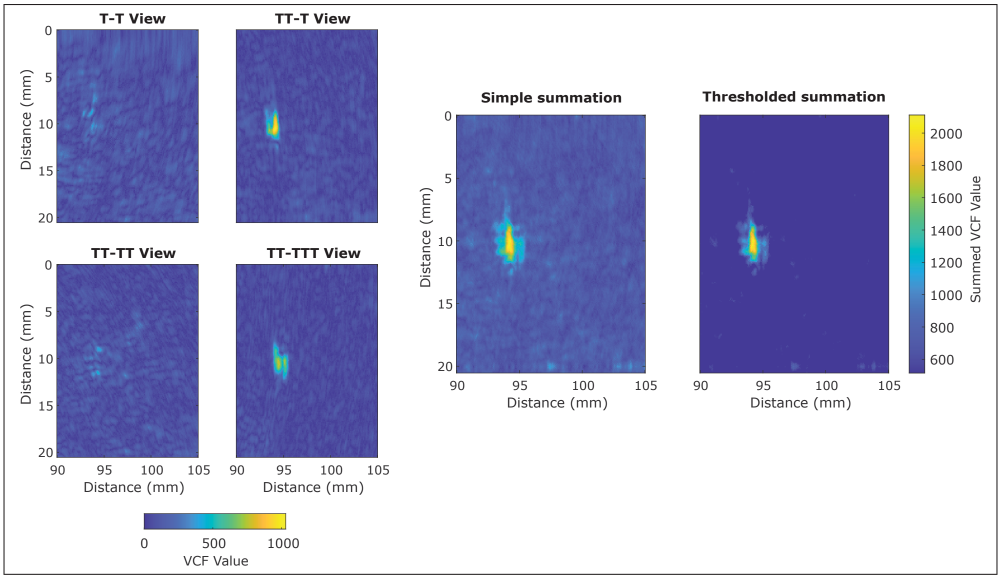

Figure 4.5 Individual - transversal only - VCF views unnormalized and sharing the same color palette (left). The summation of these views (center) and the thresholded version (right) are unnormalized and share the same color palette

normalized to their maximum. First, it can be observed that results obtained for the pixel-by-pixel summation and the maximum pixel value selection are more or less similar, both quantitatively with a low CNR discrepancy and qualitatively with similar indications in each case. Overall, all defects, no matter their location, are reconstructed with a CNR over 30 dB, which is already very satisfactory and one of the most interesting properties of using VCF to merge views. However, while all FBHs had the same diameter, not all of them were reconstructed with the same vertical extent (especially for those close to the upper surface of the sample), which can be a limitation of the method in terms of sizing capabilities, while still providing interesting detection capabilities. The thresholded version of the merged views generally allows great improvement of CNR (between 3.9 dB and 15.8 dB for the pixel-by-pixel summation and 8.9 dB and 19.2 dB for the maximum pixel value selection). No compromise on detectability is observed by applying the threshold on simply summed views, as some remaining artifacts can be observed at the bottom of the FBH A1 image. Yet, applying the threshold in the case of a maximum pixel value selection provides a highly contrasted image, but it comes at the risk of attenuating the relevant features, as can be observed for FBH A3.

4.4.4 Angled Notch Configuration Results

Following the results obtained for the FBH configuration, results obtained for the angled notch configuration are presented in Figure 4.7 in the same way, with only two cases presented for the surface-breaking notches and two cases for the centered notches. As for the FBH configuration, the pixel-by-pixel summation or maximum pixel value selection gives similar results, with a slightly higher CNR for the maximum pixel value method. Again, applying the proposed threshold on the resulting merged view allows for improvement of the CNR (between 3.6 dB and 7.9 dB for the pixel-by-pixel summation and 6.7 dB and 12.3 dB for the maximum pixel value selection). As with what was presented earlier in (Gauthier *et al.*, 2021), VCF imaging is highly sensitive to defect diffractive tips ans has a poor ability to reconstruct planar reflector faces. One can also observe what seems to be misalignment artifacts, particularly at the top of Notch B1 and Notch B2. In this case, the contribution of the T-T view to the merged view is greater for the region around the top of the tip compared to the contributions of the TT-T or TT-TT views. Thus, an increased number of reflections on the backwall, as is the case for TT-T and TT-TT views, could lead to additional phase delay or small velocity erros, and hence some incorrect superimpositions. For Notch C1 and Notch C2, view T-T does not contribute significantly to the merged view as compared to the TT-T and TT-TT views, and hence this misalignment is less observed.

4.5 Discussion

It is undeniable that VCF imaging comes with several benefits, such as removing the need for pre-calibration due to its amplitude-free characteristic, its sensitivity to highly diffractive scatterers such as crack tips, but also what it allows in terms of reduction of data required for the computation of the resulting image during acquisition (Gauthier *et al.*, 2022). VCF imaging has some documented drawbacks as well, such as its poor ability to image specular

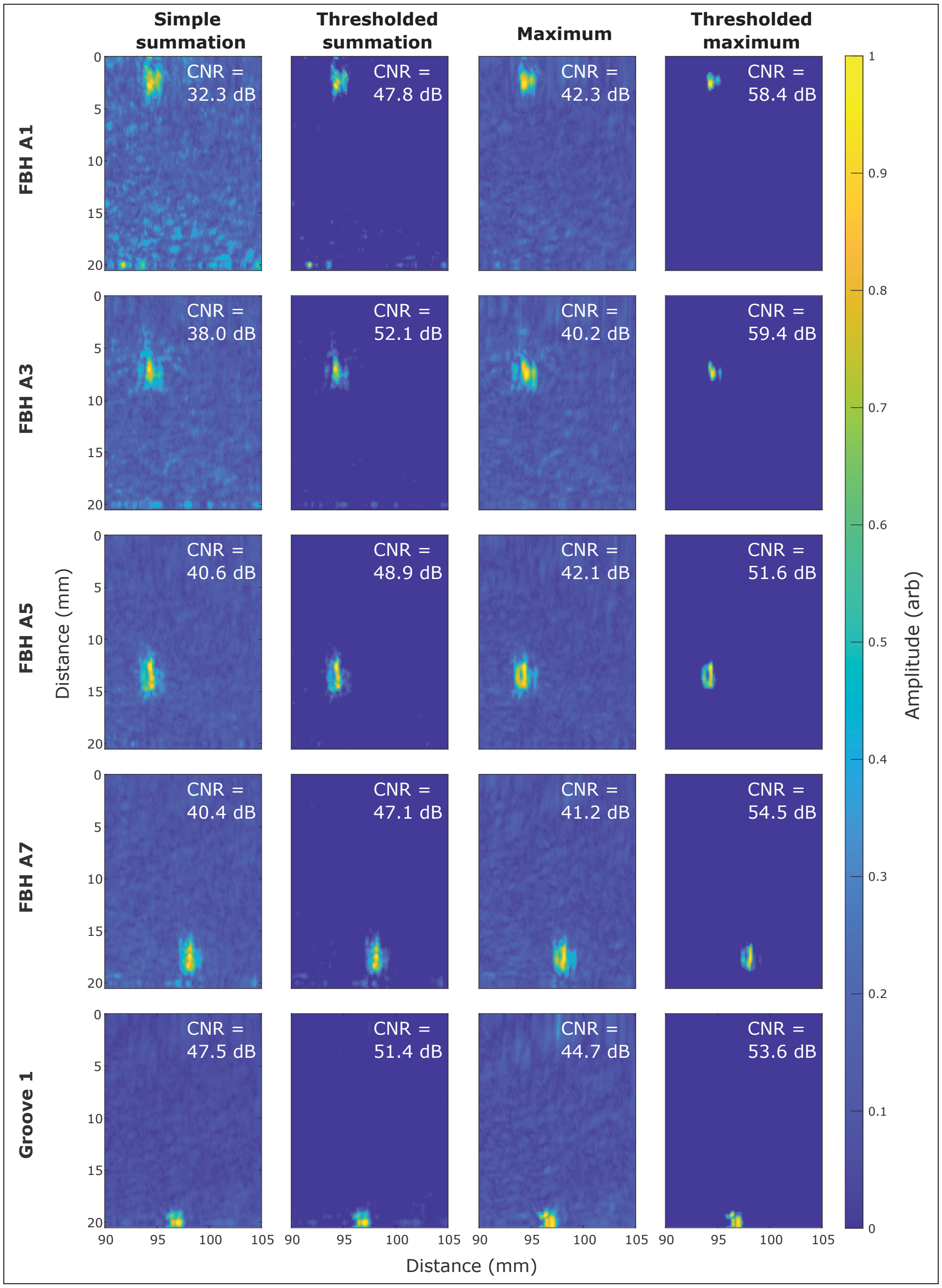

Figure 4.6 VCF merged views obtained experimentally for FBH A1, A3, A5, A7 and Groove 1 from top to bottom respectively, using simple summation (first column), thresholded simple summation (second column), maximum extraction (third column) and thresholded maximum (fourth column). Each resulting image is individually normalized against its maximum pixel amplitude. CNR is calculted for each image and displayed on the upper right corner of the image

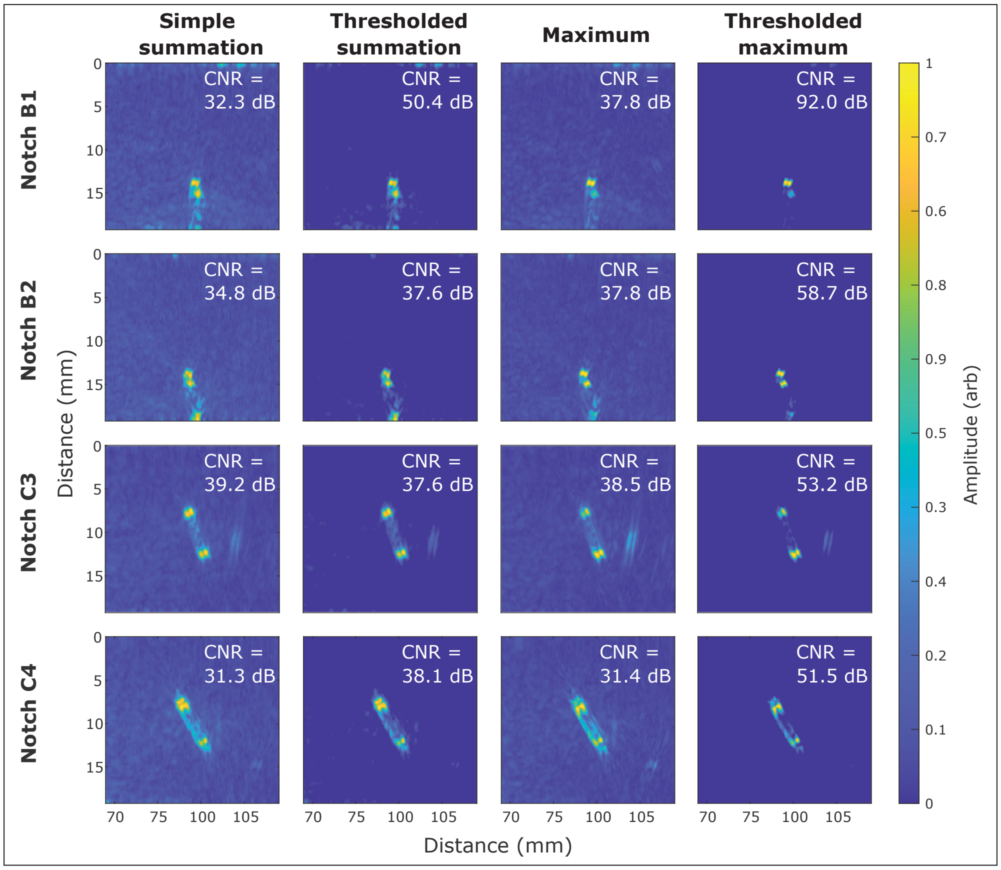

Figure 4.7 VCF merged views obtained experimentally for Notches B1, B2, C3 and C4 from top to bottom respectively, using simple summation (first column), thresholded simple summation (second column), maximum extraction (third column) and thresholded maximum (fourth column). Each resulting image is individually normalized against its maximum pixel amplitude. CNR is calculated for each image and displayed on the upper right corner of the image

reflectors like backwalls, the more elongated shape of indications corresponding to a defect as compared to conventional TFM, and its limited applicability when the Signal to Noise Ratio (SNR) becomes too low. However, the consistency of defect restitution among the different views offered by VCF imaging, meaning that each view contribution can be considered equally, allows the use of simple merging methods without compromise or hazardous assumptions. Hence, by pre-selecting a sub-set of views for a given configuration, all artificial defects, no matter its shape or orientation, were imaged whether by using the simple pixel-by-pixel summation or maximum pixel value selection methods for merging. It is noteworthy that for a specific defect shape or orientation, a single view may render a better image of the discontinuity. However, the proposed method aims to be as generic as possible, providing orientation and shape-agnostic multi-view merging methods. Indeed, while multi-view imaging is no longer restricted to research research laboratories, being available on high-end commercial equipment, it presents the additional burden of needing the selection of the right view for a given application without too much compromise on detection and sizing capabilities. The observed misalignment in the resulting merged view, especially in Figure 4.7, could be a source of confusion and would require further investigation. However, the authors believe that by performing a real-time inspection, compared to the static images presented in this study, most of the doubts related to these artifacts could be lifted. Furthermore, the statistical background associated with VCF for a generic case in which VCF values are described by a Rician distribution was presented. The parameters of this distribution are related to the number of coherent and incoherent phases used for the calculation of VCF at a given pixel location. The proposed threshold, derived from the perfectly incoherent case CDF (4.7), relies only on the number of summed signals, i.e., the number of probe elements for an FMC acquisition, and allows a great improvement of the contrast with limited impact on the resulting detectability. Despite its apparent simplicity, using the proposed threshold on VCF merged images turned out to be robust among the different presented scenarios. One could also consider taking advantage of the Rician distribution describing VCF values associated with the artifacts and background noise of some views, as presented in Figure 4.4, but this would require more complex post-processing and further investigation, which is beyond the scope of this study. Finally, the proposed threshold was designed to be conservative by setting its limit at 99% of the CDF of the perfectly incoherent scenario. As using this limit already gives satisfactory results in terms of CNR, the authors do not believe that decreasing it should be debated. However, raising this limit to 99.5% or 99.9% could be discussed in some cases where a stricter Probability of Detection (PoD) is required. Testing the proposed method with end users on real defects could also be an interesting avenue for future work.

4.6 Conclusion

This study investigated the merging of multi-view ultrasonic data through the use of VCF images. The consistency of defect restitution offered by VCF imaging across multiple views allows to consider simple merging methods without previous knowledge of defect shape and/or orientation or with the use of sensitivity maps, as is the case with conventional TFM. Two merging methods were considered : a pixel-by-pixel summation of the different views and a maximum pixel value selection from the different views. Additionally, a statistical threshold, derived from the theoretical distribution of VCF pixel amplitudes for a perfectly incoherent scenario was used to remove most of the background noise from the merged view. A more generic model for statistical analysis of VCF values was also introduced, and is based on a Rician distribution. The merging methods and threshold were evaluated experimentally on a set of two configurations composed of 3 mm diameter FBHs, 3 mm surface grooves and 0.3 mm width surface-breaking and mid-wall notches mimicking discontinuities generally found in weld bevel inspections. The theoretical statistical model for VCF pixel amplitude distribution was first verified on individual views from experimental data. A set of four views (transversal mode only) for the given application was selected before merging to limit the computational burden associated with the calculation of more than 20 individual views, which is not conceivable in practice. Then, merged views from both methods were presented before and after applying the statistical threshold and CNR was computed for each image to provide a quantitative assessment of the method. Results showed that all artificial defects were reconstructed with a satisfactory CNR (above 30 dB), irrespective of the shape or location of the defect. Overall, the pixel-by-pixel summation method and the maximum pixel value selection gave similar results. Applying the proposed threshold on the merged view allowed to improve the CNR by up to 15.8 dB. Some misalignment of indications was observed for some defects when merging the different views. This could be explained by phase shifts introduced by the multiple reflections along the wave path. However, this did not prevent the detection and location of presented defects. Being statistically-based, and although already conservative, the proposed threshold could be adjusted when a greater PoD is required. The generic model introduced for VCF pixel amplitude distribution could also be leveraged for a more specific threshold definition or view rejection. Finally, the simple and generic multi-view merging methods and the associated threshold presented in this study could be combined with the lightweight data acquisition process allowed by VCF to obtain a very competitive, advanced, and robust imaging strategy for the industry.

CONCLUSION ET RECOMMANDATIONS

Cette étude a permis d'approfondir les possibilités offertes par de nouvelles méthodes d'imagerie ultrasonore basées sur de la formation de faisceau par délai et somme dans le cas de la détection et la caractérisation de défauts dans les soudures. Les méthodes multivues ainsi que les algorithmes d'imagerie reposant uniquement sur l'utilisation de la phase du signal ont été explorés. Ces derniers présentent de nombreux avantages, comme leur sensibilité accrue aux géométries diffractives et le fait qu'ils ne sont pas sensibles à l'atténuation du signal.

Le principal objectif soutenant cette étude était l'amélioration et la simplification de l'information restituée au technicien d'inspection. En effet, celle-ci demeure très complexe d'interprétation, présentant des images très éloignées de celles à l'aspect plus naturel qui peuvent être produites par radiographie par exemple. Plus particulièrement, l'imagerie VCF a été au coeur de cette étude, représentant le meilleur compromis entre complexité de calcul et aspect des défauts reconstruits pour ce qui est des méthodes reposant uniquement sur la phase du signal. Des essais expérimentaux ont été conduits sur deux configurations différentes. La première est composée de deux plaques d'acier de ¾" d'épaisseur avec des encoches (centrées ou débouchantes) réalisées par électroérosion à plusieurs angles. La seconde est une plaque d'acier de 20 mm d'épaisseur avec des trous à fond plat (FBH) usinés sur son bord imitant les réflecteurs utilisés pour l'étalonnage d'un appareil d'inspection de soudures circonférentielles.

Dans un premier temps, l'imagerie VCF a été comparée à la méthode TOFD pour ce qui est du dimensionnement de défauts. Il a été montré que les performances de ces deux méthodes sont très similaires dans le cas de fines encoches ayant un angle par rapport au plan horizontal de plus de 70°, ce qui correspond à la majorité des défauts rencontrés dans les soudures. De plus, les performances de l'imagerie VCF pour le dimensionnement de défauts étaient meilleures que celles offertes par la TFM. Ces résultats permettent de considérer s'affranchir des sondes monoélément utilisées pour la TOFD, en particulier pour le cas de l'inspection de soudures circonférentielles. Seules les sondes multiéléments pourraient être conservées afin de réaliser autant le dimensionnement, qu'une image des défauts.

Dans un deuxième temps, la quantité de données nécessaire à la formation des images VCF et TFM a été étudiée. En effet, la méthode VCF reposant uniquement sur l'utilisation de la phase du signal, il a été montré qu'il est possible de reconstruire cette dernière à partir d'une acquisition beaucoup plus légère. Ainsi la phase du signal peut être reconstruite simplement à partir des fronts montants ou descendants du signal d'origine sans pour autant impacter de façon majeure l'image reconstruite (variabilité du CNR de moins de 0.7 dB). Cela permet de réduire la taille de la FMC de près de cinquante fois comparée à ce qui est nécessaire pour la TFM. De plus, l'acquisition ne reposant plus que sur la collecte d'une information binaire, une simplification importante de l'électronique pourrait être considérée.

Enfin, la fusion des différentes vues générées par l'imagerie VCF a été explorée. En effet, puisque l'amplitude des pixels reconstruits sur les images VCF est homogène à travers les différentes vues, n'étant pas affectée par l'atténuation, il est possible de considérer des méthodes de fusion relativement simples. La sommation pixel par pixel ainsi que la sélection des pixels ayant le maximum d'amplitude à travers les vues sont les deux méthodes proposées. De plus, un seuil statistique, issu de l'analyse de la distribution des valeurs VCF pour un cas parfaitement bruité, a été proposé et est appliqué sur l'image fusionnée afin de filtrer une grande partie du bruit de fond. De manière générale, les images VCF ainsi fusionnées permettent de reconstruire tous les types de défauts artificiels étudiés avec un CNR supérieur à 30 dB. Enfin, l'application du seuil statistique sur l'image fusionnée permet une amélioration du CNR allant jusqu'à 15.8 dB.

À la suite de ce travail, nous avons maintenant une meilleure connaissance des possibilités offertes par l'imagerie VCF, qu'elle soit considérée comme un complément de l'imagerie TFM ou bien en remplacement de celle-ci. En effet, l'imagerie VCF se révèle particulièrement adaptée pour un dimensionnement précis des défauts, peut être implémentée avec une électronique plus simple et générant moins de données, et permet enfin de considérer des méthodes de fusion des vues simples et génériques limitant le nombre de paramètres laissés au choix du technicien. Notons également qu'au cours de ce projet, notre partenaire industriel a intégré à ses équipements une méthode d'imagerie très proche du VCF, démontrant l'intérêt industriel pour cette méthode.

Cependant, d'autres pistes de recherches devraient également être explorées pour compléter ce travail et nous souhaitons ainsi formuler quelques recommandations pour faire suite à ce projet. Tout d'abord, les méthodes d'imagerie basées sur la phase du signal, comme le VCF, sont peu adaptées à la reconstruction des réflecteurs spéculaires (comme le fond d'une pièce). En effet, à la différence de l'imagerie TFM, ceux-ci sont reconstruits avec une amplitude très faible. Il serait donc intéressant d'explorer les différentes possibilités permettant d'extraire, toujours à partir de l'information de phase, l'information nécessaire à la reconstruction de ce type de réflecteurs. L'imagerie basée sur la fréquence instantanée du signal, directement dérivée de la phase, avait été envisagée dans des travaux préliminaires à ce projet, sans pour autant montrer des résultats satisfaisants. Ensuite, il serait désirable de pouvoir évaluer les performances de l'imagerie VCF dans le cas de l'inspection par ondes planes ou lorsque le nombre d'éléments de la sonde utilisés est réduit. En effet, ces méthodes sont utilisées lorsque des cadences d'inspection importantes sont nécessaires (le temps d'acquisition est largement réduit par rapport à une acquisition de type FMC). De plus, nous pensons que construire une électronique dédiée à la méthode d'acquisition binaire proposée dans la deuxième étude de ce projet serait une avenue intéressante permettant de réduire de façon importante les coûts liés à l'unité d'acquisition. Enfin, au-delà du seuil probabiliste proposé dans la dernière étude de ce projet, et reposant uniquement sur le cas parfaitement non cohérent, nous pensons que des travaux plus poussés pourraient être menés afin d'étudier plus en détail les possibilités de filtrage offertes par le cas générique décrit par une somme de phases cohérentes et non cohérentes.

BIBLIOGRAPHIE

Abdi, A., Hashemi, H. & Nader-Esfahani, S. (2000). On the PDF of the sum of random vectors. *IEEE Transactions on Communications*, 48(1), 7–12. doi : 10.1109/26.818866. Conference Name : IEEE Transactions on Communications.

Baiotto, R., Knight-Gregson, B., Nageswaran, C. & Clarke, T. (2018). Coherence Weighting Applied to FMC/TFM Data from Austenitic CRA Clad Lined Pipes. *Journal of Nondestructive Evaluation*, 37(3), 49. doi : 10.1007/s10921-018-0498-9.

Bevan, R. L. T., Budyn, N., Zhang, J., Croxford, A. J., Kitazawa, S. & Wilcox, P. D. (2020). Data fusion of multi-view ultrasonic imaging for characterisation of large defects. *IEEE Transactions on Ultrasonics, Ferroelectrics, and Frequency Control*, 1–1. doi : 10.1109/TUFFC.2020.3004982.

Budyn, N. *Imaging and defect characterisation using multi-view ultrasonic data in nondestructive evaluation*. (Thèse de doctorat).

Budyn, N., Bevan, R., Croxford, A. J., Zhang, J., Wilcox, P. D., Kashubin, A. & Cawley, P. (2018). Sensitivity images for multi-view ultrasonic array inspection. *AIP Conference Proceedings 1949*. doi : 10.1063/1.5031558.

Budyn, N., Bevan, R. L. T., Zhang, J., Croxford, A. J. & Wilcox, P. D. (2019). A Model for Multiview Ultrasonic Array Inspection of Small Two-Dimensional Defects. *IEEE Transactions on Ultrasonics, Ferroelectrics, and Frequency Control*, 66(6), 1129–1139. doi : 10.1109/tuffc.2019.2909988.

Camacho, J. & Fritsch, C. (2011a). *Adaptive Beamforming by Phase Coherence Processing*. IntechOpen. doi : 10.5772/15531.

Camacho, J. & Fritsch, C. (2011b). Phase coherence imaging of grained materials. *IEEE Transactions on Ultrasonics, Ferroelectrics, and Frequency Control*, 58(5), 1006–1015. doi : 10.1109/TUFFC.2011.1901. Conference Name : IEEE Transactions on Ultrasonics, Ferroelectrics, and Frequency Control.

Camacho, J., Parrilla, M. & Fritsch, C. (2009). Phase Coherence Imaging. *IEEE Transactions on Ultrasonics, Ferroelectrics, and Frequency Control*, 56(5), 958–974. doi : 10.1109/TUFFC.2009.1128.

Camacho, J., Atehortua, D., Cruza, J. F., Brizuela, J. & Ealo, J. (2018). Ultrasonic crack evaluation by phase coherence processing and TFM and its application to online monitoring in fatigue tests. *NDT & E International*, 93, 164–174. doi : 10.1016/j.ndteint.2017.10.007.

Camacho, J., Fritsch, C., Fernandez-Cruza, J. & Parrilla, M. (2019). Phase Coherence Imaging : Principles, applications and current developments. *Proceedings of Meetings on Acoustics*, 38(1), 055012. doi : 10.1121/2.0001201. Publisher : Acoustical Society of America.

Cantero-Chinchilla, S., Wilcox, P. D. & Croxford, A. J. (2022). A deep learning based methodology for artefact identification and suppression with application to ultrasonic images. *NDT & E International*, 126, 102575. doi : 10.1016/j.ndteint.2021.102575.

Cardoso, G. & Saniie, J. (2004). Performance evaluation of DWT, DCT, and WHT for compression of ultrasonic signals. *IEEE Ultrasonics Symposium, 2004*, 3, 2314–2317 Vol.3. doi : 10.1109/ULTSYM.2004.1418304.

Cardoso, G. & Saniie, J. (2005). Ultrasonic data compression via parameter estimation. *IEEE Transactions on Ultrasonics, Ferroelectrics, and Frequency Control*, 52(2), 313–325. doi : 10.1109/TUFFC.2005.1406557. Conference Name : IEEE Transactions on Ultrasonics, Ferroelectrics, and Frequency Control.

Chapuis, B. & Jenson, F. (2014). Inspection des soudures circonférentielles de pipes en utilisant des systèmes d'inspection ultrasonores automatisés (AUT) avec la méthode de discrimination zonale – Simulation de courbes de probabilités de détection (POD) en utilisant le logiciel CIVA. *NDT.net*, 2014-11, 3.

Charlesworth, J. P. & Temple, J. A. G. (2001). *Engineering applications of ultrasonic time-of-flight diffraction* (éd. 2nd). Baldock, Hertfordshire, England ; Philadelphia, Pa. : Research Studies Press.

Cheeke, J. D. N. (2017). *Fundamentals and Applications of Ultrasonic Waves* (éd. 2). Boca Raton : CRC Press. doi : 10.1201/b12260.

Coffey, J. M. & Chapman, R. K. (1983). Application of elastic scattering theory for smooth flat cracks to the quantitative prediction of ultrasonic defect detection and sizing. *Nucl Energy*, 22(5), 319–333.

Cruz, F., Simas Filho, E., Albuquerque, M., Silva, I., Farias, C. & Gouvêa, L. (2017). Efficient feature selection for neural network based detection of flaws in steel welded joints using ultrasound testing. *Ultrasonics*, 73, 1–8. doi : 10.1016/j.ultras.2016.08.017.

Cruza, J. F., Camacho, J. & Fritsch, C. (2017). Plane-wave phase-coherence imaging for NDE. *NDT & E International*, 87, 31–37. doi : 10.1016/j.ndteint.2017.01.005.

Demirli, R. & Saniic, J. (2004). Denoising and compression of ultrasonic signals using model-based estimation techniques. *IEEE Ultrasonics Symposium, 2004*, 3, 2306–2309 Vol.3. doi : 10.1109/ULTSYM.2004.1418302.

Drinkwater, B. W. & Wilcox, P. D. (2006). Ultrasonic arrays for non-destructive evaluation : A review. *NDT & E International*, 39(7), 525–541. doi : 10.1016/j.ndteint.2006.03.006.

Durand, D. & Greenwood, J. A. (1957). Random Unit Vectors II : Usefulness of Gram-Charlier and Related Series in Approximating Distributions. *The Annals of Mathematical Statistics*, 28(4), 978–986. doi : 10.1214/aoms/1177706798. Publisher : Institute of Mathematical Statistics.

Fan, B., Aeron, S., Pedrycz, A. & Valero, H. (2017). On Acoustic Signal Compression for Ultrasonic Borehole Imaging. *IEEE Transactions on Computational Imaging*, 3(2), 330–343. doi : 10.1109/TCI.2017.2670366. Conference Name : IEEE Transactions on Computational Imaging.

Fan, C., Caleap, M., Pan, M. & Drinkwater, B. W. (2014). A comparison between ultrasonic array beamforming and super resolution imaging algorithms for non-destructive evaluation. *Ultrasonics*, 54(7), 1842–1850. doi : 10.1016/j.ultras.2013.12.012.

Felice, M. V. & Fan, Z. (2018). Sizing of flaws using ultrasonic bulk wave testing : A review. *Ultrasonics*, 88, 26–42. doi : 10.1016/j.ultras.2018.03.003.

Gauthier, B., Painchaud-April, G., Le Duff, A. & Bélanger, P. (2021). Towards an Alternative to Time of Flight Diffraction Using Instantaneous Phase Coherence Imaging for Characterization of Crack-Like Defects. *Sensors*, 21(3), 730. doi : 10.3390/s21030730. Number : 3 Publisher : Multidisciplinary Digital Publishing Institute.

Gauthier, B., Painchaud-April, G., Le Duff, A. & Belanger, P. (2022). Lightweight and Amplitude-Free Ultrasonic Imaging Using Single-Bit Digitization and Instantaneous Phase Coherence. *IEEE Transactions on Ultrasonics, Ferroelectrics, and Frequency Control*, 1–1. doi : 10.1109/TUFFC.2022.3163621. Conference Name : IEEE Transactions on Ultrasonics, Ferroelectrics, and Frequency Control.

Ginzel, E. (2013). *Ultrasonic Time of Flight Diffraction*. Eclipse Scientific Products Incorporated.

Gomi, T. & Nakajima, M. (2012). Dual-Energy Subtraction X-Ray Digital Tomosynthesis : Basic Physical Evaluation. *Open Journal of Medical Imaging*, 2012. doi : 10.4236/ojmi.2012.23021. Publisher : Scientific Research Publishing.

Govindan, P. & Saniie, J. (2015). Processing algorithms for three-dimensional data compression of ultrasonic radio frequency signals. *IET Signal Processing*, 9(3), 267–276. doi : 10.1049/iet-spr.2014.0186.

Groover, M. P. (2007). *Fundamentals of modern manufacturing : materials, processes, and systems*. Third edition. Hoboken, NJ : J. Wiley & Sons.

Han, X., Wu, W., Li, P. & Lin, J. (2014). Application of ultrasonic phased array total focusing method in weld inspection using an inclined wedge. pp. 114–117. doi : 10.1109/SPAWDA.2014.6998539.

Han, X., Wu, W., Zhang, D. & Wan, H. (2019). Combination of direct, half-skip and full-skip TFM to characterize defect(II). doi : 10.1109/ultsym.2019.8925989.

Hashemi, H. (1993). The indoor radio propagation channel. *Proceedings of the IEEE*, 81(7), 943–968. doi : 10.1109/5.231342. Conference Name : Proceedings of the IEEE.

Holmes, C., Drinkwater, B. W. & Wilcox, P. D. (2005). Post-processing of the full matrix of ultrasonic transmit–receive array data for non-destructive evaluation. *NDT & E International*, 38(8), 701–711. doi : 10.1016/j.ndteint.2005.04.002.

Huthwaite, P. (2014). Accelerated finite element elastodynamic simulations using the GPU. *Journal of Computational Physics*, 257, 687–707. doi : 10.1016/j.jcp.2013.10.017.

Iakovleva, E., Chatillon, S., Bredif, P. & Mahaut, S. (2014). Multi-mode TFM imaging with artifacts filtering using CIVA UT forwards models. *AIP Conference Proceedings*, 1581(1), 72–79. doi : 10.1063/1.4864804.

International, A. (2019). *Standard Practice for Use of the Ultrasonic Time of Flight Diffraction (TOFD) Technique*. West Conshohocken, PA.

Isla, J. A. & Cegla, F. B. (2019). Simultaneous transmission and reception on all elements of an array : binary code excitation. *Proceedings of the Royal Society A : Mathematical, Physical and Engineering Sciences*, 475(2225), 20180831. doi : 10.1098/rspa.2018.0831.

Jeune, L. L., Robert, S., Dumas, P., Membre, A. & Prada, C. (2015). Adaptive ultrasonic imaging with the total focusing method for inspection of complex components immersed in water. *AIP Conference Proceedings*, 1650(1), 1037–1046. doi : 10.1063/1.4914712.

Joyce Y Liu, B. A. (2019). CMUT/CMOS-based Butterfly iQ - A Portable Personal Sonoscope. *ADVANCED ULTRASOUND IN DIAGNOSIS AND THERAPY*, 3(3), 115–118. doi : 10.37015/AUDT.2019.190819.

Kah, P., Mvola, B., Martikainen, J. & Suoranta, R. (2014). Real Time Non-Destructive Testing Methods of Welding. *Advanced Materials Research*, 933, 109–116. doi : 10.4028/www.scientific.net/AMR.933.109. Conference Name : Manufacture Engineering, Quality and Production System III ISBN : 9783038350910 Publisher : Trans Tech Publications Ltd.

Kim, J. H., Yeo, S., Kim, J. W., Kim, K., Song, T.-K., Yoon, C. & Sung, J. (2018). Real-Time Lossless Compression Algorithm for Ultrasound Data Using BL Universal Code. *Sensors*, 18(10), 3314. doi : 10.3390/s18103314. Number : 10 Publisher : Multidisciplinary Digital Publishing Institute.

Knight-Gregson, B., Peyton, A., Scully, P., Weston, M. & Davis, C. (2016). Improvement of ultrasonic cross-sectional imagery via the application of coherence weighting and the total focusing method.

Lesage, J., Marvasti, M. & Farla, O. (2021). Vector coherence imaging for enhancement of small omni-directional scatterers and suppression of geometric reflections. *NDT & E International*, 123, 102502. doi : 10.1016/j.ndteint.2021.102502.

Lokesh B & Thittai, A. K. (2016). Spatial resolution improvement in Plane Wave Imaging using adaptive Sign Coherence Factor weighting. *2016 IEEE International Ultrasonics Symposium (IUS)*, pp. 1–4. doi : 10.1109/ULTSYM.2016.7728900.

Lu, Y., Demirli, R., Cardoso, G. & Saniie, J. (2006). A successive parameter estimation algorithm for chirplet signal decomposition. *IEEE Transactions on Ultrasonics, Ferroelectrics, and Frequency Control*, 53(11), 2121–2131. doi : 10.1109/TUFFC.2006.152. Conference Name : IEEE Transactions on Ultrasonics, Ferroelectrics, and Frequency Control.

Lyu, Y., Hong, H., Song, G. & He, C. (2021). A Simplified Integration of Multi-Channel Ultrasonic Guided Wave System for Phased Array Detection and Total Focusing Imaging. *The International Journal of Acoustics and Vibration*, 26. doi : 10.20855/ijav.2021.26.21695.

Ma, H.-W., Wang, L.-Q., Li, K. & Chang, D.-Y. (2011). Design of an Orbit-holding Traveling Mechanism of Girth Weld Ultrasonic Scanner. *2011 Third International Conference on Measuring Technology and Mechatronics Automation*, pp. 938–941. doi : 10.1109/ICMTMA.2011.235.

Mansour, M. & Ali, M. (2010). Lossless compression of ultrasound RF data. *2010 IEEE International Ultrasonics Symposium*, pp. 2282–2285. doi : 10.1109/ULTSYM.2010.5935587.

Martínez-Graullera, O., Romero-Laorden, D., Martín-Arguedas, C. J., Ibañez, A. & Ullate, L. G. (2012). A new beamforming process based on the phase dispersion analysis. pp. 185–188. doi : 10.1063/1.3703167.

Mayworm, R. C., Alvarenga, A. V. & Costa-Felix, R. P. B. (2021). A metrological approach to the time of flight diffraction method (ToFD). *Measurement*, 167, 108298. doi : 10.1016/j.measurement.2020.108298.

Moles, M., Dubé, N., Labbé, S. & Ginzel, E. (2005). Review of Ultrasonic Phased Arrays for Pressure Vessel and Pipeline Weld Inspections. *Journal of Pressure Vessel Technology*, 127(3), 351–356. doi : 10.1115/1.1991881.

Nabil, Y., Toufik, B. & Morad, G. (2015). Ultrasonic signals parameters estimation based on differential evolution. *2015 3rd International Conference on Control, Engineering Information Technology (CEIT)*, pp. 1–5. doi : 10.1109/CEIT.2015.7233119.

Ogilvy, J. A. & Temple, J. A. G. (1983). Diffraction of elastic waves by cracks : application to time-of-flight inspection. *Ultrasonics*, 21(6), 259–269. doi : 10.1016/0041-624X(83)90058-6.

P. Yu, T. G. (2017). The Use of Multi-Mode TFM to Measure the Depth of Small Surface-Break Cracks in Welds. pp. 106–110. doi : 10.1109/FENDT.2017.8584593.

Pesavento, A., Burow, V. & Ermert, H. (1997). Compression of ultrasonic RF data. *1997 IEEE Ultrasonics Symposium Proceedings. An International Symposium (Cat. No.97CH36118)*, 2, 1471–1474 vol.2. doi : 10.1109/ULTSYM.1997.661854.

Pettit, J. R., Walker, A., Cawley, P. & Lowe, M. J. S. (2014). A Stiffness Reduction Method for efficient absorption of waves at boundaries for use in commercial Finite Element codes. *Ultrasonics*, 54(7), 1868–1879. doi : 10.1016/j.ultras.2013.11.013.

Prado, V. T., Higuti, R. T., Kitano, C. & Martinez-Graullera, O. (2014). Instantaneous phase threshold for reflector detection in ultrasonic images. *IEEE Transactions on Ultrasonics, Ferroelectrics, and Frequency Control*, 61(7), 1204–1215. doi : 10.1109/TUFFC.2014.3019.

Prado, V. T., Higuti, R. T., Kitano, C., Martínez-Graullera, & Adamowski, J. C. (2013). Lamb mode diversity imaging for non-destructive testing of plate-like structures. *NDT & E International*, 59, 86–95. doi : 10.1016/j.ndteint.2013.06.001.

Prado, V. T., Garcia Granja, S. C., Higuti, R. T., Kitano, C., Martinez-Graullera, O. & Segura, L. E. (2015). Defect detection in anisotropic plates based on the instantaneous phase of signals. *IEEE Transactions on Ultrasonics, Ferroelectrics, and Frequency Control*, 62(10), 1888–1894. doi : 10.1109/TUFFC.2014.006955. Conference Name : IEEE Transactions on Ultrasonics, Ferroelectrics, and Frequency Control.

Putsherry, D. & Misra, D. (2018). Project Specific AUT Automatic Ultrasonic Testing Validation to Determine Height Sizing Accuracy for Pipeline Girth Weld ECA Acceptance Criteria. *Day 4 Thu, November 15, 2018*, pp. D041S103R001. doi : 10.2118/193170-MS.

Rayleigh, L. (1880). XII. On the resultant of a large number of vibrations of the same pitch and of arbitrary phase. *The London, Edinburgh, and Dublin Philosophical Magazine and Journal of Science*, 10(60), 73–78. doi : 10.1080/14786448008626893.

Rice, S. (1974). Probability Distributions for Noise Plus Several Sine Waves - The Problem of Computation. *IEEE Transactions on Communications*, 22(6), 851–853. doi : 10.1109/TCOM.1974.1092281. Conference Name : IEEE Transactions on Communications.

Rice, S. O. (1948). Statistical properties of a sine wave plus random noise. *The Bell System Technical Journal*, 27(1), 109–157. doi : 10.1002/j.1538-7305.1948.tb01334.x. Conference Name : The Bell System Technical Journal.

Rocha, L., Velho, L. & Carvalho, P. C. P. (2002). Image moments-based structuring and tracking of objects. pp. 99–105. doi : 10.1109/SIBGRA.2002.1167130.

Royer, D., Dieulesaint, E. & Gennes, P.-G. d. (1996). *Ondes élastiques dans les solides. Tome 1 : Propagation libre et guidée*. Paris : Masson.

Ruiz-Reyes, N., Vera-Candeas, P., Curpián-Alonso, J., Mata-Campos, R. & Cuevas-Martínez, J. C. (2005). New matching pursuit-based algorithm for SNR improvement in ultrasonic NDT. *NDT & E International*, 38(6), 453–458. doi : 10.1016/j.ndteint.2004.12.001.

Schmerr, L. W. (1998). *Fundamentals of Ultrasonic Nondestructive Evaluation : A Modeling Approach*. Boston, MA : Springer.

Schmerr Jr, L. W. (2015). *Fundamentals of Ultrasonic Phased Arrays*. New York, NY : Springer.

Schmerr Jr, L. W. (2016). *Fundamentals of Ultrasonic Nondestructive Evaluation : A Modeling Approach* (éd. 2nd ed. 2016 édition). New York, NY : Springer.

Shaloo, M., Schnall, M., Klein, T., Huber, N. & Reitinger, B. (2022). A Review of Non-Destructive Testing (NDT) Techniques for Defect Detection : Application to Fusion Welding and Future Wire Arc Additive Manufacturing Processes. *Materials*, 15(10), 3697. doi : 10.3390/ma15103697. Number : 10 Publisher : Multidisciplinary Digital Publishing Institute.

Sharov, S. A., Orlov, Y. V. & Persiantsev, I. G. (2006). The high-speed compression of large data streams in ultrasonic diagnostics. *Pattern Recognition and Image Analysis*, 16(1), 68–70. doi : 10.1134/S1054661806010214.

Silk, M. G. (1987). Changes in ultrasonic defect location and sizing. *NDT International*, 20(1), 9–14. doi : 10.1016/0308-9126(87)90367-1.

Soto-Cajiga, J. A., Pedraza-Ortega, J. C., Rubio-Gonzalez, C., Bandala-Sanchez, M. & Romero-Troncoso, R. d. J. (2012). FPGA-based architecture for real-time data reduction of ultrasound signals. *Ultrasonics*, 52(2), 230–237. doi : 10.1016/j.ultras.2011.08.007.

Standards, B. (2009). *Time-of-flight diffraction technique as a method for detection and sizing of discontinuities*.

Sy, K., Bredif, P., Iakovleva, E., Roy, O. & Lesselier, D. (2018a). Development of methods for the analysis of multi-mode TFM images. *Journal of Physics : Conference Series*, 1017, 012005. doi : 10.1088/1742-6596/1017/1/012005.

Sy, K. (2018). *Étude et développement de méthodes de caractérisation de défauts basées sur les reconstructions ultrasonores TFM*. (Thèse de doctorat).

Sy, K., Brédif, P., Iakovleva, E., Roy, O. & Lesselier, D. (2018b). Development of the specular echoes estimator to predict relevant modes for Total Focusing Method imaging. *NDT & E International*, 99, 134–140. doi : 10.1016/j.ndteint.2018.07.005.

Vithanage, R. K. W., Mohseni, E., Qiu, Z., MacLeod, C., Javadi, Y., Sweeney, N., Pierce, G. & Gachagan, A. (2021). A Phased Array Ultrasound Roller Probe for Automated in-Process/Interpass Inspection of Multipass Welds. *IEEE Transactions on Industrial Electronics*, 68(12), 12781–12790. doi : 10.1109/TIE.2020.3042112. Conference Name : IEEE Transactions on Industrial Electronics.

Wang, B., Zhong, S., Lee, T.-L., Fancey, K. S. & Mi, J. (2020). Non-destructive testing and evaluation of composite materials/structures : A state-of-the-art review. *Advances in Mechanical Engineering*, 12(4), 1687814020913761. doi : 10.1177/1687814020913761. Publisher : SAGE Publications.

Welvaert, M. & Rosseel, Y. (2013). On the Definition of Signal-To-Noise Ratio and Contrast-To-Noise Ratio for fMRI Data. *PLOS ONE*, 8(11), e77089. doi : 10.1371/journal.pone.0077089. Publisher : Public Library of Science.

Wilcox, P. D., Croxford, A. J., Budyn, N., Bevan, R. L. T., Zhang, J., Kashubin, A. & Cawley, P. (2020). Fusion of multi-view ultrasonic data for increased detection performance in non-destructive evaluation. *Proceedings of the Royal Society A : Mathematical, Physical and Engineering Sciences*, 476(2243), 20200086. doi : 10.1098/rspa.2020.0086. Publisher : Royal Society.

Zhang, H., Zeng, L., Fan, G., Zhang, H., Zhu, Q. & Zhu, W. (2020). Instantaneous Phase Coherence Imaging for Near-Field Defects by Ultrasonic Phased Array Inspection. *Sensors (Basel, Switzerland)*, 20(3), 775. doi : 10.3390/s20030775.

Zhang, J., Drinkwater, B. W. & Wilcox, P. D. (2013a). Comparison of ultrasonic array imaging algorithms for nondestructive evaluation. *IEEE Transactions on Ultrasonics, Ferroelectrics, and Frequency Control*, 60(8), 1732–1745. doi : 10.1109/TUFFC.2013.2754. Conference Name : IEEE Transactions on Ultrasonics, Ferroelectrics, and Frequency Control.

Zhang, J., Drinkwater, B. W., Wilcox, P. D. & Hunter, A. J. (2010). Defect detection using ultrasonic arrays : The multi-mode total focusing method. *NDT & E International*, 43(2), 123–133. doi : 10.1016/j.ndteint.2009.10.001.

Zhang, J., Drinkwater, B. W. & Wilcox, P. D. (2013b). Ultrasonic array imaging in nondestructive evaluation : total focusing method with using circular coherence factor. *Eighth International Symposium on Precision Engineering Measurement and Instrumentation*, 8759, 87592N. doi : 10.1117/12.2014569.

Zhang, Q., Chen, T., Que, P. & Xing, Y. (2008). Compression of ultrasonic signals with the lifting scheme wavelet transform. *Russian Journal of Nondestructive Testing*, 44(7), 490–495. doi : 10.1134/S1061830908070073.

Zhang, Y. D., Shen, X., Demirli, R. & Amin, M. G. (2012). Ultrasonic Flaw Imaging via Multipath Exploitation. *Advances in Acoustics and Vibration*, 2012, 1–12. doi : 10.1155/2012/874081.